Measurement of Cold Molecular Collisions between co-trapped OH and Rb

by

John M. Gray

B.S., Georgia Institute of Technology, 2014

A thesis submitted to the

Faculty of the Graduate School of the

University of Colorado in partial fulfillment

of the requirements for the degree of

Doctor of Philosophy

Department of Physics

2022

Committee Members:

Heather Lewandowski, Chair

John Bohn

Eric Cornell

Margaret Murnane

Robert Parson

Gray, John M. (Ph.D., Physics)

Measurement of Cold Molecular Collisions between co-trapped OH and Rb

Thesis directed by Prof. Heather Lewandowski

Cold molecules are an important tool in the study of precision measurement, chemical physics, and quantum collisions. Polar radical molecules, like the hydroxyl radical OH, are particularly interesting due to their importance as short lived intermediates in extreme chemical environments, such as the interstellar medium, the atmosphere, and combustion. In this thesis, we describe the OHRbIT Experiment (**OH** and **Rb I**nteracting in **T**raps). With this experiment, we seek to measure the cross sections of collisions between cold OH molecules and ultracold Rb atoms in a co-trapped environment. Rubidium atoms are trapped in a quadrapole magnetic field at a temperature of $T \sim 500\mu K$. The atoms are transported through the vacuum chamber to overlap with an electrostatic quadrapole trap that is used to trap OH molecules. The OH molecules are slowed using a Stark Decelerator and trapped in the electric quadrapole trap with a temperature of $\sim 50mK$. The cross sections of the interaction are extracted from measurements of the evolution of the number and energy distribution of the trapped OH molecules. We describe the 1+1' resonantly-enhanced multiphoton ionization (REMPI) detection scheme that allows us to measure the energy distribution of the OH molecules. We also discuss the production of vacuum ultraviolet (VUV) light at 118nm that is used in the REMPI detection.

Dedication

To my parents.

Acknowledgements

First, I would like to thank my advisor, Heather Lewandowski, for the advise, expertise, and support that she has provided throughout my PhD. I would also like to thank the rest of the Lewandowski group. Travis Briles and Yomay Shyur were both great mentors who helped me learn a lot about experimental physics. Jason Bossert and Tommy Garcia both worked directly with me on the OH and Rb apparatuses, and were both great scientists and a pleasure to work with. The post-docs on the ion experiment, Philip Schmidt and Catherine Catani, were always there to help. And to the rest of the Lewandowski Group who has helped me during my time here; Maya, Cam, Greg, Kyle, Olivia, Chase, Ben, Andres, and Ian.

Contents

Chapter

Figures

Figure

Chapter 1

Introduction

1.1 Why Cold Molecules?

Cold and ultracold molecules have been an area of intense research interest in the past few decades. As an extension of the study of cold atoms, cold molecules offer many of the same challenges, tools, and goals. However, owing to the complex quantum energy level structure due to rotational and vibrational degrees of freedom, cold molecules offer a rich environment for the study of quantum systems and their applications. The fundamental goal of studying cold molecules is the understanding and manipulation of individual quantum states to probe complex physics in a controlled manner. Cold molecules have been used in precision measurements for tests of fundamental physics and to probe the variation of fundamental constants, such as the fine structure constant[1], the electron electric dipole moment[2, 3, 4], and CP-violation[5]. Cold molecules are also useful for studying the physics of chemical reactions, and allow for control of the quantum state of the reactants, collision energy, and even the orientation of reactants.[6, 7]

The study of cold molecules is also important for studying the natural chemical processes found in many extreme environments. The isolated environment in which cold molecules are often produced is an ideal environment for studying radicals and ions which can be highly chemically reactive. A plethora of chemical species have been found to exist in the interstellar medium, which has a temperature of $\sim 4K$.[8] Laboratory experiments with cold molecules can be used to study the spectroscopic and chemical properties of these species to better understand the chemistry in the interstellar medium, predict molecules that may be found, and identify molecules in data from

interstellar spectra. Studying cold molecules in the lab can also help understand the chemistry of combustion and the atmosphere by isolating short-lived intermediate radicals and ions that play an important role[9, 10]. The OH radical, which is the subject of this thesis, plays an important role in the chemistry of the atmosphere,[11] combustion,[12, 13] and even the interstellar medium.[14, 15] Laboratory experiments involving spectroscopy of cold OH radicals have been used alongside data from interstellar OH megamasers to constrain the time variation of fundamental constants.[1]

1.2 Cold Molecular Collisions

The study of collisions involving cold neutral molecules is also an area of particular research interest. In the cold-collision regime, the cross sections and products of interactions become largely dependant on the details of the interaction potential. Resonances have been observed due to the quantization of internal states of the constituents and the partial waves of the interaction energy. [16, 17, 18]The rapid advancement of experimental techniques has begun to catch up with theoretical techniques for approximating interaction potentials. A major contributor to the complexity of cold molecular collisions is the large anisotropy that can dominate long-range interactions. Experiments that push the energy of collisions to colder regimes where theoretical models may differ can help refine these models. [19].

In order to study an interaction, an experimenter needs a method to bring the species together and a method to detect the products of the interaction. Experiments that study interactions between cold molecules usually bring collision partners together in three main ways. First is to merge or cross two molecular beams. Merged beams can allow for high resolution tunability of the collision energy by changing the beam crossing angle or by directly controlling the velocity of the species with a decelerator.[20, 21, 22] Higher resolution can also be gained by exploiting the correlation between velocity at different positions in a moving beam. Second is to have a molecular beam impinging on a trapped sample. For both types beam experiments, the interaction time is limited by the length of the interaction region and the velocity of the beams. Beam-trap experiments do, however, allow many pulses of the beam to impinge on the trapped sample.

The third method is to trap both collision partners in the same region of space. This method can increase the sensitivity to more rare collision events by increasing the interaction time. The co-trapped environment can also allow inelastic and elastic collisions to be distinguished more directly. Elastic collisions will lead to a thermalization of the collision partners, and this can be seen by probing the energy distribuition. Inelastic collisions, on the other hand, will cause a change in the quantum state. If the molecule is transferred to a non-trapped state, its loss from the trap can be detected. Of particular interest to this experiment is the case of a trapped molecule colliding with a trapped atom. This type of experiment has recently been achieved for Li+O_2[23], N+NH[24], Rb+ND_3[25, 26], and Rb+CaF[27]. In this experiment, we study collisions of cotrapped Rb+OH.

1.3 Cold Molecule Production

The production of cold molecules can be accomplished by a wide range of techniques. These techniques are typically categorized into direct and indirect methods. Direct methods take a preexisting molecule and cool it down from some high initial temperature. The most common technique is known as supersonic expansion. Using a supersonic expansion, any molecule that can be vaporized can be entrained in a beam of rare gas can be cooled to the Kelvin regime. Other direct cooling methods involve removing heat energy from the molecule through interactions with light, fields, or atoms. Recent advancements in this field have involved direct laser cooling of molecules, even allowing molecules to be trapped in a magneto-optical trap (MOT). [28, 29, 30] Direct laser cooling of molecules, however, requires particular criteria of the energy level structure. The branching ratio for spontaneous emission into the ground cooling state must be large enough and the number of transitions with a non-trivial branching ratio must be low enough to minimize the number of repumping laser wavelengths needed. These criteria are not met in most molecules. The process of directly cooling one species with another is known as sympathetic cooling. Sympathetic cooling has been accomplished by using ions to cool ions[31], ultra cold atoms to cool atoms,[32] and ultra cold atoms to cool ions.[33] The current frontier in sympathetic cooling is the prospect of using ultra cold atoms to cool cold molecules, moving these molecular species from the millikelvin to

microkelvin regime.

Indirect cooling methods bring together ultracold atoms to form cold or ultracold molecules. The molecules are created from ultracold atoms by either photo-association [34] or magneto-association[35]. Molecules formed by indirect methods can be have high densities and ultracold temperatures (100's of nK). However, the number of species that can be created via these methods is severely limited. Currently, the molecules are limited to diatomic molecules that can be formed from atoms that can be easily laser cooled and trapped, such as alkali and alkaline-earth elements.[36, 37, 38, 39] Furthermore, the accessible quantum states are limited by the potential energy surfaces, which must allow free to bound transitions for association and bound to bound levels for stimulated emission in an energy regime that is accessible by high precision lasers. Indirect cold molecule production techniques have led to many high impact studies of ultracold physics and chemistry.[40, 41, 42, 43] However, in order to produce cold molecules that are traditionally chemically important, direct cooling is necessary and most molecules are limited to the 1K temperature regime from supersonic expansion.

1.4 The OHRbIT Experiment

In this thesis, we describe the OHRbIT Experiment (**OH** and **Rb I**nteracting in **T**raps). With this experiment, we seek to measure the cross sections of collisions between cold OH molecules and ultracold Rb atoms in a co-trapped environment. Rubidium atoms are trapped in a quadrapole magnetic field at a temperature of $T \sim 500\mu K$. The magnetic coils that produce the trapping fields sit outside the vacuum chamber on movable tracks. The atoms are transported through the vacuum chamber to overlap with an electrostatic quadrapole trap that is used to trap OH molecules. After the atoms are in place, the cold OH molecules are created in a supersonic expansion. The OH molecules are slowed using a Stark Decelerator and trapped in the electric quadrapole trap with a temperature of $\sim 50mK$. The cross sections of the interaction are extracted from measurements of the evolution of the number and energy distribution of the trapped OH molecules.

The contents of this thesis are organized as follows. Chapter 2 describes the quantum me-

chanical properties of the OH radical and how it behaves in external fields. We also detail the process we use to produce a molecular beam of cold OH radicals. Chapter 3 describes how we exploit the behaviour of OH in an electric field to slow our beam of cold OH radicals in a process known as Stark Deceleration. In Chapter 4, we discuss how OH can be detected in a cold molecular beam experiment. We describe a 1+1' REMPI detection scheme for OH radicals and the advantages of using REMPI over LIF. In Chapter 5, we describe the production of the 118 nm VUV light required for the REMPI scheme. In Chapter 6, we describe how we trap OH in an electrostatic trap. We also discuss how the new REMPI scheme can be used to measure the density distribution of the trapped OH to elucidate the dynamics of the cloud. In Chapter 6, we discuss the combination of our OH trapping experiment with a Rb trapping experiment to study collisions between Rb and OH. We discuss the theoretic predictions and the expectations of the experiment. We present measurements that demonstrate collisions between OH and Rb and estimate cross sections from these measurements. We also discuss future work to extract the inelastic and elastic cross sections using Monte Carlo simulations.

Chapter 2

The OH Molecule: Structure and Production

2.1 Introduction

In this thesis, the main molecule of interest is the neutral OH radical. In order to understand the methods used to manipulate and detect OH, some understanding of the molecular structure is necessary. In this chapter, I will discuss the molecular structure of OH and how the relevant molecular states react to electric and magnetic fields. I will also describe the process of making our molecular beam of nearly state-pure OH radicals.

2.2 Molecular Structure

The description of molecular energy level structure is much more complicated than atomic structure. The structure of atoms is well described by the behavior of the electrons orbiting an approximately fixed nucleus. Whereas for molecules, the relative motion of different nuclei needs to be accounted for as extra degrees of freedom for energy to be stored in. The rich spectroscopic structure of molecules , while complicated to describe, is one of the factors that make the study of molecular spectroscopy interesting and useful.

In order to simplify the description of molecular wavefunctions, we can apply the Born-Oppenheimer approximation. Since the mass of the nuclei is many orders of magnitude larger than the mass of the electrons, the motion of nuclei is much slower compared to the orbital motion the electrons. The Born-Oppenheimer approximation assumes that the motion of electrons happens instantaneously relative to nuclear motion. The Hamiltonian describing the molecule, H_{mol}, can

be separated into the parts that describe the electron orbit of the nuclei, H_{elec}, and the part that describes the relative motion of the nuclei, H_{nuc}. The nuclear motion can further be separated into rotation about the center of mass and vibrations that change the equilibrium bond lengths

$$H_{mol} = H_{elec} + H_{vib} + H_{rot}, \tag{2.1}$$

The total molecular wave function, Ψ_{mol}, is then separable into the product of the eigenfunctions of the separate electronic, vibrational, and rotational hamiltonians

$$|\Psi_{mol}\rangle = |\Psi_{elec}\rangle\,|\Psi_{vib}\rangle\,|\Psi_{rot}\rangle\,. \tag{2.2}$$

The energy of the molecule is then the sum of the separate electronic, vibraitional, and rotational energies

$$E_{mol} = E_{elec} + E_{vib} + E_{rot}, \tag{2.3}$$

The energy associated with each of these separate degrees of freedom also occurs on different energy scales. The energy difference between different electronic levels is typically on the order of eV's, or 10,000's of cm^{-1}. Exciting a molecule to the next electronic level typically requires a laser with wavelengths in the visible or UV part of the spectrum. Vibrational energy is the next largest scale, with vibrational energy levels typically being separated on the order of 1000 cm^{-1}. Excitation between vibrational levels is typically achieved with an infrared laser. Rotational energy level splittings are the lowest energy, being typically on the order of 10's-100's of cm^{-1}. The energy scale of rotations cooresponds to the microwave region of the spectrum.

2.2.1 OH Electronic Structure

In molecular orbital theory, molecular orbitals are described as linear combinations of atomic orbitals. The ground electronic states of the atomic constituents of OH are

- H: $(1s)\quad {}^2S$
- O: $(1s)^2(2s)^2(2p)^4\quad {}^3P$

These combine to form the molecular orbitals

- OH: $(1s\sigma)^2(2s\sigma)^2(2p\sigma)^2(2p\pi)^3$

This combination of orbitals represents an open shell radical with an unpaired electron in the one of the $(2p\pi)$ orbitals. This combination of orbitals gives four possible term symbols: $^2\Sigma^-$,$^4\,\Sigma^-$,$^4\,\Pi$,$^2\,\Pi$. The potential energy curves for OH are shown in Fig.2.1. The only bound state corresponding to the this configuration is the $^2\Pi$ which is the electronic ground state.

This electronic state can be further divided by fine structure splitting. The value of the projection of the orbital angular momentum onto the internuclear axis, Λ is given by the letter of the term symbol, $\Pi \rightarrow |\Lambda| = 1$. The superscript of the term symbol is $2|\Sigma| + 1 = 1 \rightarrow |\Sigma| = 1/2$. The total angular momentum can take on the values $J = |\Lambda| \pm |\Sigma| = 1/2$ and $3/2$.

There are a total of four bound states, with the first excited state $A^2\Sigma^+$ resulting from the promotion of a $(2p\sigma)$ electron to occupy the vacant $(2p\pi)$ orbital. This excited state lies approximately 4 eV above the ground state and is accessible by excitation by UV lasers. Resonant excitation to the $A^2\Sigma^+$ state is typically used in detection of OH.

2.3 Hund's Coupling Cases

In atoms, the electronic spin angular momentum S couples with the electronic orbital angular momemtum **L** to provide an energy splitting between elecronic energy levels with the same **L** but different **S**. This spin orbit coupling arises from the considering the frame of reference of the electron, which sees a nucleus orbiting it: a moving charge which creates a magnetic field that interacts with electrons magnetic dipole moment. Likewise, in molecules the relative motion of electrons and nuclei leads to coupling between different spins and angular momenta. The various angular momentum vectors that lead to coupling interactions are:[45]

- **L**, Orbital electronic angular momentum
- **S**, Electronic spin angular momentum

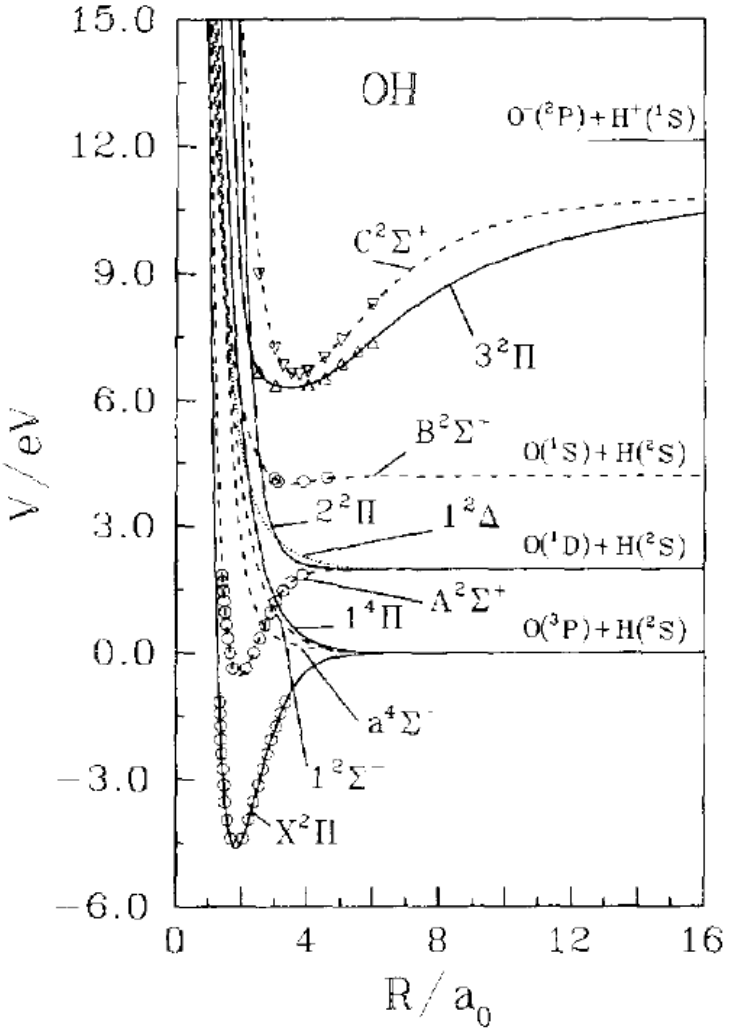

Figure 2.1: Energy curves showing the possible states of the OH molecule. From[44] Bound and unbound molecular states are derived from combinations of atomic states. The energy of a molecular state at large internuclear distance approaches the combined atomic energy.

- **J**, Total angular momentum
- **N**, The total angular momentum excluding electron spin, **N** = **J** -**S**
- **R**, Rotational angular momentum, **R** = **J** - **L** -**S**

Clearly, the existence of so many competing couplings would be overwhelming to attempt a full description. However, by considering the relative strengths of the interactions, one can construct a simplified picture that can roughly diagonalize the spin orbit Hamiltonian with nicely defined quantum numbers. Five such cases have been described and are known as Hund's cases. Labeled (a) through (e), Hund's cases (a) and (b) are the most common and relevant to the OH molecule.

The first and most common Hund's case, case (a) depicted in Fig. 2.2, is defined by two dominant interactions. First, the orbital angular momentum L is strongly coupled to the internuclear axis by electrostatic forces. Second, a strong spin-orbit interaction couples the electronic spin angular momentum **S** to **L**, effectively coupling S to the internuclear axis. The projection of **S** and **L** onto the internuclear axis, Σ and Λ respectively, sum to give $\Omega = \Sigma + \Lambda$ which is a good quantum number. The total angular momentum is then defined by J = Ω + R. The ground electronic state of OH ($2p\pi$) is best described by Hund's case (a), and the good quantum numbers are Σ, Λ, Ω, and J.

In Hund's case (b), the spin orbit coupling is much weaker. Depicted in Fig. 2.3 **L** is coupled to the internuclear axis, but **S** is not. The good quantum numbers in this case are Λ, N, and J. The first excited state of OH, $A^2\Sigma^+$, is best described by Hund's case (b).

2.4 OH Rotational Structure

The rotation of diatomic molecules is often treated with the rigid rotor model, where the two atoms with masses m_1 and m_2 are assumed to have a fixed distance, r. From classical mechanics, the energy associated with rotations in this case is

$$E_r = \frac{1}{2} I \omega^2 \tag{2.4}$$

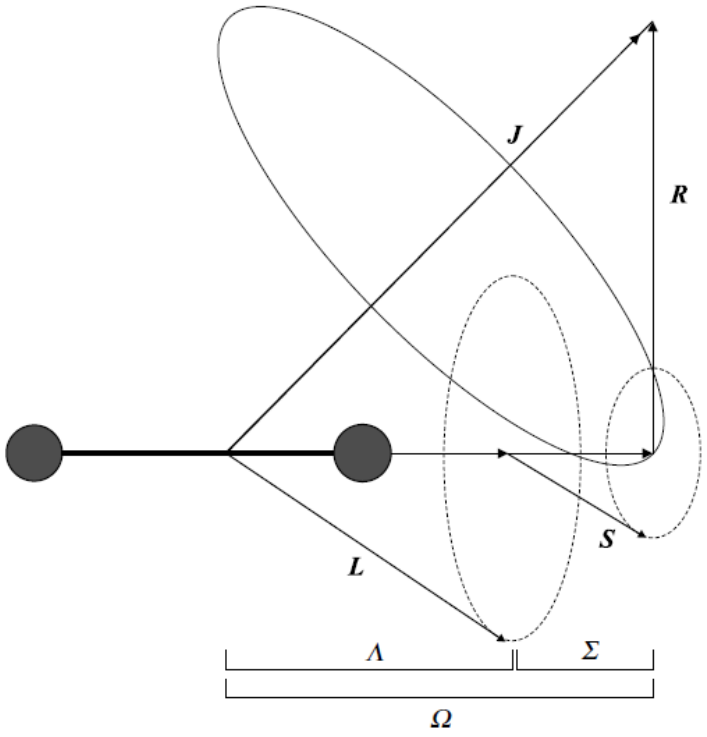

Figure 2.2: Diagram of vector coupling for Hund's Case (a). From [46]

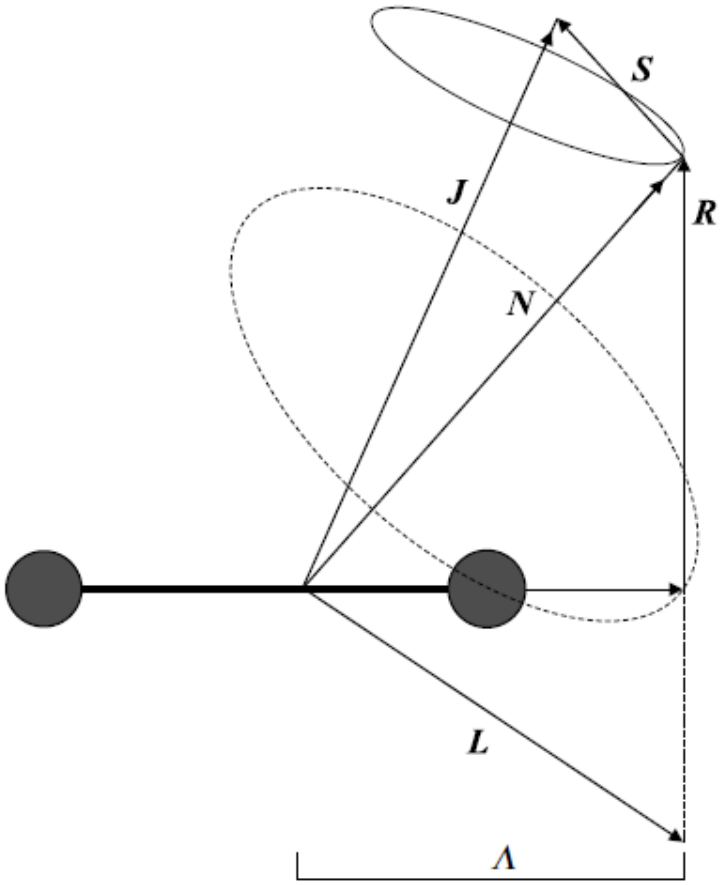

Figure 2.3: Diagram of vector coupling for Hund's Case (b). From [46]

where ω is the frequency of rotation. I is the rotational moment of inertia given by

$$I = m_1 r_1^2 + m_2 r_2^2 = \mu r^2 \tag{2.5}$$

where r_1 and r_2 are the distances from the center of mass to the respective nuclei and μ is the reduced mass

$$\mu = \frac{m_1 m_2}{m_1 + m_2} \tag{2.6}$$

The angular momentum of the system, given by $L = I\omega$, can be substituted into Equation (2.4) to give

$$E_r = \frac{L^2}{2I} \tag{2.7}$$

The quantum Hamiltonian is defined by substituting the rotational angular momentum operator, $\mathbf{R}$, for the classical angular momentum

$$H_r = \frac{\hbar^2}{2I}\mathbf{R}^2 = B\mathbf{R}^2 \tag{2.8}$$

where B is the rotational constant. In a Hund's case (a) molecule, like the ground state $^2\Pi$ states of OH, $\mathbf{R} = \mathbf{J} - \mathbf{L} - \mathbf{S}$ and the Hamiltonian becomes

$$H_r = B(\mathbf{J}^2 + \mathbf{L}^2 + \mathbf{S}^2 - 2\mathbf{J}\cdot\mathbf{L} - 2\mathbf{J}\cdot\mathbf{S} + 2\mathbf{L}\cdot\mathbf{S}) \tag{2.9}$$

The rotational energy is given by

$$H_r = B(J(J+1) + S(S+1) + 2\Lambda\Sigma + \Lambda^2 - 2\Omega^2) \tag{2.10}$$

The rotational constant B will be different for each electronic and vibrational energy level, and for the ground state of OH $B = 18.534 cm^{-1}$. The rotational energy levels for the OH ground state are plotted in Figure (2.4). Each new rotational level increases the value of J by 1 while the other values are constant. Levels can be split between the $^2\Pi_{3/2}$ and $^2\Pi_{1/2}$ manifolds.

2.4.1 Lambda Doubling

Another important factor in the structure of diatomic molecules is parity. The parity, ϵ, of a state determines whether the sign of the overall wavefunction changes sign upon inversion, or a

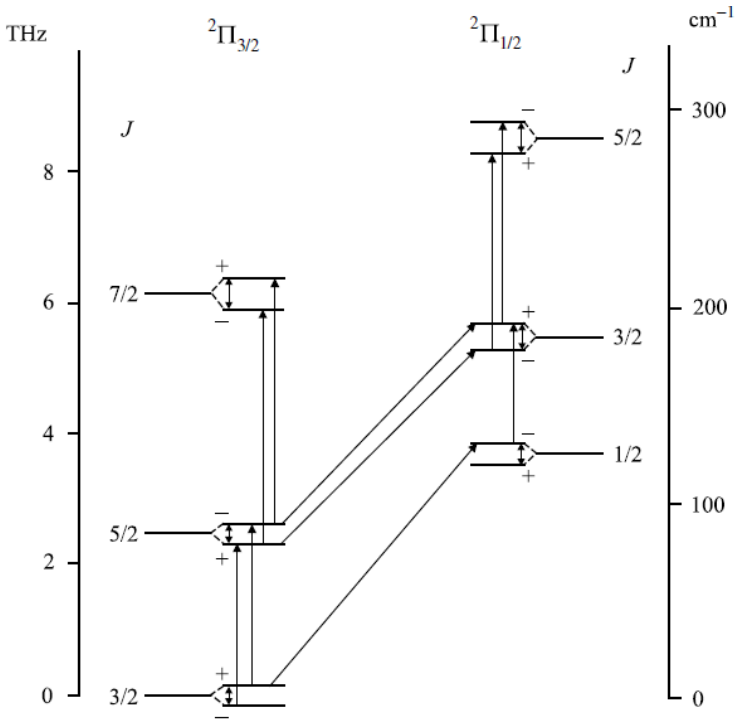

Figure 2.4: Rotational energy levels of the ground state of OH. From [46]

reflection of all particles at the origin. If the wavefuction is unchanged, the parity is $\epsilon = +1$. If the sign of the wavefunction flips, the parity is $\epsilon = -1$. The parity of a rotational state alternates between + and - for even and odd levels of J respectively. For electronic states with $\Lambda \neq 0$, like the ground $^2\Pi$ state of OH, there are two possible orientations of Λ. Parity states are made from linear combinations of the two orientations, and each rotational state, J, has a positive and negative parity level. The degeneracy between the two parity states is lifted by a weak spin-rotation coupling, giving rise to a Lambda Doublet splitting. In the $^2\Pi_{3/2}$ state of OH, the ground rotational state has a lambda doublet splitting of $\Delta = 0.056cm^{-1}$. In Figure 2.4, the lambda doublet splitting is exagerated, but demonstates the important characteristics. The splitting grows with increasing J, and the parity of the upper and lower states flips based on the parity of the rotational state.

2.5 OH in External Fields

2.5.1 OH in Electric Fields

When a molecule with an electric dipole moment encounters an electric field, it will experience a Stark shift. The Hamiltonian for the Stark effect is given by

$$H_S = -\mathbf{d}_e \cdot \mathbf{E}, \tag{2.11}$$

where $\mathbf{d}_e$ is the molecule's electric dipole moment and $\mathbf{E}$ is the magnetic field vector. For a diatomic molecule electric dipole moment points along the internuclear axis. As the molecule rotates, the components of the dipole moment perpendicular to the rotation axis average out to zero. The time averaged component that survives is the projection of d_e onto $\mathbf{J}$,

$$< d_J >= |d_e| cos(z, \mathbf{J}) = \frac{dK}{\sqrt{J(J+1)}} \tag{2.12}$$

where K is the projection of $\mathbf{J}$ onto the internuclear axis, which for a Hund's case (a) molecule $K = \Omega$. The Hamiltonian then becomes

$$H_Z = -d_J \mathbf{J} \cdot \mathbf{E}, \tag{2.13}$$

We can evaluate the Hamiltonian in the $|JM_J\Omega\rangle$ basis by taking the magnetic field to be along the z-axis

$$E_Z = \langle JM_J\Omega|H_S|JM_J\Omega\rangle = -dE\frac{M_J\Omega}{J(J+1)} = -d_{eff}E \tag{2.14}$$

where M_J is the projection of J along the z-axis.

The above treatment is a first-order approximation that ignores the effects of parity. In the parity basis, Equation (2.14) represents the off diagonal elements, and the diagonal elements give the zero-field lambda doublet splitting.

$$H = \begin{pmatrix} -\Delta/2 & -d_{eff}E \\ -d_{eff}E & \Delta/2 \end{pmatrix} \tag{2.15}$$

Solving for the eigenvalues of this matrix gives the Stark energy splitting

$$\Delta E_S = \frac{\Delta}{2} \mp \sqrt{(\frac{\Delta}{2})^2 + (dE\frac{M_J\Omega}{J(J+1)})^2} \tag{2.16}$$

where the $\mp$ symbol is used to denote that the sign is opposite of the parity state (the energy of positive parity states decreases with electric field and negative parity states increase). Stark shifts are plotted in Figure 2.5. For small electric fields, the first order Stark shift is comparable to the Lambda doublet splitting and the over all shift is quadratic in the electric field. For large electric fields, the effect is linear.

2.5.2 OH in Magnetic Fields

In the OHRBIT experiment, the OH molecules will also experience magnetic fields on the order of 100's of gauss. So, we must also understand how magnetic fields affect the internal state of OH. The interaction of a molecule's magnetic dipole moment with an external magnetic field is know as the Zeeman effect. The Hamiltonian for the Zeeman efect is given by

$$H_Z = -\mu_m \cdot \mathbf{B}, \tag{2.17}$$

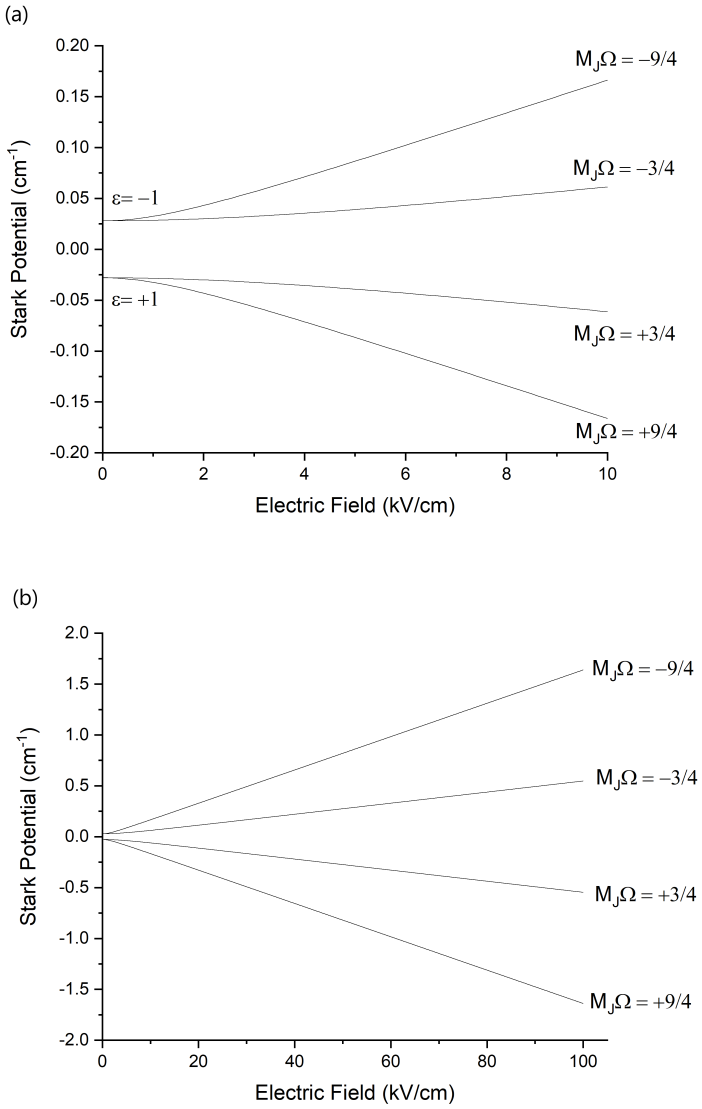

Figure 2.5: Stark Shifts in OH for (a) small and (b) large electric fields.

where μ_m is the molecule's magnetic moment and $\mathbf{B}$ is the magnetic field vector. The magnetic moment of a molecule

$$\mu_m = -\mu_b(\mathbf{L} + g_e\mathbf{S}), \tag{2.18}$$

includes contributions from both the orbital angular momentum, $\mathbf{L}$, and the spin angular momentum, $\mathbf{S}$, where μ_b is the Bohr magneton and $g_e \approx 2$ is the electron g-factor. For a Hund's case (a) molecule, L and S are coupled to the internuclear axis with projections Λ and Σ. The magnetic moment points along the molecular axis with magnitude

$$\mu_\Omega = \mu_B(\Lambda + g_e\Sigma) \tag{2.19}$$

While the molecule rotates, the molecular axis precesses around $\mathbf{J}$. The time averaged magnetic moment along $\mathbf{J}$ due to this precession is given by

$$< \mu_J >= \mu_\Omega cos(z, \mathbf{J}) = \mu_B(\Lambda + g_e\Sigma)\frac{\Omega}{\sqrt{J(J+1)}} \tag{2.20}$$

Equation (2.17) then becomes

$$H_Z = -\mu_J \mathbf{J} \cdot \mathbf{B}, \tag{2.21}$$

We can evaluate the Hamiltonian in the Hunds case (a) basis $|JM_J\Omega\epsilon\rangle$, in which the Hamiltonian is diagonal. By taking the magnetic field to be along the z-axis

$$E_Z = \langle JM_J\Omega\epsilon|H_Z|JM_J\Omega\epsilon\rangle = \mu_b\mathbf{B}(\Lambda + g_e\Sigma)\frac{\Omega M_J}{J(J+1)}. \tag{2.22}$$

where M_J is the projection of J along the z-axis.

In this experiment we are mainly concerned with the $X^2\Pi_{3/2}$ ground state of OH, in which case Equation (2.22) reduces to

$$E_Z = \frac{4}{5}\mu_B M_J B, \tag{2.23}$$

Equation (2.23) is plotted in Figure 2.6 for each M_J level in each parity state. Crossings between Zeeman levels with different parities occur at 496 G, 744 G, and 1488 G.

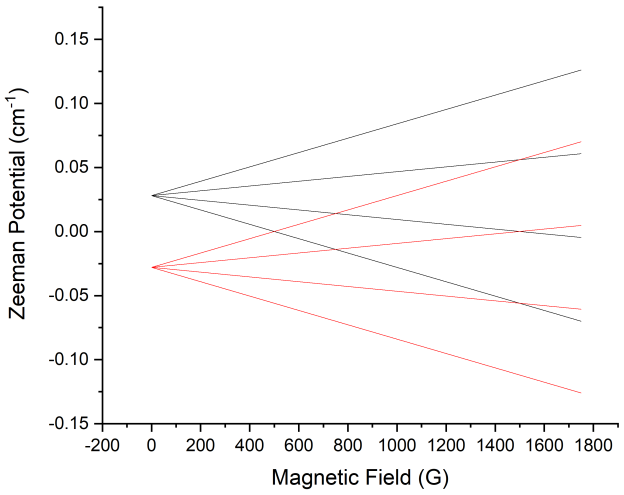

Figure 2.6: Zeeman Shifts in OH. Black curves are negative parity, Red curves are positive parity.

2.5.3 OH in Combined Fields

In the presence of both electric and magnetic fields, the Hamiltonian is the sum of the Stark and Zeeman

$$H_X = -\mu_m \cdot \mathbf{B} - \mathbf{d}_e \cdot \mathbf{E}. \tag{2.24}$$

While the electric and magnetic dipole moments are alligned to the internuclear axis and will always point in the same (or opposite) direction in the molecular frame, the electric and magnetic fields are free to point whereever the experiment demands. We can let the magnetic field $\mathbf{B}$ lie along the z-axis and define the angle β to be the angle between $\mathbf{B}$ and $\mathbf{E}$. The Hamiltonian can for the $^2\Pi_{3/2}$ state of OH can be written [47]

$$\begin{pmatrix}
-\frac{\Delta}{2}-\frac{6}{5}\mu_B B & 0 & 0 & 0 & \frac{3}{5}dEcos\beta & -\frac{\sqrt{3}}{5}dEsin\beta & 0 & 0 \\
0 & -\frac{\Delta}{2}-\frac{2}{5}\mu_B B & 0 & 0 & -\frac{\sqrt{3}}{5}dEsin\beta & \frac{1}{5}dEcos\beta & -\frac{2}{5}dEsin\beta & 0 \\
0 & 0 & -\frac{\Delta}{2}+\frac{2}{5}\mu_B B & 0 & 0 & -\frac{2}{5}dEsin\beta & -\frac{1}{5}dEcos\beta & -\frac{\sqrt{3}}{5}dEsin\beta \\
0 & 0 & 0 & -\frac{\Delta}{2}+\frac{6}{5}\mu_B B & 0 & 0 & -\frac{\sqrt{3}}{5}dEsin\beta & -\frac{3}{5}dEcos\beta \\
\frac{3}{5}dEcos\beta & -\frac{\sqrt{3}}{5}dEsin\beta & 0 & 0 & \frac{\Delta}{2}-\frac{6}{5}\mu_B B & 0 & 0 & 0 \\
-\frac{\sqrt{3}}{5}dEsin\beta & \frac{1}{5}dEcos\beta & -\frac{2}{5}dEsin\beta & 0 & 0 & \frac{\Delta}{2}-\frac{2}{5}\mu_B B & 0 & 0 \\
0 & -\frac{2}{5}dEsin\beta & -\frac{1}{5}dEcos\beta & -\frac{\sqrt{3}}{5}dEsin\beta & 0 & 0 & \frac{\Delta}{2}+\frac{2}{5}\mu_B B & 0 \\
0 & 0 & -\frac{\sqrt{3}}{5}dEsin\beta & -\frac{3}{5}dEcos\beta & 0 & 0 & 0 & \frac{\Delta}{2}+\frac{6}{5}\mu_B B
\end{pmatrix} \tag{2.25}$$

where the first four indices are the positive parity states with $M_J = -3/2, -1/2, +1/2, +3/2$ and the last four are the negative parity states with $M_J = -3/2, -1/2, +1/2, +3/2$. Note that the diagonal contains the lambda doublet splitting and Zeeman shift, because they do not mix parity states. The off diagonal elements contain the Stark shift, which do mix parity states.

2.6 OH Creation

When studying the physics of atoms and molecules, it is important to have a sample of cold gas-phase particles in order to minimize the potential interactions between particles. This presents a challenge, since particles tend to exit the gas phase when they are cooled to the sub Kelvin temperature regime that affords the unique quantum control that makes studying cold molecules so interesting. The solution that experimentalists have been using for decades is to entrain the molecules they want to study in a carrier gas that can collide with and cool the molecule while limiting collisions between the molecules that would cause them to cluster into liquids. The method

employed in this experiment is to entrain our molecules in a supersonic expansion of a rare gas. Illustrated in Figure 2.7, a supersonic expansion occurs when a gas is allowed to pass through an apperature between a region of high pressure and a vacuum. Collisions will tend to convert heat energy into forward velocity, making a beam that has a large velocity in the forward direction but a narrow spread of velocities cooresponding to a temperature on the order of 1K. The rare gas can also quench the internal molecular degrees of freedom, which leaves the molecules near the rovibrational ground state. The expanding gas will often be passed through another aperature in order to separate a useable portion of the beam and reduce the background gas farther down the beamline.

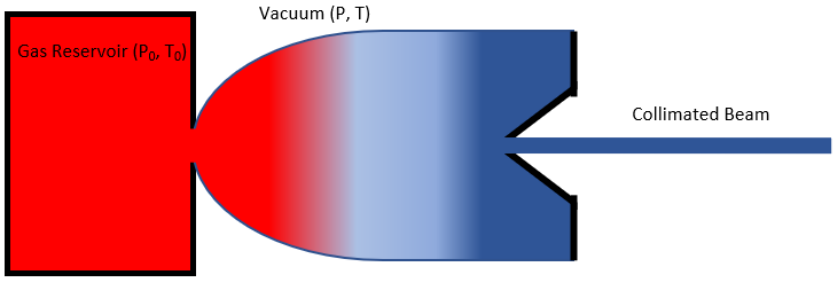

Figure 2.7: Illustration of a supersonic expansion.

The velocity of the beam can be calculated by considering the change in enthalpy across the aperature. As the gas expands into the vacuum, the pressure differential accelerates particles while converting enthalpy into forward velocity. Using the enthalpy per unit mass the equation describing this enthalpy change is[48]

$$h_0 = h + \frac{1}{2}v^2 \tag{2.26}$$

where h_0 is the initial enthalpy of the gas reservoir, h is the final enthalpy after expansion, and v

is the velocity. This can be solved to give the velocity[48]

$$v(T) = \sqrt{\frac{2k_B}{m}\frac{\gamma}{\gamma-1}(T_0 - T)} \tag{2.27}$$

where m is the mass of the carrier gas and γ is the ratio of the heat capacities at constant pressure and volume, $\gamma = \frac{C_P}{C_V}$. When using a monoatomic gas, such as a rare gas, as the carrier gas $\gamma = \frac{5}{3}$. The approximation is made that the intial temperature is much larger than the final temperature, or $\frac{T_0}{T} = \infty$, which leads to a velocity

$$v_\infty = \sqrt{\frac{2k_B T_0}{m}\frac{\gamma}{\gamma-1}} \tag{2.28}$$

The velocity can be tuned by changing the temperature of the gas reservoir, T_0. The velocity can also be changed by changing to a carrier gas with a different mass. Most often, a rare gas is used as the carrier gas. Figure 2.8 plots v_∞ versus carrier gas mass, noting the velocity for the different rare gasses at $T_0 = 300K$.

The molecular beam apparatus used in this experiment is displayed in Figure 2.9. We use Krypton as our carrier gas at a pressure of 2200 Torr. The Krypton is bubbled through a reservoir of distilled water, to seed the gas with 1% H_2O. The flow of the gas into the vacuum chamber is controlled by a piezo electric transducer (PZT) valve.[50] The PZT valve opens when a voltage (300-500V) is applied. We pulse the opening voltage for 100 μs, creating a pulsed supersonic expansion of H_2O seeded in Kr.

OH radicals are created in a discharge across the expanding gas at the exit aperature. Collisions between high energy electrons and H_2O molecules cause H_2O to fragment. For collision energies on the order of 100 V, the process that dominates is

$$e^- + H_2O \rightarrow OH(X) + H + e^- \tag{2.29}$$

where the OH(X) denotes that OH is left in the ground electronic state. A voltage of 900V is applied across the discharge electrodes for a duration of 20 μs. The relatively short pulsed discharge allows the OH to be created with a tunable mean velocity. Since the time of flight from the valve exit to the

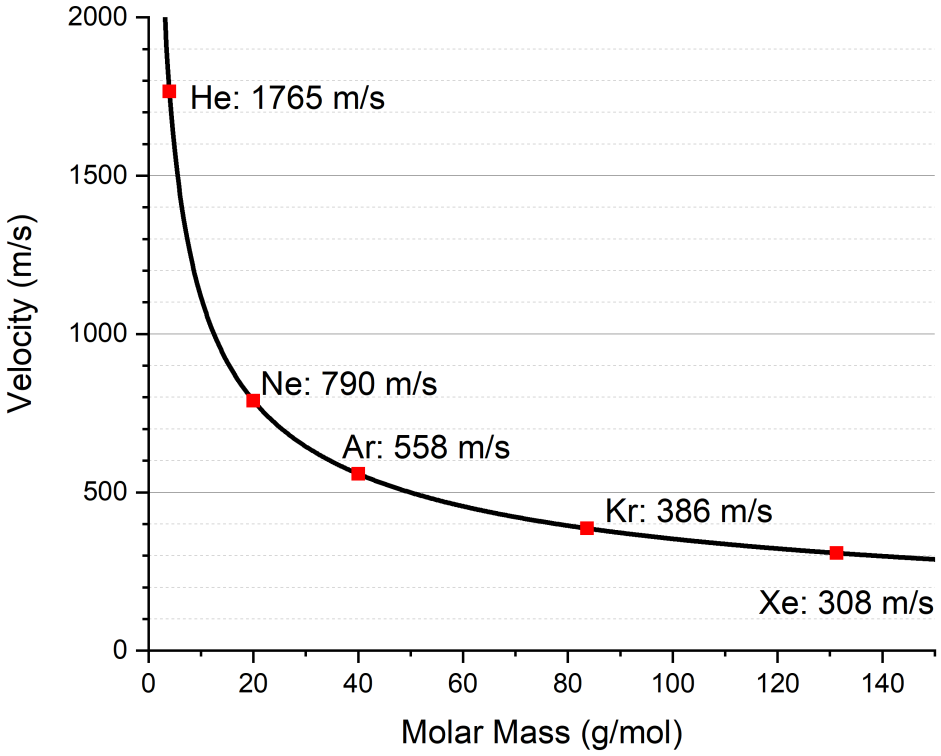

Figure 2.8: Velocity vs mass of carrier gas.

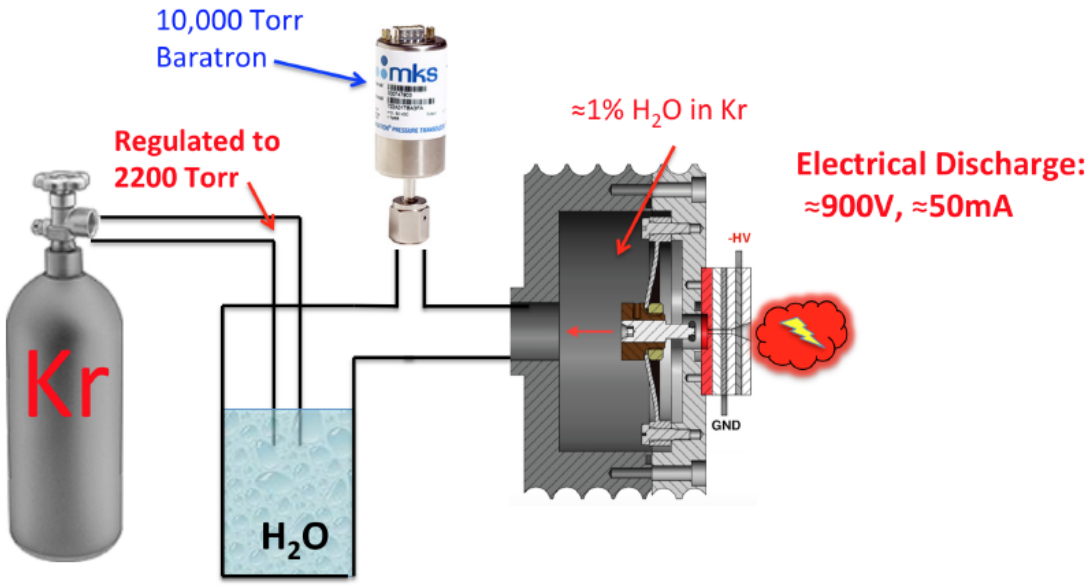

Figure 2.9: Diagram of the apparatus used for producing OH molecular beam. From [[49]]

discharge region is dependant on the velocity of the molecules, the delay between valve opening and discharge can be varied to select a different portion of the Kr/H_2O gas pulse to create the OH from. The short discharge also produces a smaller velocity distribution. Under our typical experimental conditions, the OH beam has a velocity of 420 m/s and velocity spread of 50 m/s. The beam is collimated by a skimmer as it passes into the portion of the vacuum chamber containing our Stark Decelerator.

Chapter 3

Stark Deceleration

3.1 Introduction

As described above, a supersonic expansion can produce a relatively dense sample of cold molecules. However, these cold molecules are produced with a large forward velocity, which reduces the amount of time an experimentalist has to interact with the molecules. A technique known as Stark deceleration has been demonstrated to slow fast moving polar molecules to a tunable final velocity. Stark deceleration uses spatially inhomogeneous time varying electric fields to decelerate neutral polar molecules. By changing the timing of the electric fields, the final velocity can be changed to fit the desired experiment. In this chapter, we describe the Stark Deceleration process and how we slow our OH molecules down to a velocity where they can be trapped at rest.

3.2 Stark Deceleration

To decelerate something, it must experience a force. The force to decelerate a polar molecule can be produced by exploiting the Stark potential experienced by polar molecules in an electric field. The force experienced by a particle in some potential field is given by the gradient of that potential

$$F = -\nabla U_{Stark}. \tag{3.1}$$

In the approximation of high electric fields where the Stark potential is linear, the force becomes

$$F = -\nabla(\mathbf{d}_e \cdot \mathbf{E}) = d_e \nabla|\mathbf{E}|. \tag{3.2}$$

We can see from Eq. 3.2 that the force a polar molecule feels from an electric field comes from the gradient of the electric field. Whether this force produces an acceleration or deceleration is dependent on the internal state of the molecule. In the ground state of OH, if the sign of the product ΩM_J is negative, the state is weak-field-seeking.

In order to do this in the lab, we can use electrodes to produce a large electric field in one region, like shown in Figure 3.1. When a molecule in a weak-field-seeking state approaches the region between the electrodes, it is moving from a region of low electric field to a region of high electric field. This produces a potential hill with a gradient that opposes the motion of the molecule. As it climbs the potential hill, the molecule is decelerated while trading kinetic energy for Stark potential energy. If the molecule were allowed to pass through the electrodes to the other side and over this peak in the potential energy, it would begin to accelerate back to its initial velocity. However, if the voltages on the two electrodes were quickly turned off while the molecules were still experiencing the Stark potential, that potential energy will go away without doing any work to the molecule.

The amount of energy that can be taken out by a single pair of electrodes is somewhat limited, but this can be overcome by combining many stages one after another. In this way, the molecules are constantly climbing a potential hill and losing kinetic energy, then losing the potential energy when the hill is turned off. The electric dipole moment of typical polar diatomic and simple polyatomic molecules is around 1-2 debeye, with the electric dipole moment of OH being 1.67 D. Electric fields that can be reasonably produced in a vacuum chamber between two stainless steel electrodes is 50-150 kV/cm. This means that approximately 2K can be removed per stage, and 150 stages are needed decelerate down to rest.

The Stark decelerator used in this experiment consists of 149 pairs of pin electrodes. A picture of the decelerator can be found in Figure 3.2.

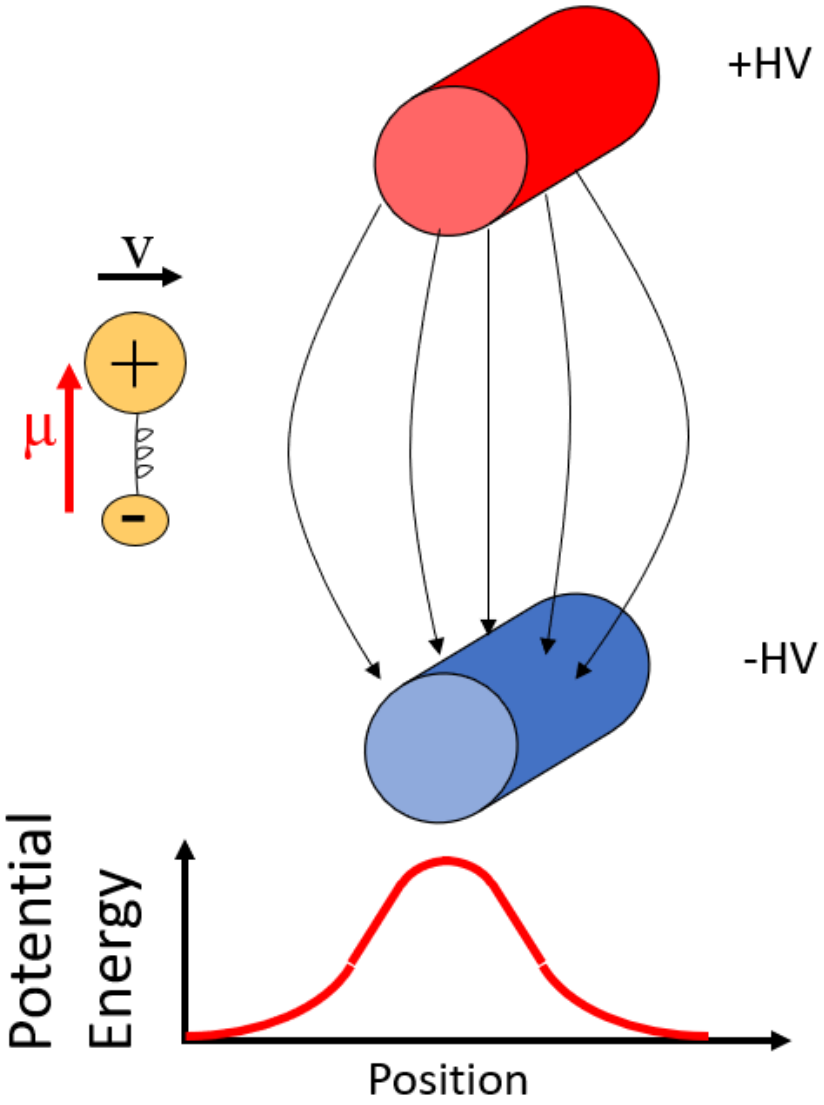

Figure 3.1: Single Pin Pair Diagram. With the electrodes held at ±HV, the molecule experiences a potential energy hill due to the Stark effect.

3.3 Operation of a Stark Decelerator

Four rods run down the length of the decelerator, in which the electrode pins are inserted. The rods are numbered 1 through 4. Pins connected to rods 1 and 4 oppose each other and make a pin pair. Pins connected to rods 2 and 3 also oppose each other and make a pin pair. The pins from rods 1 and 4 are oriented at a 90 degree angle from the pins from rods 2 and 3. The electric fields tend to keep the beam from expanding in the direction between the pins but not along the pins. So the 90 degree angle alternates between which of the transverse directions the molecules are being confined.

The voltages on the rods are switched between ground and $\pm 12kV$ by individual high voltage switches with a rise/fall time on the order of 100ns. Rods 1 and 3 will hold -12kV, while rods 2 and 4 hold +12kV. When operating the decelerator the voltages on the rods are switched between two configurations

- Rods 1 and 4 at $\pm 12kV$, Rods 2 and 3 grounded
- Rods 1 and 4 grounded, Rods 2 and 3 at $\pm 12kV$

To understand how the decelerator is operated in order to control the final velocity of the molecules, we define the synchronous molecule. The synchronous molecule is a hypothetical molecule that travels directly along the axis of the decelerator around which the timing of the decelerator is designed. The Stark potentials of an OH molecule traveling directly along the axis of the decelerator can be found in Figure 3.3. The potential is usually parameterized by $W(\phi)$ as a function of the phase angle

$$\phi = 180^\circ \frac{z}{L} \tag{3.3}$$

where z is the position of the molecule along the decelerator axis and L is the distance between similar pin pairs.

Figure 3.4 shows the path of the synchronous molecule along the potentials during deceleration. The zero of ϕ is defined to be the position where the potentials for both configurations are

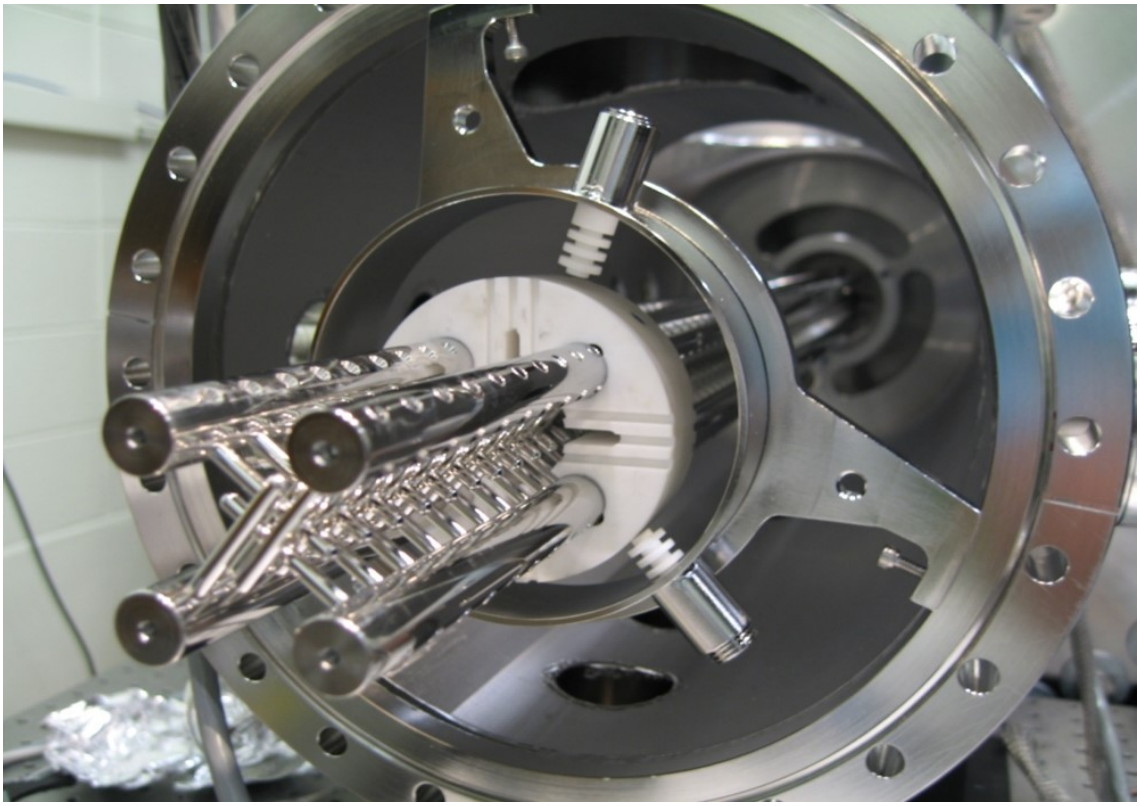

Figure 3.2: A picture of the Stark Decelerator.

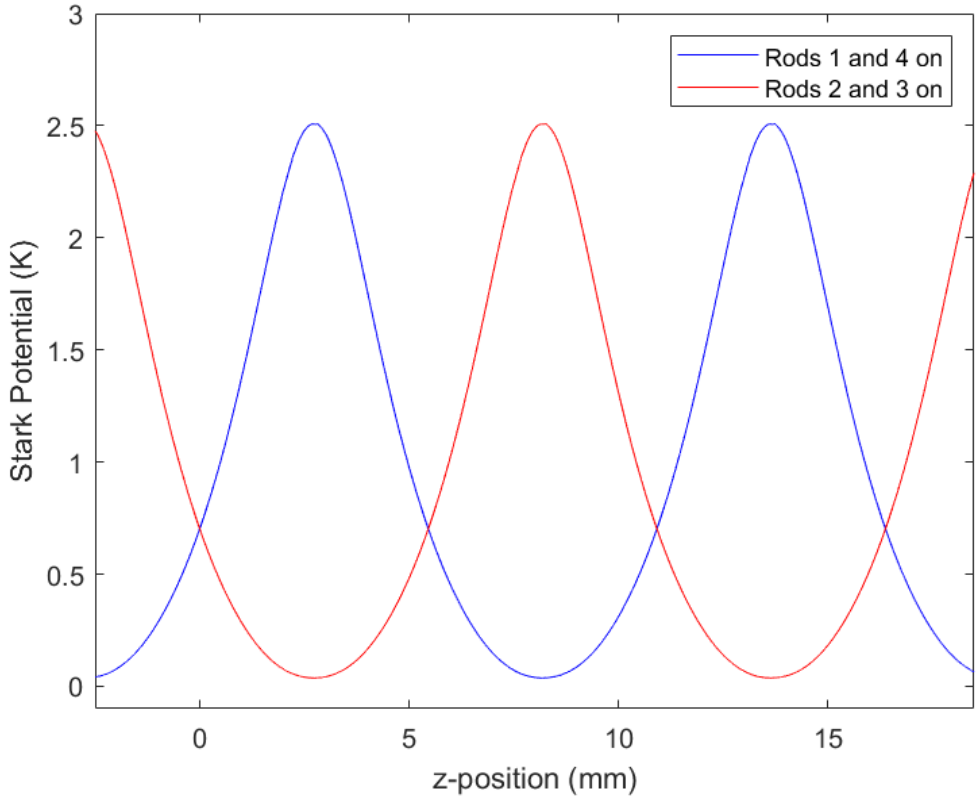

Figure 3.3: Stark Potential for the two voltage configurations. Because the rods electrically connect every 4th pin, a periodic potential is created that spans the entire decelerator.

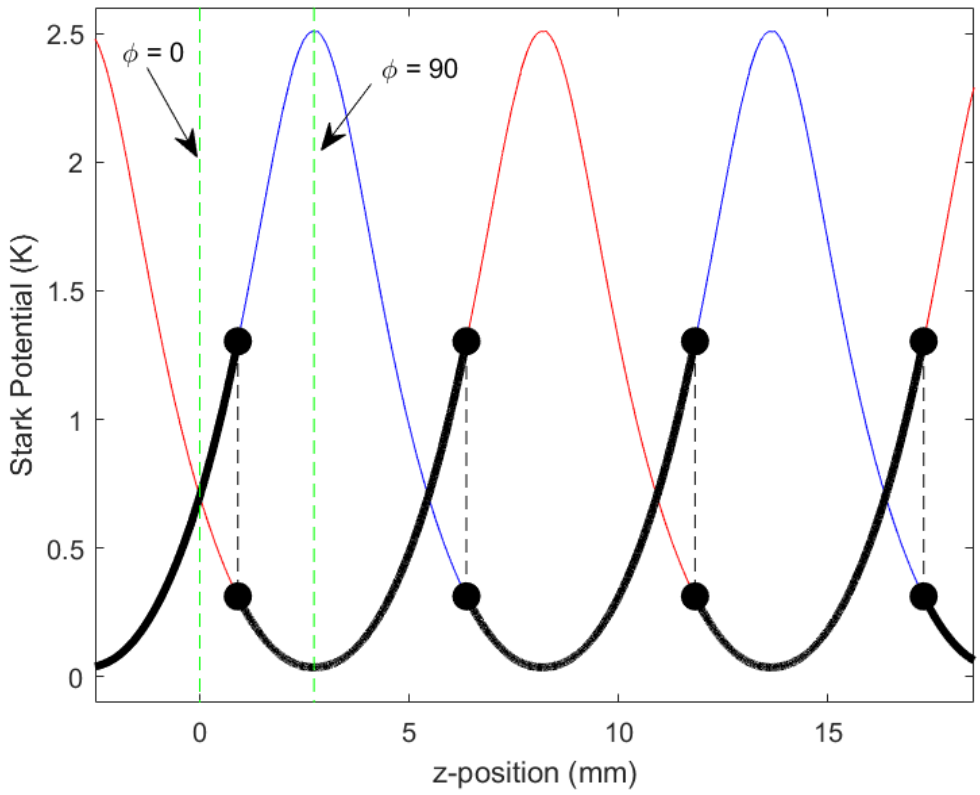

Figure 3.4: Demonstration of Deceleration. Path of the synchronous molecule along the potential energy curves are is the black line. When the sychronous molecule reaches the desired phase angle, the potential configuration is switched. The molecules lose an amount of energy ΔK, which is the difference between the potential energy curves at that phase angle.

equal, which is also halfway between the pin pairs. For a phase angle of $\phi = 0°$, the energy lost when the potentials switch is $\Delta K = 0$. The maximum amount of energy is lost when switched at $\phi = 90°$, since this phase angle lines up the maximum of the initial potential with the minimum of the switched potential. The potential after switching between configurations is just the original potential shifted by π, and the energy lost is given by

$$\Delta K(\phi) = W(\phi) - W(\phi + \pi). \tag{3.4}$$

If the phase angle of switching is kept constant, then the velocity after a number of stages, n, is given by

$$\frac{1}{2}mv_n(\phi)^2 = \frac{1}{2}mv_i^2 + n\Delta K(\phi) \tag{3.5}$$

$$v_n(\phi) = \sqrt{v_i^2 - \frac{2n\Delta K(\phi)}{m}} \tag{3.6}$$

The phase space acceptance of the decelerator is the region of the 6-D phase space that will be remain in the vicinity of the synchronous molecule and be successfully decelerated. A description of the behaviour of the molecules in the transverse dimensions can be found in [51]. In the longitudinal direction, the phase space acceptance can be derived from the potentials above. The energy lost per stage, $\Delta K(\phi)$, varies from 0 to W_{max} between $\phi = 0°$ and $90°$ and to first order is given by

$$\Delta K(\phi) \approx -W_{max} sin(\phi) \tag{3.7}$$

The average force on a molecule per stage is given by

$$\bar{F} = \frac{\Delta K}{L} = \frac{-W_{max} sin(\phi)}{L} \tag{3.8}$$

A molecule that differs in phase angle by an amount $\Delta\phi$ will experience a force relative to the synchronous molecule of

$$\bar{F}_{rel} = \bar{F}_0 - \bar{F} = \frac{-W_{max}}{L}[sin(\phi_0) - sin(\phi_0 + \Delta\phi)] \tag{3.9}$$

This force is negative for phase angles larger than ϕ_0, and positive for phase angles smaller than ϕ_0, representing a restorative force that pushes the molecule back towards the synchronous molecule. Using Newton's second law, we can derive an equation of motion

$$\frac{mL}{\pi}\frac{d^2\phi}{dt^2} - \frac{W_{max}}{L}[sin(\phi_0) - sin(\phi_0 + \Delta\phi)] = 0 \tag{3.10}$$

By numerically integrating Equation 3.10, we can find the boundary of phase space for which orbits around the synchronous molecule are stable, known as the separatrix. The separatrices for a few different phase angles are plotted in Figure 3.5. Molecules in the phase space outside of

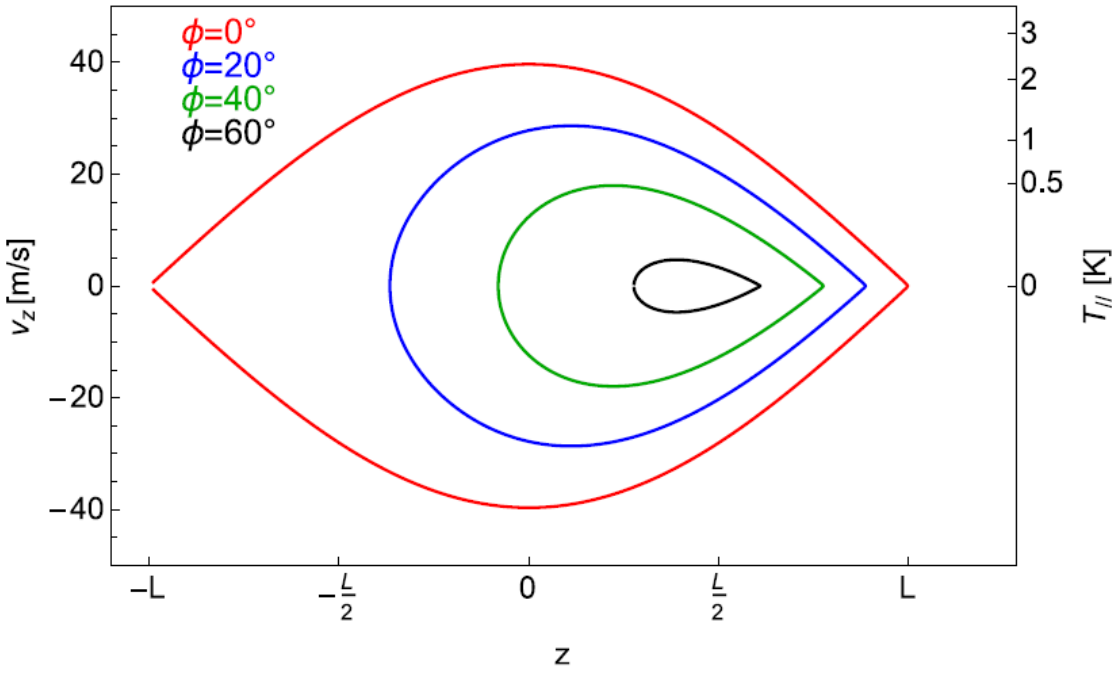

Figure 3.5: Separatrices for OH at various phase angles. From [**?**].

the separatrix are accelerated away from the synchronous molecule, while the molecules within the separatrix are decelerated with the synchronous molecule, forming a packet of decelerated molecules. The phase space volume shrinks as ϕ_0 increases, meaning the number of molecules that can be decelerated decreases as the target velocity decreases.

3.4 Alternate Deceleration Schemes

One of the main problems with the traditional pulsed pin decelerator is loss due to transverse motion of the molecules.[52, 51] Coupling between the longitudinal and transverse motion of the molecules leads to regions of the phase-space acceptance that are unstable. Alternative deceleration geometries and schemes have been designed to eliminate or overcome this problem. For pulsed pin decelerators, changing the sequence that voltages are applied can help mitigate the transverse loss.[53, 54, 55] Travelling wave ring decelerators can eliminate the transverse loss, since they produce a three dimensional trapping potential that moves along with the molecules.[56] A ring decelerator can also be operated in a pulsed mode, which still exploits the cylindrical symmetry of the decelerator to greatly reduce potential transverse loss.[57]

Recently, it has been shown that mixing in alternate voltage configurations can help provide a restoring force in the transverse direction.[58] In the traditional deceleration mode, after the voltage is switched between configurations, the molecules spend a significant amount of time between the two grounded electrodes. However, the field lines from the charged electrodes create a defocusing potential along the grounded electrodes. By applying an alternative voltage configuration between slowing stages, the transverse potentials can be changed to be focusing. Dave Reens describes in his PhD Thesis different configurations that can be achieved with varying degrees of experimental complexity.[58] These configurations are dubbed Very Strong Focusing (VSF), Strong Focusing (SF), and Focusing, in order of decreasing complexity and improvement. The voltage configurations and switching schemes are summarized in Figure 3.6.

For each of these schemes, there is an intermediate focusing stage where the molecules are better confined in the direction along the pin pair. A single stage of the deceleration sequence consists of the molecules traveling from a phase angle of $\phi = \phi_0 - 360$ to $\phi = \phi_0$. The focusing potentials are symmetric about $\phi = -180°$, and ΔK is symmetric about $\phi = 0$. So, in each of the focusing schemes, the molecules travel from a phase angle of $\phi = \phi_0 - 360$ to $\phi = -\phi_0$ on the focusing potential without a change in energy. The molecules then travel along the slowing

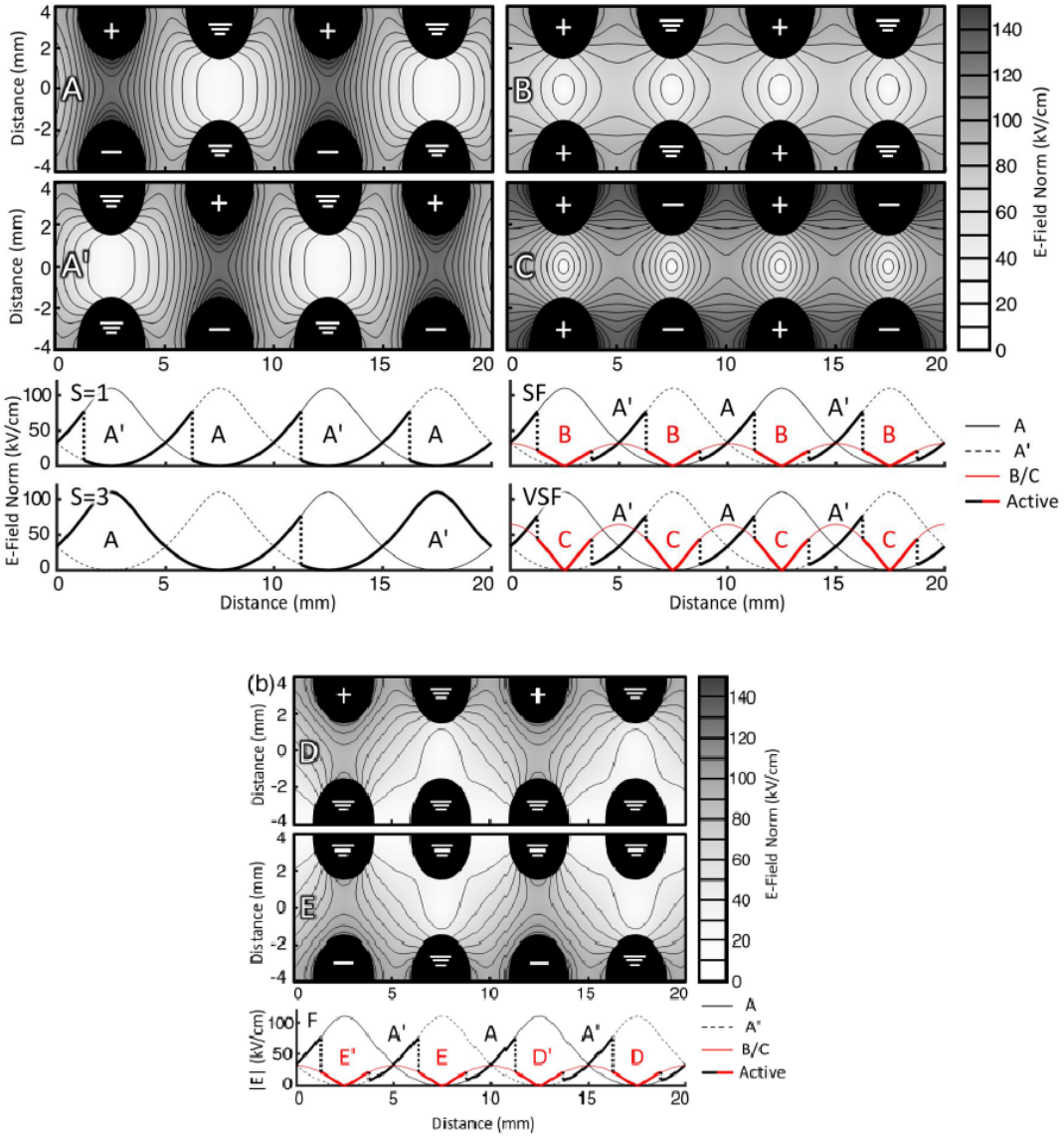

Figure 3.6: Different voltage configurations for Focusing modes. From [58].

potential from $\phi = -\phi_0$ to $\phi = \phi_0$. There is an energy drop at both potential switches, which totals to $\Delta K(\phi_0)$.

The main difference in experimental complexity is the number of high voltages switches needed to achieve the voltage configurations. In the traditional (s=1) switching scheme, a single high voltage switch is needed to switch each rod between ground and either negative or positive high voltage. This requires only four high voltage switches. In the VSF configuration, two of the rods now need to be able to switch between ground and both positive and negative high voltage. This requires a total of six switches. It also requires two pairs of switches to be operated in parallel, which is prone to breaking the switches. In the SF configuration, only one of the rods needs to be able to switch between ground and both positive and negative high voltage. This configuration requires a total of five switches, with a single pair being run in parallel. The F configuration requires no new switches and no switches to be run in parallel. The only changes that need to be made from the s=1 configuration are in the times when electrodes turn on and off. Reens saw a fourfold improvement in the number of decelerated molecules across a wide range of final velocities, including slower velocities that can be loaded into a trap.[58] For these reasons, we adopted the Focusing slowing scheme in 2019.

3.5 Deceleration Data

Figure 3.7 shows OH molecule signal for various final velocities decelerated from $v_i = 420m/s$ using the s=1 slowing scheme. The plot for each velocity has three distinct peaks, corresponding to different potential wells of the decelerator. The synchronous molecule is in the middle of the three peaks. Our goal in decelerating OH is to load the molecules into an electrostatic trap (discussed below). The trapping scheme is designed to accept molecules at $\sim 33.7m/s$. Figure 3.8 shows slowing to 33.7m/s using S=1 slowing and the Focusing scheme. The focusing scheme increases the total number of molecules in the decelerated packet by a factor of $\sim$3.

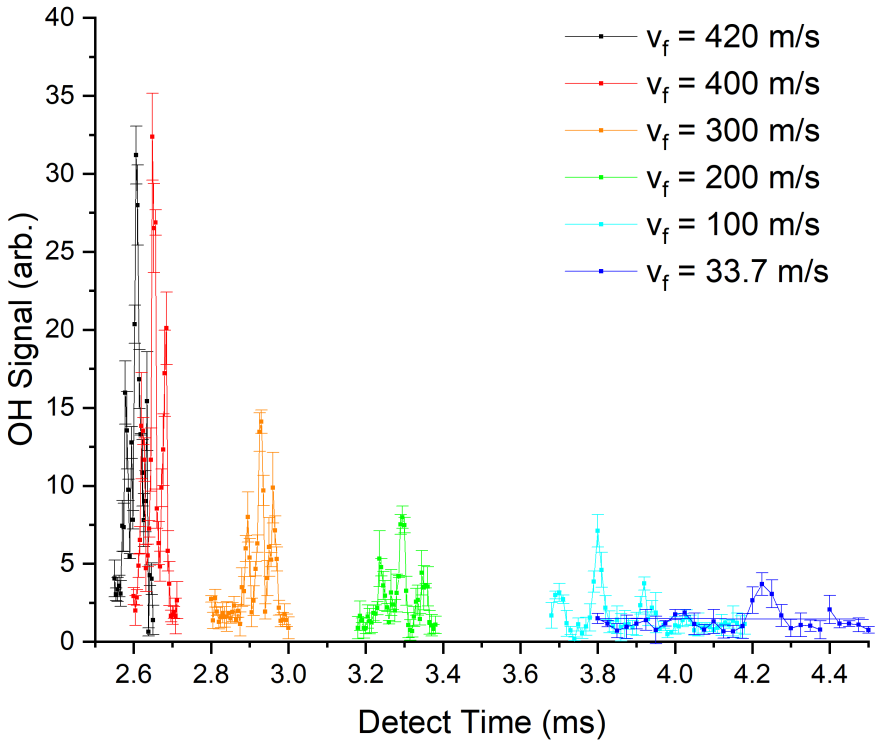

Figure 3.7: Deceleration of OH to different final velocities from an initial velocity of $v_i = 420m/s$. For $v_f = 420m/s$ the decelerator is operated at a phase angle of $\phi_0 = 0$.

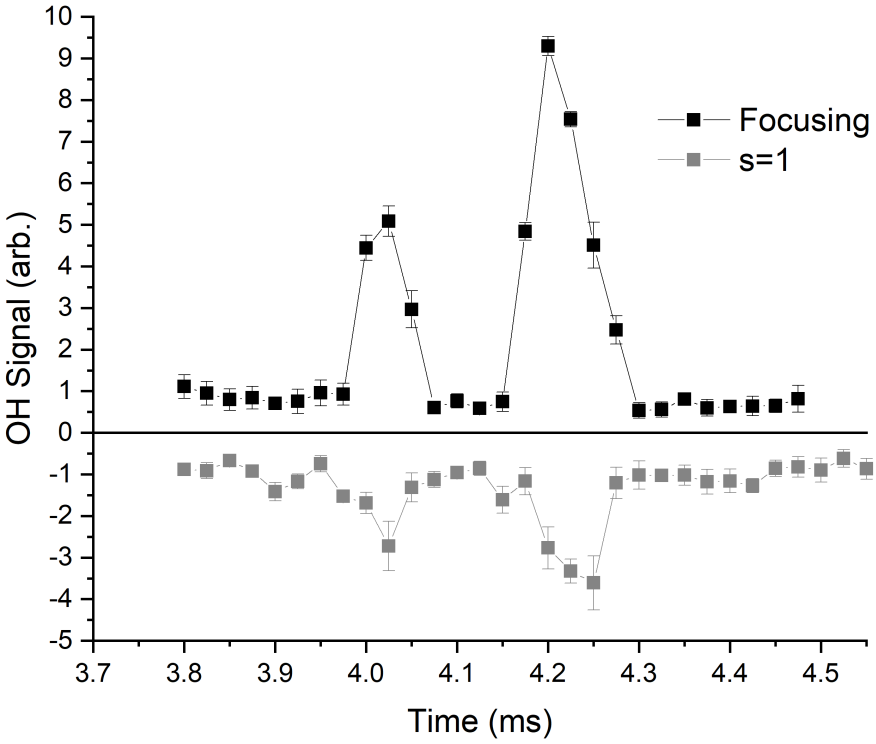

Figure 3.8: Comparison between S=1 and Focusing deceleration schemes for slowing to 33.7 m/s. The S=1 data is plotted upside down. The peak that arrives later in time around 4.2s contains the sychronous molecule and would be loaded into our trap. Integrating this later peak shows an approximately threefold increase in signal.

Chapter 4

Detection of OH

4.1 Introduction

State selective detection of molecules is an important tool for performing science with cold molecules. Detection requires a way to interact with the molecule, and a way to determine if the interaction has happened. For a detection scheme to be state selective, either the interaction or the product of the interaction must be state selective in some way. Often, the resonant absorption of a photon is chosen as the state selective interaction. From this excitation, three main methods are often employed to measure the interaction. First, the fraction of light that was absorbed can be measured. This requires a combination of molecule density and absorption cross section that is large enough to absorb enough light to have a good signal-to-noise ratio. However, this is not possible in most cold molecule experiments. Second, the excited molecule will fluoresce, producing photons that could be measured. This process is referred to as laser induced fluorescence (LIF). Third, the resonantly excited molecule can be ionized by another photon, and the amount of ions can be measured. This process is known as resonantly enhanced multiphoton ionization (REMPI). In this chapter, I will discuss how OH is traditionally detected via LIF. I will also describe our UV-VUV REMPI detection scheme for OH. The advantages and disadvantages of LIF vs REMPI are discussed.

4.2 LIF of OH

The most common technique for detecting OH is via laser induced flouresence on the A$\leftarrow$ X transition. The strongest absorption line for this electronic transition is to the $\nu' = 0$ vibrational state using a UV laser wavelength of 308 nm. However, a large Frank-Condon factor leads the strongest emission to be along the the $\Delta\nu = 0$ ($\nu' = 0 \longrightarrow \nu = 0''$) transition. Thus, most of the fluorescing light is the same wavelength as the excitation laser. While LIF detection is often accomplished in atoms by collecting fluorescence at the same wavelength as the excitation, this is not as easy in the detection of a cold molecule like OH. The UV photon in a cold molecule detection scheme will usually be produced by a pulsed laser with a pulse width too fast and repetition rate too slow to produce multiple cycles of excitation and emission. The large amount of laser light being pumped into the vacuum chamber, compared to the relatively small amount of light emitted from the molecules, would limit the signal to noise ratio of light emitted by LIF vs background light reflected from elsewhere. This would tend to limit the sensitivity of detection. Therefore, LIF detection of OH is typically acheived by exciting to the $A^2\Sigma^+(\nu' = 1)$ manifold using 281 nm light. The light emitted is mostly along the $\Delta\nu = 0$ ($\nu' = 1 \longrightarrow \nu = 1''$) transition at 313 nm, which can be spectrally filtered from the laser light.

4.3 LIF Detection Efficiency

One of the main disadvantages of LIF is a low detection efficiency that limits the signal-to-noise ratio. When the molecules fluoresce, the photons are emitted in all directions with equal probability. Only those photons that can be collected into a detection device will be counted towards the detection of the molecules. The fraction of emitted photons that can be collected to the detection device will be limited by the geometry of the system. The fraction of photons that can be detected is fundamentally limited by the solid angle around the molecules from which photons can be efficiently collected. Since the molecules being detected are in a vacuum chamber and often surrounded by electrodes or other shiny metal objects, the options for collecting a significant

fraction of the solid angle are limited. Even in the best case scenarios, where a lens can be placed inside of vacuum very close to the fluorescing region, and a parabolic mirror is used to reflect photons emitted away from the detector back towards the detector, collecting more than 5-10% is extremely difficult and often experimentally unfeasible. In our experiment, the trap electrodes and chamber design present a fundamental limit to the solid angle that can be collected. The gap between the trap electrodes in our experiment is 3 mm. There is no room to fit a lens inside the vacuum chamber, and the closest a lens can be placed is 37 mm away from the center of the trap. For a 25mm diameter lens, the fraction of the solid angle of emitted photons is limited to $4 * 10^{-3}$.

Another problem that limits the signal-to-noise of an LIF detection scheme is the filtering that is needed to distinguish between fluoresced signal photons and background noise photons. The typical instrument used to detect fluoresced photons is a photomultiplier tube (PMT). Photons impinging on the detector of a PMT create photoelectrons which are amplified through a system of cascading electrodes that produce measurable current. PMTs can be extremely sensitive and allow for detection of single photons; however, that sensitivity to signal also makes them sensitive to noise sources. Photomultiplier tubes can be designed for detecting light in the UV, but the spectral response still presents problems for our LIF scheme.

The PMT used earlier in my thesis work is a 9125B from ET Enterprises, the quantum efficiency of which can be found in Figure 4.1. The quantum efficiency for a single 313nm photon to create an electron cascade is around 30%, limiting the sensitivity to signal. While the quantum efficiency falls off quickly below 300 nm, there are $8.5x10^{15}$ photons per 6mJ pulse of our 281nm laser. Even the small fraction of the light that is reflected off windows, the chamber, and trap electrodes would present a significant amount of background photons. Furthermore, the quantum efficiency extends into the visible light, where orders of magnitude more photons are present from room lights. In order to block out these undesired wavelengths, spectral filters can be added to the optical system collecting the photons. Since the 281 nm light at shorter wavelength and the room light at longer wavelength both need to be filtered while allowing the 313 nm to be transmitted, a combination of high pass, low pass, and band pass filters are required. An analysis of the filters

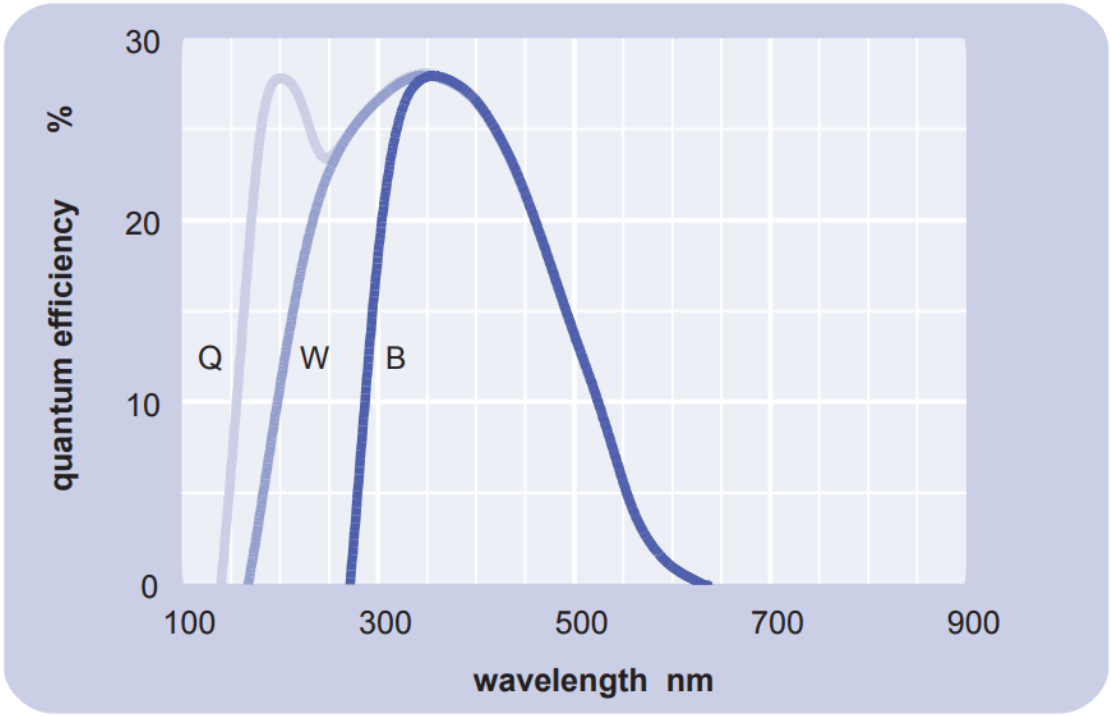

Figure 4.1: Quantum efficiency vs wavelength of the PMT (labeled B) used in previous experiments. The quantum efficiency at the flourescnence wavelength 313 nm is 26% and at the laser wavelength 281 nm is 5%.

used in our prior experiments can be found in the thesis of Travis Briles [**?**] (Chapter 6.5). Based on the filters available at the time, a stack of filters was designed that sufficiently blocked out possible noise wavelengths, but the trasmission at 313 nm was only 35.5%.

From these different loss sources, we can estimate an overall detection efficiency for LIF. For every molecule that absorbs a photon at 281 nm, the probability of detecting a photon at 313 nm using the PMT is

$$\eta = \alpha * \beta * \chi * \gamma = 2.5 * 10^{-4} \tag{4.1}$$

where α is the fractional solid angle, β is the transmission of 313 nm through the filters, χ is the quantum efficiency of the PMT at 313 nm, and γ is the branching ratio for the excited OH to emit along the $\Delta\nu = 0$ transition. This means approximately 4000 molecules need to be excited to detect a single photon. Since so many excited molecules are needed to detect a single photon, the entire cloud of molecules must be illuminated in order to produce a detectable signal. While this can be useful for determining information about the total number of molecules in the cloud, it does not allow the density profile of the cloud to be probed.

4.4 REMPI of OH

Resonantly enhanced multi-photon ionization (REMPI) is the photoionization of a molecule in a multi step process where the first step is a resonant excitation. The molecule in the excited state is subsequently ionized by the absorption of another photon. The resonant excitation step can be due to the absorption of a single photon or multiple photons. The ionization step can be due to a photon of the same color in the same laser pulse as the excitation photons, or it can be from photons of a different color. The convention for describing a REMPI scheme is A+B, where A is the number of photons required for excitation and B is the number of photons required for the subsequent ionization. If the ionization step utilizes a different color than the excitation step, this will be denoted by B' (B prime). For example, a 2+1' REMPI scheme would have a two photon absorption at one wavelength and a single photon ionization from the excited state at a different

wavelength.

The ionization potential of OH (13.017 eV) would correspond to a photon wavelength of 95.2 nm, which is in the vacuum ultraviolet (VUV) part of the spectrum. All of the excited states, except for the $A^2\Sigma^+$, also lie high enough above the ground state to require a VUV energies to access. A few REMPI techniques have been developed that utilize a single UV color for a 2+1 or 3+1 scheme through Rydberg states of the OH molecule, summarized in Figure 4.2. While ionized

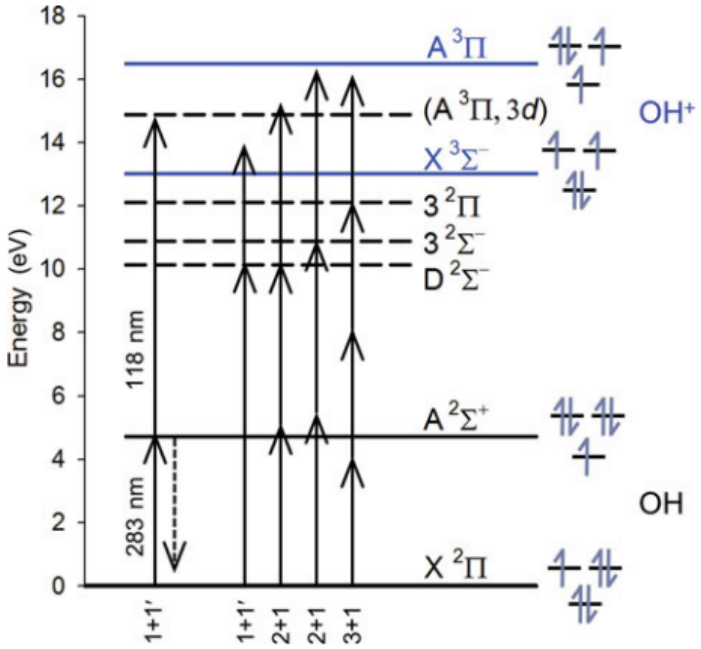

Figure 4.2: Energy diagram showing different REMPI schemes observed for ionizing OH. From [59]

OH was able to be detected with these schemes, the efficiency is limited. The excited Rydberg states have lifetimes on the order of 100 ps resulting from potential energy surfaces that cross repulsive states, which lead to dissociation before the molecule can be ionized.

A REMPI scheme that proceeds through the $A^2\Sigma^+$ state used in LIF would seem to be a good candidate, but the ionization step is a bit more complicated. The electron configuration of the ground state of the OH^+ ion and the $A^2\Sigma^+$ state are given by

- $OH^+ X^3\Sigma^- : (1s\sigma)^2(2s\sigma)^2(2p\sigma)^2(2p\pi)^2$

- $OH A^2\Sigma^+ : (1s\sigma)^2(2s\sigma)^2(2p\sigma)^1(2p\pi)^4$

Ionizing the neutral $A^2\Sigma^+$ state through the ground ionic state would require two electrons to change state and is forbidden. However, there are Rydberg states of the neutral OH molecule at higher energy than the ionization potential that subsequently autoionize. This was used by Beames et al to demonstrate a 1+1' REMPI scheme, which we use in this experiment. In this study, OH was produced in a supersonic expansion and detected by 1+1' REMPI. The first photon is a UV photon with a tunable wavelength near 281 nm. The second photon is a VUV photon of fixed wavelength at 118 nm, the 9th harmonic of a Nd:YAG laser. The UV wavelength was varied while measuring the ionization signal. The spectroscopic peaks were assigned to transitions between different rotational levels of the ground and excited states. For our experiment, we are only concerned with detection of OH in the J=3/2, ϵ=-1 state. The peak ionization signal from this state was detected at a wavelength corresponding to the R_{21} rotational branch.

Figure 4.3 shows the experimental setup for our OH detection. Light at 281 nm is produced using a pulsed dye laser (R6G), with the fundamental being frequency doubled by a KDP crystal. Light at 118 nm is produced by creating the 9th harmonic from an Nd:YAG laser. The YAG laser is internally frequency tripled to 355nm, then the 355nm light is tripled in a gas cell of Xenon and Argon. The process of producing this 118nm light is detailed later in this chapter. The ions are accelerated through a time of flight mass spectrometer (TOFMS) and detected by a microchannel plate (MCP). Ions are extracted from the ionization region to the MCP with near unit transfer efficiency. A grid on the front of the MCP needed for the final acceleration of the ions into the MCP plates reduces the detection efficiency to 90%. Since the detection efficiency is so much higher than for LIF, instead of trying to detect the entire cloud, we can reduce our detection volume by focusing the ionization beam. This will allow us to gain information about the position profile of the molecules in the trap. This information can elucidate dynamics of the molecules in the trap [60] and is important for understanding the results of trapped collision experiments [25, 61]

The 118nm light is focused through the trap with a beam waist of 30 μm. The last mirror

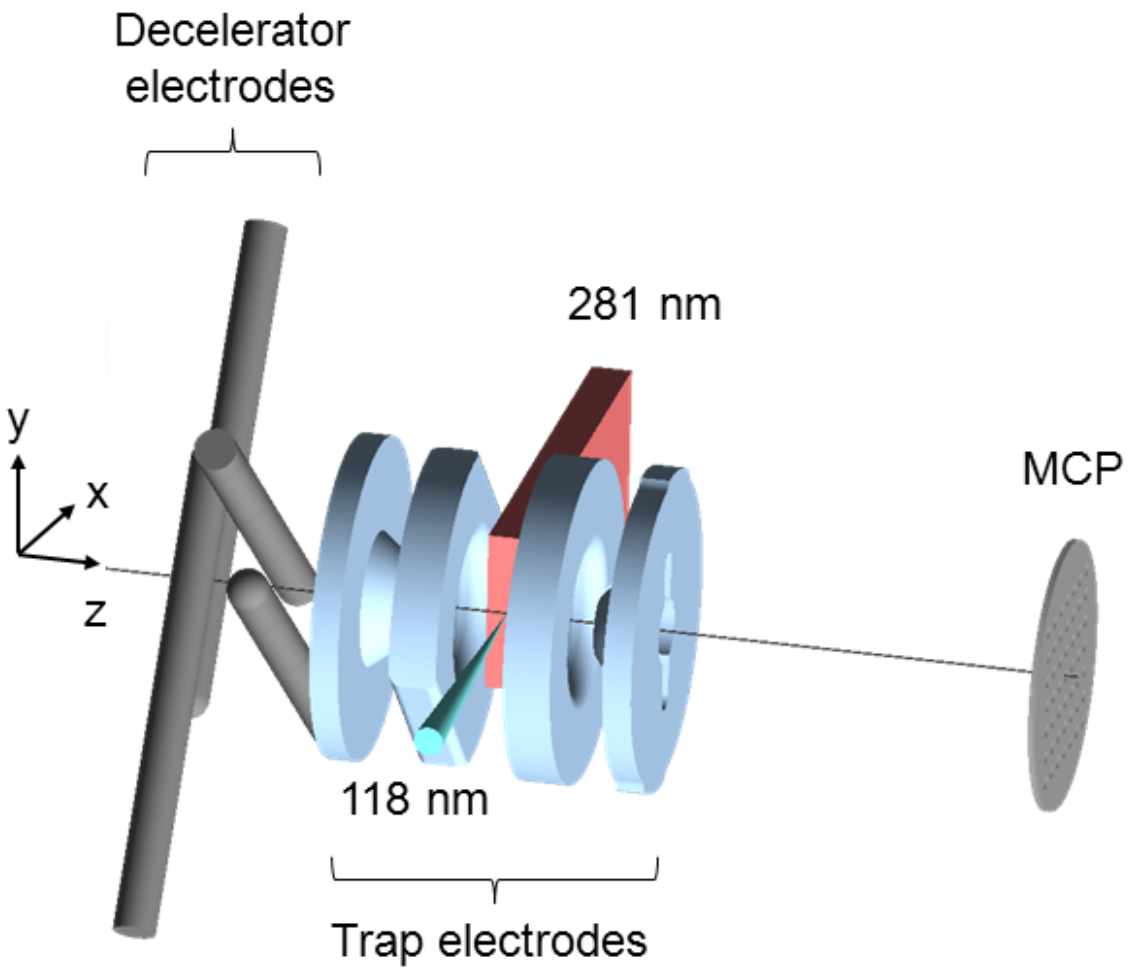

Figure 4.3: Experimental set up for REMPI detection of OH.

before the 355nm light enters the gas cell contains a computer-controlled closed-loop picomotor (New Focus Model 8310). The motor is used to scan the ionization position across the OH in the trap to measure the density as a function of position along the y-axis. The 281 nm light is cylindrically focused through the trap, with the focused direction being along the molecular beam axis. This produces a high intensity to saturate the excitation step, while also keeping the beam spread out along the y-axis in order to make sure the molecules are still being excited when the 118 nm light is scanned along that dimension. The two laser pulses are temporally separated by 20 ns, with the 281 nm light arriving first.

4.5 Future Improvements

It is possible that more OH ionization signal could be achieved by tuning the wavelength of the VUV. In [59], the authors resonantly excite OH to different rotational levels of the of the $A^2\Sigma^+(\nu = 1)$ state then measure the ionized OH signal while varying the VUV wavelength. This produces a rotationally resolved spectrum of transitions to the auto-ionizing Rydberg state. Figure 4.4 shows ionization from the $J = 5/2$ level of the excited state vs VUV wavelength, with the dashed purple line corresponding to the wavelength of the 9th harmonic of a YAG laser (discussed later in this chapter, this is how our VUV is produced). The strong ionization signal originating from the $J = 5/2$ state seems to be due to a coincidence of this 9th harmonic with one of the rotational levels of the Rydberg state. This wavelength sits on the side of the peak assigned to the ${}^PQ$ branch. Moving to the peak of this branch, or to the peak assigned to the R_2 branch could yeild more ionization signal in our experiment.

It also possible that varying the UV light to a different wavelength corresponding to excitation to a different rotational level in $A^2\Sigma^+(\nu = 1)$. There are 3 allowed transitions from our trapped OH state: R_{21}, Q_1, and P_{21}. Ionization signal after excitation along the Q_1 branch can be found in the middle plot of Figure 2 in [59] (reproduced here in Figure 4.5) while corresponding plot for the P_{21} branch is in Figure 1 of [59]. The OH ionization signals are all reported as relative signal and may not be directly comparable. However, the signal to noise ratio for the Q_1 branch plot appears

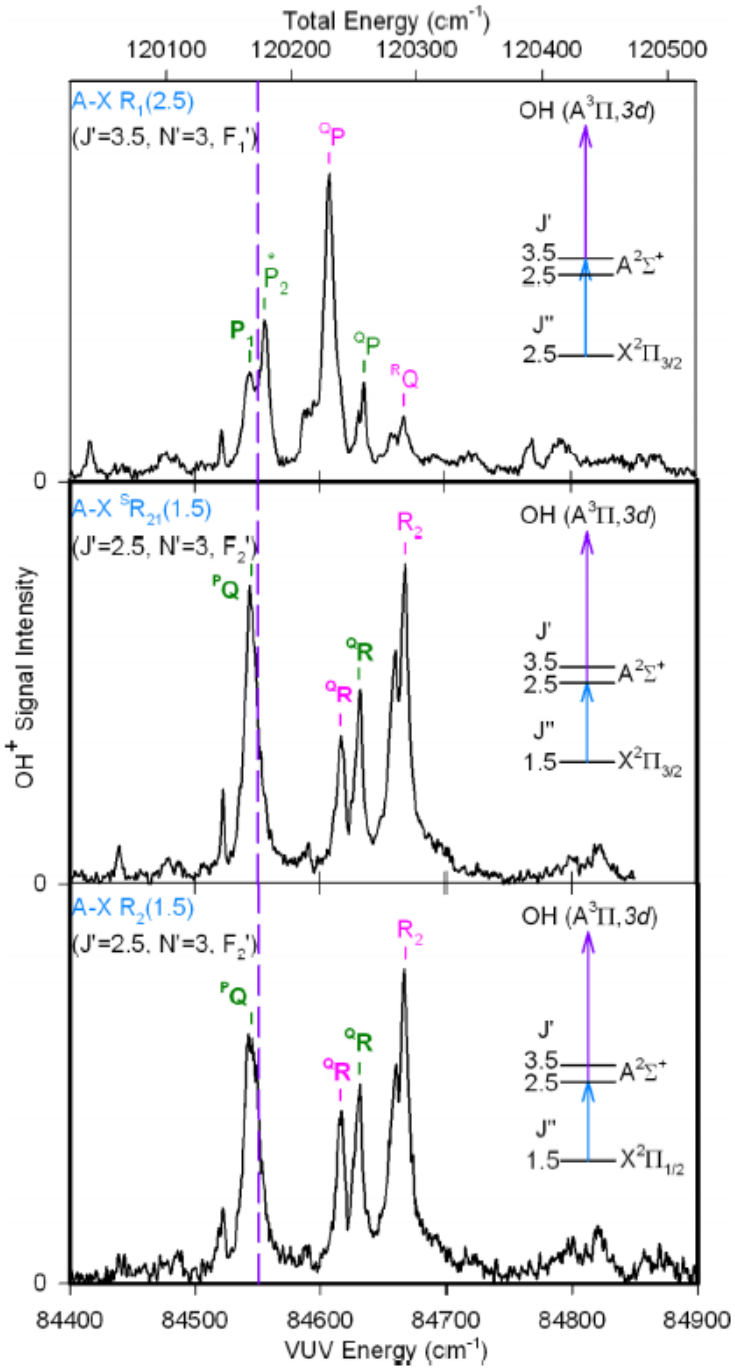

Figure 4.4: VUV Ionization spectrum of OH, From [59]. The vertical dashed line cooresponds to the fixed 118 nm light from the 9th harmonic of a Nd:YAG. The middle plot shows the ionization spectrum from the excited rotational state used in this work.

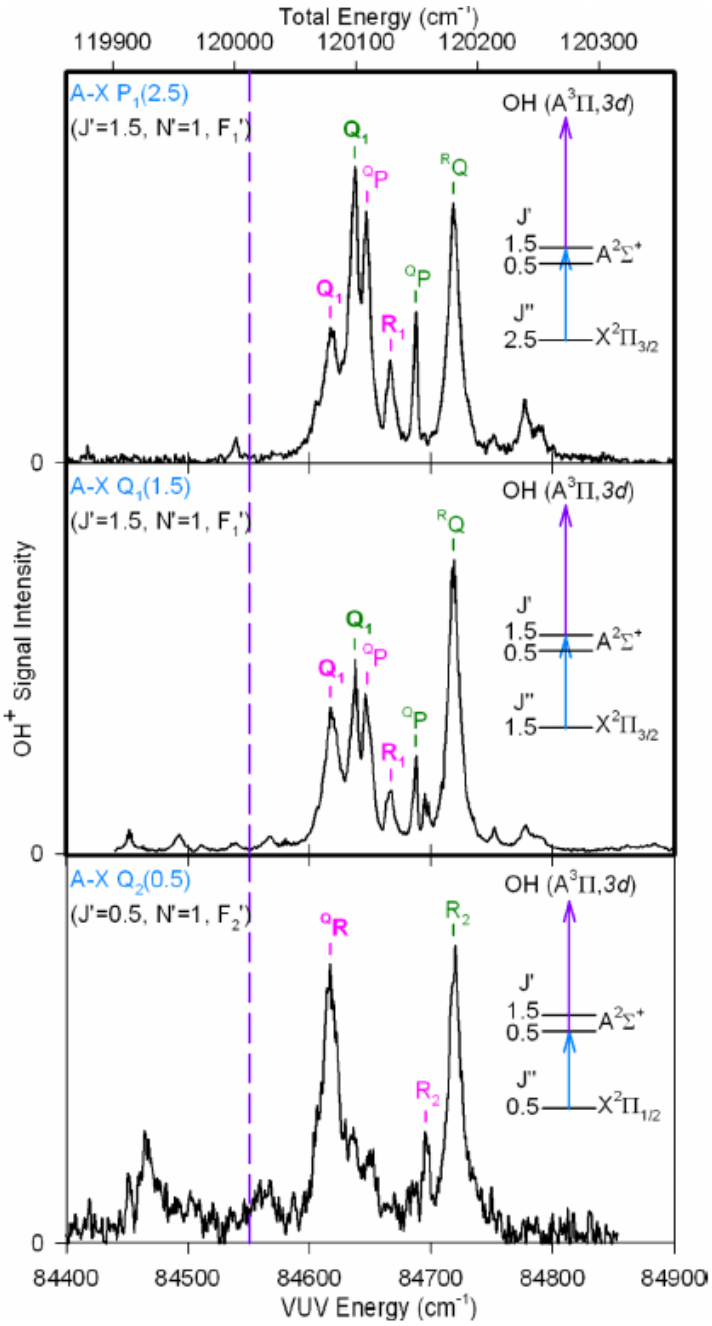

Figure 4.5: VUV Ionization spectrum of OH, From [59]. The vertical dashed line cooresponds to the fixed 118 nm light from the 9th harmonic of a Nd:YAG. The middle plot shows the ionization spectrum from the J'=1.5 state, which is accessible from the J"=1.5 state along the Q_1 rotational branch.

to be nearly an order of magnitude better than the other two branches. The enhanced ionization signal is likely due to a the Q_1 branch being the most efficient branch in terms of excitation. This may indicate that tuning the UV light to the Q_1 branch and the VUV to the peak of the ${}^{R}Q$ branch would yield even the most efficient ionization of decelerated and trapped OH.

Chapter 5

Produciton of 118 nm light

In this chapter, we present a reproduction of our paper "Characterization of a vacuum ultraviolet light source at 118 nm" by Gray et al. published in JCP in 2021 [62] The abstract and acknowledgements have been removed, and the bibliographical references and formatting have been changed to match the format of this thesis.

5.1 Introduction

Vacuum ultraviolet (VUV: $\lambda \approx$ 100-200 nm) light sources [63, 64, 65] have important applications in a wide variety of experiments in atomic physics and physical chemistry, including molecular spectroscopy for the understanding of chemical bonds, [66, 67] high resolution studies for metrology, [68, 69, 70, 71, 72] and as a universal ionization source in mass spectrometry[73, 74]. High fluxes of VUV light are available from synchrotrons, but the complexity, cost, and beam-time constraints of these sources makes a more accessible tabletop VUV source desirable. With the exception of excimer lasers,[75] which operate at only a few set wavelengths, tabletop sources of VUV light require use of nonlinear optical techniques. Nonlinear optical frequency mixing, [76, 77, 78] of which harmonic generation is a special case, is a powerful technique for producing coherent radiation at wavelengths where small commercial laser sources do not typically operate.[79]

One VUV source is made by frequency tripling the third harmonic output of a Nd:YAG laser in a xenon-argon gas mixture to create 118 nm light. The 118 nm photon can be used in single or multi-photon ionization applications. Specifically, chemical dynamics studies use 118 nm

light in ion-pair photodissociation spectroscopy,[80] ion pair production,[81] anion photoelectron spectroscopy,[82] and one-photon ionization processes. [83, 84, 85, 86] Additionally, 118 nm photons have been used to perform multi-photon ionization of cold radical molecules.[87, 88, 60]

Since the conversion efficiency of 355 nm light to 118 nm light is low ($\sim 10^{-5}$)[89] and may constrain the detection sensitivity of an experiment, it is important to understand the limits of the tripling technique in order to experimentally optimize 118 nm light production. The basic theory of 118 nm generation in a xenon-argon gas cell [90, 91, 92] and experimental setup[93] have been detailed in previous papers. However, the experimentally observed 118 nm photon production has been observed to significantly diverge from theory at high gas pressures and has not been modeled so far.

Here, we describe the basic theory and experimental setup for generating 118 nm light and characterize the limitation of the VUV production at high xenon pressures. We present evidence that absorption at 118 nm by xenon limits 118 nm production. We develop a model that accounts for this absorption, whose predictions are in good agreement with our experimental results.

5.2 Theory of Non-Resonant Third Harmonic Generation

Anisotropic crystals with large second-order nonlinear optical susceptibilities ($\chi^{(2)}$) and a wide optical transparency range can be efficient at producing visible, near-infrared, and soft UV light. Since these crystals start to absorb light below 200 nm, generation of VUV light via nonlinear optical frequency mixing generally requires a gaseous nonlinear medium, which is transparent at these wavelengths. However, the structural symmetry of isotropic media such as gases means that only odd-order nonlinear susceptibilities are non-vanishing,[94] leaving the third-order susceptibility, $\chi^{(3)}$, as the first nonlinear term. [76]

Third-harmonic light produced by the large $\chi^{(3)}$ in these systems can extend into the VUV and extreme ultraviolet regions of the spectrum. For this process to be efficient, phase matching is important, as the fundamental light and third-harmonic light must maintain a fixed phase relationship in order to coherently build the tripled light. In the gaseous system discussed here, phase

matching is accomplished by mixing a negatively dispersive gas that acts as the nonlinear medium with positively dispersive gas that can be used to tune the phase matching. In the remainder of this section, we discuss the basic model of third-harmonic generation (THG) and conditions to optimize phase matching.

The basic setup for THG is depicted in Fig. 5.1. The fundamental light at 355 nm is focused into a gas cell of length, L, with a beam waist of w_0 and a confocal parameter of $b = \frac{2\pi w_0^2}{\lambda}$. The third-harmonic light is shown in blue. The total power of the third-harmonic light produced by a focused Gaussian beam with incident fundamental power $\mathcal{P}_\omega$ is given by [91, 92]

$$\mathcal{P}_{3\omega} = \frac{8.215 \times 10^{-2}}{(3\lambda)^4} \left|\chi_{eff}^{(3)}\right|^2 \mathcal{P}_\omega^3 \left|F_1(b\Delta k)\right|^2 . \tag{5.1}$$

Here, all powers are in watts, λ is the third-harmonic wavelength in nm, and $\chi_{eff}^{(3)}$ is the macroscopic nonlinear coefficient. $F_1(b\Delta k)$ is a dimensionless function that describes phase matching, and Δk is the wave-vector mismatch between the fundamental and third-harmonic light.

Experimentally, there are four parameters that can be varied to optimize the third-harmonic power (Eq. 5.1): (1) the macroscopic nonlinear coefficient $\chi_{eff}^{(3)}$, (2) the confocoal parameter, and (3) maximizing the power in the fundamental ($\mathcal{P}_\omega$). However, independent maximization of Δk in a single component gas is impossible because both $\chi_{eff}^{(3)}$ and $F_1(b\Delta k)$ are dependent on $\mathcal{N}$, the atomic number density of the gas. $\chi_{eff}^{(3)}$ is given by

$$\chi_{eff}^{(3)} = \mathcal{N} \times \chi_a^{(3)}, \tag{5.2}$$

where $\mathcal{N}$ is in units of atoms/cm^3 and $\chi_a^{(3)}$ is the third-order nonlinear coefficient per atom in esu. Generally $F_1(b\Delta k)$ must be evaluated numerically. However, in the tight-focusing limit, where the nonlinear medium is much longer than the confocal parameter of the focused fundamental beam ($b \ll L$), $F_1(b\Delta k)$ can be solved analytically to give [92, 90]

$$|F_1(b\Delta k)|^2 = \begin{cases} \pi^2 (b\Delta k)^2 e^{b\Delta k} & \Delta k < 0, \\ 0 & \Delta k \geq 0, \end{cases} \tag{5.3}$$

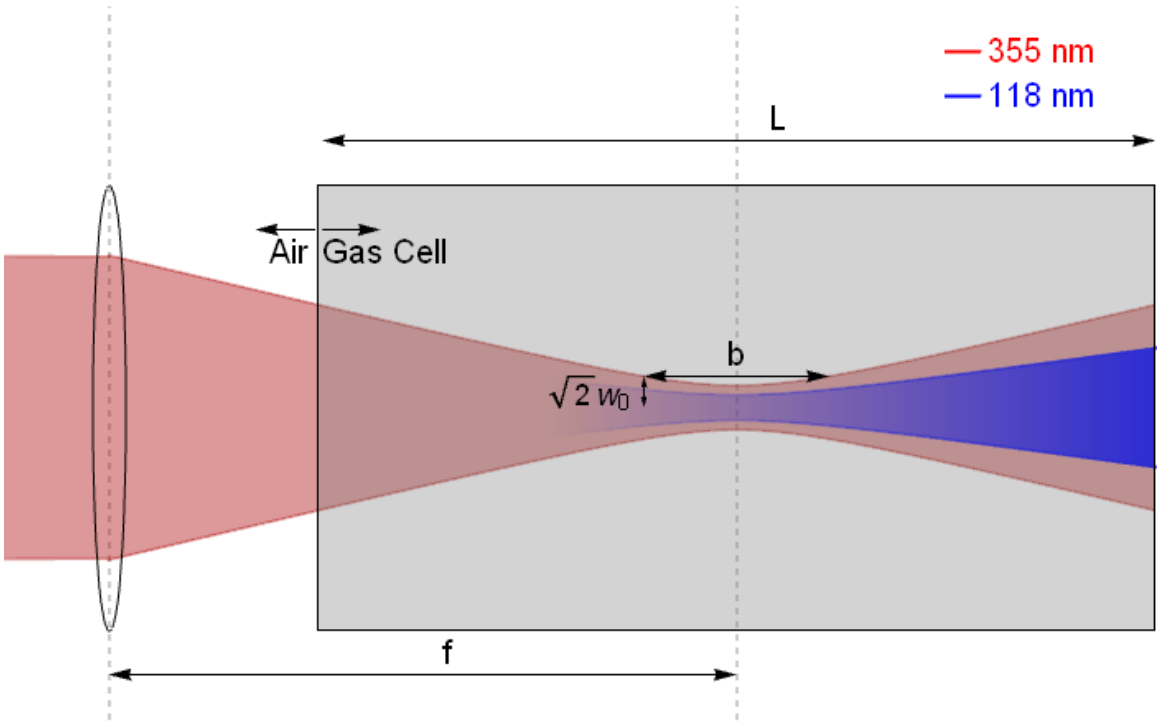

Figure 5.1: Diagram showing the parameters of the gas cell for generating 118 nm light (blue). The 355 nm beam (red) is focused into the gas cell (gray box) by a lens with focal length f. The confocal parameter b and beam waist w_0 are noted.

which has a maximum at $\Delta k_{max} = -\frac{2}{b}$.

Δk is related to $\mathcal{N}$ through the index of refraction, and is given by

$$\Delta k = \frac{2\pi}{\lambda}\left[n_1 - n_3\right]. \tag{5.4}$$

In this notation, n_1 and n_3 are the index of refraction at the third-harmonic wavelength λ and the fundamental wavelength 3λ, respectively. For a gas, the effective macroscopic index of refraction, n, is given by

$$n(\lambda) = 1 + \mathcal{N}\chi_a^{(1)}(\lambda), \tag{5.5}$$

where $\chi_a^{(1)}$ is the atomic linear susceptibility at wavelength λ. Therefore, Δk can be expressed as

$$\Delta k = C\mathcal{N}, \tag{5.6}$$

where $C = \frac{2\pi}{\lambda}\left[\chi_a^{(1)}(\lambda) - \chi_a^{(1)}(3\lambda)\right]$ is a constant describing the microscopic dispersive properties of the gaseous medium. C can be thought of as the effective wave-vector mismatch per atom. Phase matching is adjusted by tuning Δk, and thus $F_1(b\Delta k)$, via the pressure of the gas.

As can be seen from Eqn. 5.3, Δk must be negative to generate third-harmonic light. This occurs only in media that exhibits negative dispersion (i.e., $n_3 > n_1$). Xenon was chosen as the nonlinear medium for THG of 118 nm because it is the only rare gas that exhibits negative dispersion at this wavelength. With only a negatively dispersive gas, Δk and $\chi_{eff}^{(3)}$ are both dependent on $\mathcal{N}$. If a positively dispersive gas with negligible nonlinearity is added, Δk and $\chi_{eff}^{(3)}$ can be decoupled. Argon is typically used as the positively dispersive gas for THG of 118 nm light.[93] For a mixture of the two gases, the total wave-vector mismatch at the nominal third-harmonic wavelength, λ_0, is given by summing over the partial pressures of each gas,

$$\begin{aligned}\Delta k(\lambda_0) &= \mathcal{N}_{Xe}C_{Xe}(\lambda_0) + \mathcal{N}_{Ar}C_{Ar}(\lambda_0), \\ &= \mathcal{N}_{Xe}\left[C_{Xe}(\lambda_0) + RC_{Ar}(\lambda_0)\right],\end{aligned} \tag{5.7}$$

where $R = \frac{\mathcal{N}_{Ar}}{\mathcal{N}_{Xe}}$ is the pressure ratio of the two gases. With the addition of argon, $\chi^{(3)}_{eff}$ can be adjusted using $\mathcal{N}_{Xe}$, while Δk can be maximized using $\mathcal{N}_{Ar}$.

Since $F_1(b\Delta k)$ is maximized when $\Delta k(\lambda_0)_{max} = -\frac{2}{b}$, phase matching is optimized when the pressure ratio is

$$R_{\text{opt}} = \frac{-2}{b}\frac{1}{\mathcal{N}_{Xe}C_{Ar}(\lambda_0)} - \frac{C_{Xe}(\lambda_0)}{C_{Ar}(\lambda_0)}. \tag{5.8}$$

For large xenon pressures, which are desirable for increasing $\chi^{(3)}_{\text{eff}}$ and thus $\mathcal{P}_{3\omega}$, the optimum ratio approaches the constant value of $\frac{C_{Xe}}{C_{Ar}}$ and is independent of the value of confocal parameter, b. Using the values $C_{Xe}(118.2\text{ nm}) = -6.12\times10^{-17}\text{cm}^2$ and $C_{Ar}(118.2\text{ nm}) = +5.33\times10^{-18}\text{cm}^2$ from Mahon *et al.,* [95] this ratio is 11.48.

5.3 Experimental Setup for Third-Harmonic Generation

The experimental apparatus used to generate VUV light is shown in Fig. 5.2. Light at 355 nm from a Q-switched Nd:YAG laser (Continuum: Inlite III-10, internally tripled) is focused into a mixture of xenon and argon contained in a stainless steel cell using a 50 cm focal length lens. The gas cell is made of standard 304-SS conflat vacuum parts with an overall length of $\sim$ 40 cm. A UV fused silica window seals the input end of the cell, where the 355 nm light enters. The output end, between the gas cell and the UHV detection chamber, is sealed using a 25 cm focal length MgF_2 lens, which also serves to focus the VUV light into the detection region.

The focal length of the lens and size of the cell must be chosen to avoid burning optics and maximize gas conductance. The cell is three standard conflat crosses connected together and has a length of $\sim$ 40 cm. The focal length of the 50 cm lens, external to the cell, was chosen to be approximately the length of the gas cell. The focus is designed to be in the center of the gas cell, so that the 355 nm intensity at the input window and output lens are low enough to prevent damaging the optics. The position of the focus also allows for perpendicular optical access through a conflat window into the focal region. Although LiF windows have a higher transmission at 118 nm, a

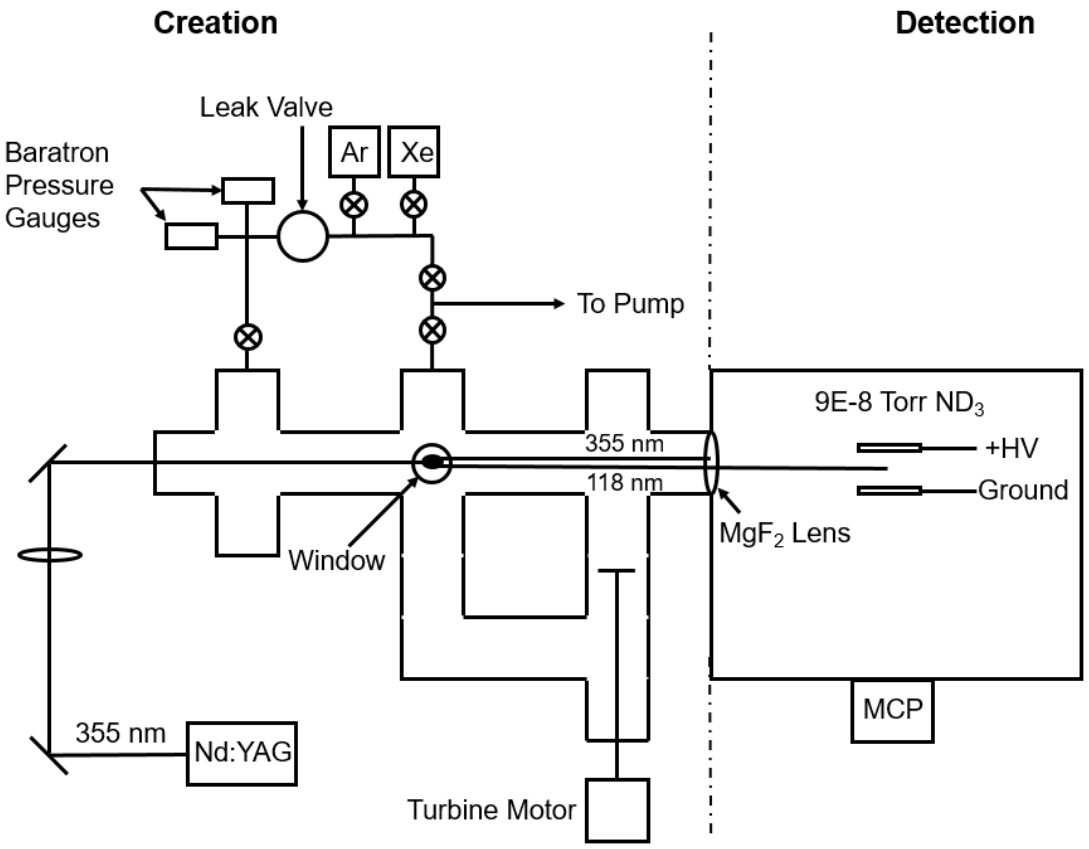

Figure 5.2: Schematic of the experimental setup. A lens focuses the 355 nm light into the gas cell where 118 nm light is created. A window placed above the focus of the 355 nm beam allows perpendicular optical access to the tripling region. The MgF_2 lens focuses the 118 nm light and defocuses the 355 nm in the detection region. 118 nm flux is detected via ionization of deuterated ammonia (ND_3). A low flow rate of ND_3 fills the detection chamber to a partial pressure of 9×10^{-8} Torr. ND_3^+ ions are accelerated through a time-of-flight mass spectrometer and detected by a micro-channel plate (MCP).

MgF_2 window was chosen for the output lens due to its hardness and because it is not hygroscopic, allowing the window to handle pressure differentials in excess of 1 atm. The large positive dispersion in MgF_2 causes the focal length of the lens at 118 nm to be about 58% shorter than that at 355 nm. This property is exploited to minimize the intensity of 355 nm in the detection region by defocusing the 355 nm light, which helps to prevent multi-photon processes. Additionally, most of the defocused 355 nm light is blocked from even reaching the detection region by a macor iris placed after the MgF_2 lens.

The gas cell is constructed from 2-3/4 inch conflat pieces to provide adequate gas conductance. Attempts at making portions of the gas cell out of 1/4 inch ID tubing led to trapped pockets of unmixed xenon, which slowly diffused out over several days. The release of trapped xenon led to drifts in the gas ratio, changing the phase matching and leading to drifts in the amount of 118 nm light produced.

Xenon and argon are introduced into the gas cell through a leak valve and needle valve. The needle valve is important for separating the gas mixing cell from the low conductance elements such as the pressure gauges and gas lines connecting the leak valve. Leaving open the needle valve between the gas mixing cell and leak valve increases the gas mixing time by a factor of three.

Gas mixing in the cell can be aided by a turbine, which causes gas to flow in a loop of 2-3/4 inch conflat pieces (Fig. 5.2). Gas mixing using the turbine did not reach equilibrium noticeably faster than without the turbine, but the 118 nm flux varied more smoothly while mixing. Without the turbine, adding argon to the system would cause large spikes and dips in the measured 118 flux, as the introduction of argon rapidly changed the Xe/Ar ratio in the tripling region. Unaided mixing in the cell took only 15 minutes with no signs of continued mixing or signal loss observed over the course of several weeks.

The 118 nm light is detected indirectly by using it to ionize deuterated ammonia (ND_3) and subsequently detecting ND_3^+. 118 nm light is focused by the MgF_2 lens between two electrodes in the UHV chamber. Ionized ND_3 is accelerated through a time-of-flight mass spectrometer (TOF-MS) and is detected by a micro-channel plate (MCP) (Fig. 5.2). The number of ND_3^+ ions produced

is proportional to the number of 118 nm photons that are focused into the detection region, since the ionization is a one-photon process and no saturation effects are observed.

5.4 Phase Matching and Conversion Efficiency Limitations

To experimentally determine the phase matched ratio of partial pressures of Xe/Ar, we add a set amount of xenon to the mixing cell and then add increments of argon in order to map out each phase-matching curve. Fig. 5.3 shows phase-matching curves for several xenon pressures. Each phase-matching curve was fit to Eq. 5.3 to extract the location of the peak 118 nm flux and the optimum Xe/Ar ratio for a given xenon pressure. The optimum Xe/Ar ratios are plotted in Fig. 5.4 along with a fit to Eq. 5.8, which gives $b = 2.3 \pm 0.3$ cm. As shown in Eq. 5.8, the optimum Xe/Ar ratio depends on the confocal parameter and xenon pressure, but for high xenon pressures the ratio approaches the asymptotic limit of 11.48 (horizontal dashed line).

Although the optimum pressure ratios are consistent with the model, the conversion efficiency of 355 nm light to 118 nm does not agree with model predictions. Eq. 5.1 predicts that for a phase-matched mixture, the 118 nm light produced should scale as the square of the xenon pressure. However, mixtures with more than 24 Torr of xenon (290 Torr total pressure) yielded decreasing 118 nm light with increasing Xe pressure. At xenon pressures >70 Torr, almost no 118 nm light was detected. This same turnover in 118 nm light production versus total pressure has been observed in Shi *et al.*. [85] In other studies, optimal conversion efficiencies have been observed at lower total pressures of 20 Torr,[84] 50 Torr,[82] and 200 Torr. [86] The prevalence of optimal conversion efficiencies at low total pressures and the large discrepancy between the predicted and measured yield of 118 nm light at high pressures indicates that some process, which is not included in the models, is significantly limiting the production of 118 nm light.

The deviation from theory for the expected 118 nm flux of a phase-matched mixture of Xe/Ar at higher total pressures is accompanied by the appearance of a fluorescence streak inside the gas cell (inset Fig. 5.5). It appears near the focus of the 355 nm light and along the propagation axis. The fluorescence streak does not appear when 355 nm light is focused in to the cell filled with only

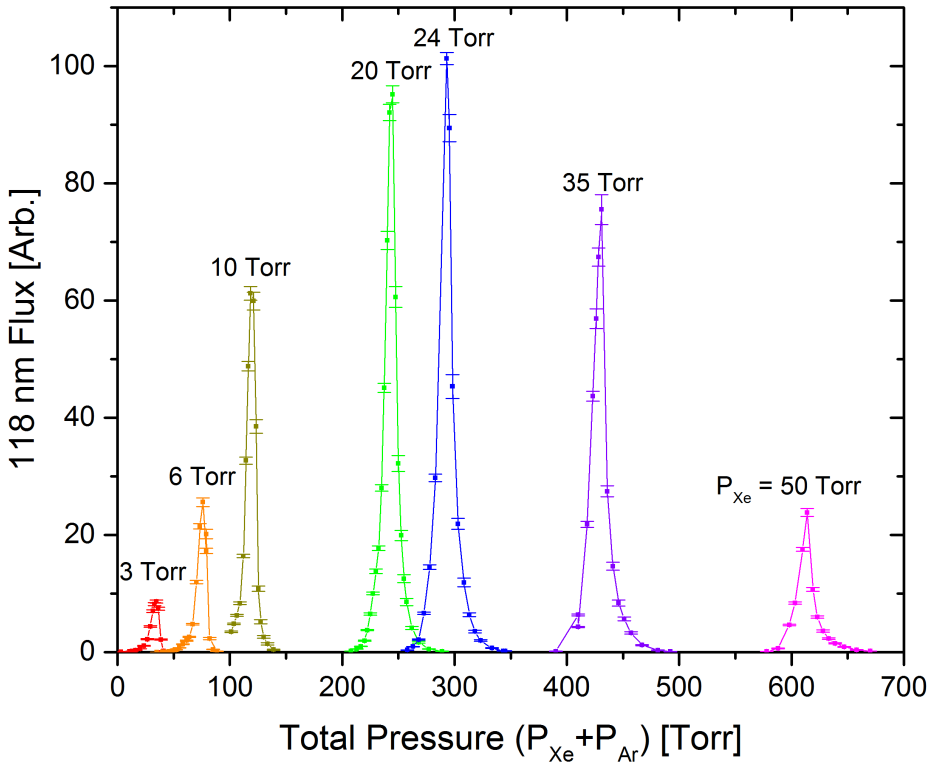

Figure 5.3: Phase-matching curves for different pressures of xenon (labeled above). 118nm flux is measured while Ar is added to a fixed pressure of Xe and plotted as a function of total pressure.

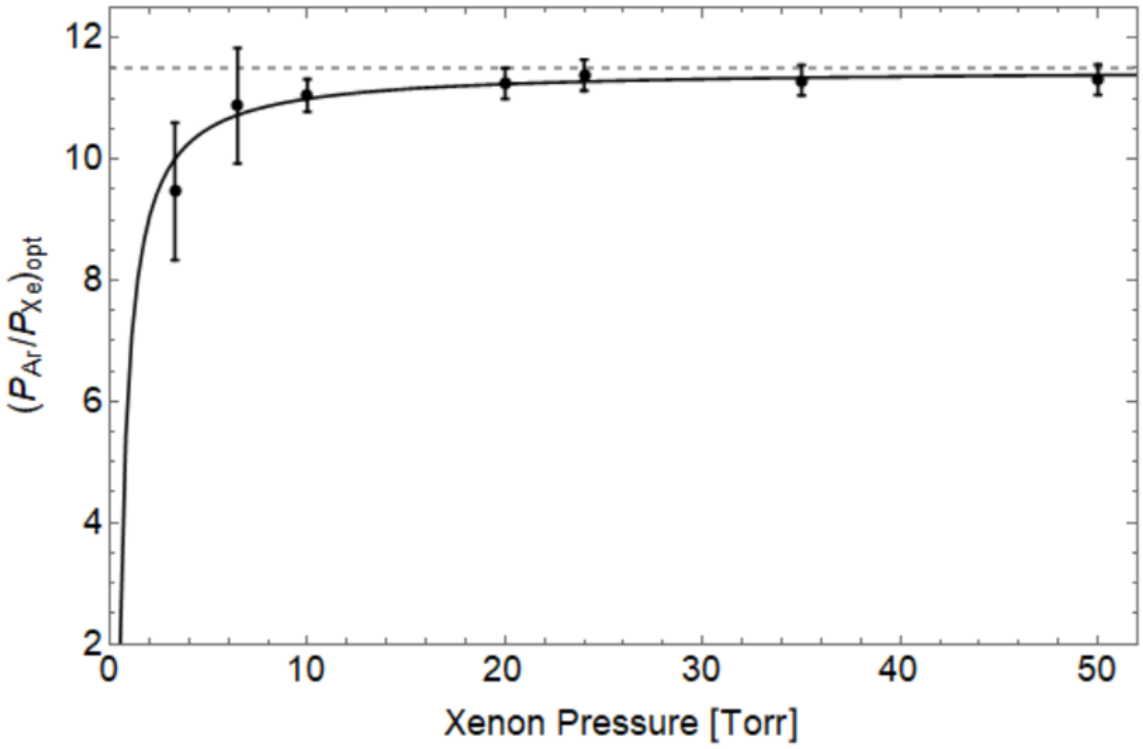

Figure 5.4: Plot of optimum Ar:Xe ratio vs. Xe pressure. The solid line is the output of a fit of Eq. 5.8 to the data with b = 2.3 ± 0.3 cm as the only fit parameter. The dashed line represents the asymptotic limit of 11.48 predicted from the model.

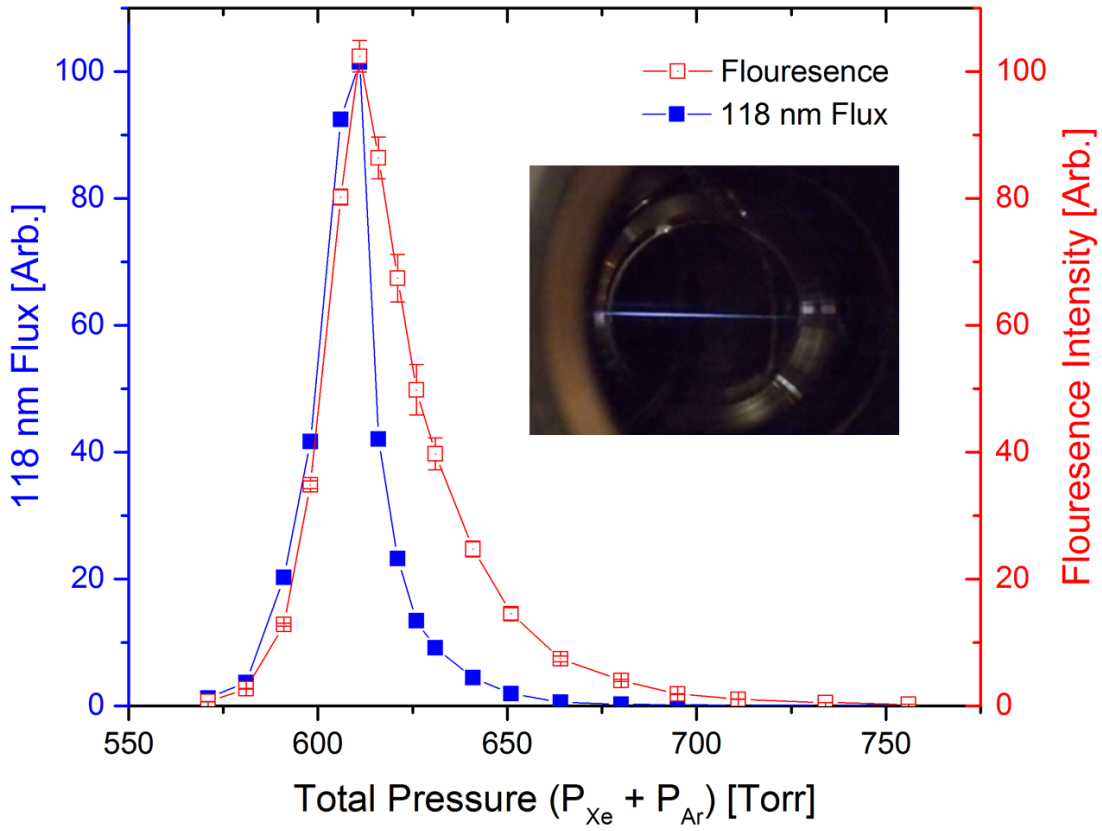

Figure 5.5: Plot of 118 nm flux and the fluorescence signal vs total pressure for $P_{Xe} = 50$ Torr. The fluorescence signal is correlated with the presence of 118 nm light. The inset show a picture of the fluorescence streak through a conflat window.

argon or only xenon. Instead it appears only when xenon and argon are both present and near a phase-matched ratio. The fluorescence is collected through a vaccuum window using a lens outside the gas cell to focus the light onto a photodiode. The fluorescence intensity follows the shape of the generated VUV light flux throughout a phase-matching curve as shown in Fig. 5.5, indicating that 118 nm photons play a role in the fluorescence. Fig. 5.6 shows the 118 nm flux and fluorescence signal as a function of the xenon pressure for a phase-matched mixture. The fluorescence appears to begin at some threshold xenon pressure and increases roughly linearly in intensity with increasing xenon pressure.

118 nm light was also created using krypton as the phase-matching gas. Using the same apparatus and measurements described above, xenon and krypton were phase matched with an optimum Kr/Xe ratio of 4.6, which agreed with the krypton dispersion calculated in Mahon *et al.* [95] This mixture also produced a maximum of 118 nm light followed by a decrease with increasing gas pressure. The fluorescence streak was also present only with a phase-matched mixture of the two gasses. (Fig. 5.6). Spectra of the fluorescence were obtained for the Xe/Ar (Fig.5.7 (a)) and Xe/Kr (Fig.5.7 (b)) systems using an Ocean Optics USB2000 spectrometer. Spectral lines were assigned using data from the NIST Atomic Spectra Database. [96] We mark the location of all lines in the NIST database that are above a certain threshold relative intensity [96] in order to identify observed lines and note which lines are missing from the spectra. For Xe and Kr, a threshold of 500 was used, and for Ar a threshold of 20000 relative intensity was used. The Xe/Ar spectrum (Fig. 5.7 (a)) shows predominantly Xe I spectral lines and weak Ar I spectral lines. The lines are similar in relative signal to those observed from a xenon arc lamp, indicating that the fluorescence is likely from electron-ion recombination in xenon. The spectrum for the Xe/Kr system (Fig.5.7 (b)) also shows predominantly Xe I spectral lines, with Kr I spectral lines appearing relatively weakly. Xenon is ionized preferentially despite being present in a lower concentration than the phase-matching gasses (Ar or Kr). This would seem to indicate that ionization is not due to just the high electric field of the 355 nm light, but a resonant process involving xenon. The energetics suggest a two-photon process is causing the ionization of xenon. The energy of a single 118 nm

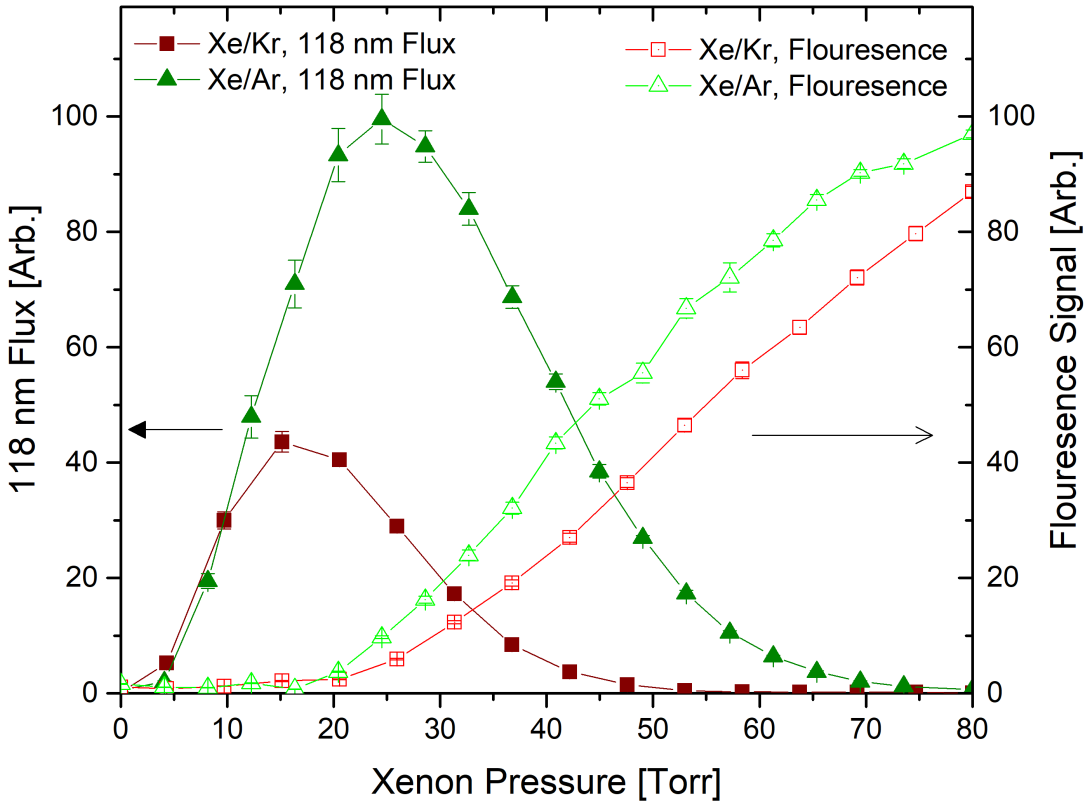

Figure 5.6: Comparison of the 118 nm signal and fluorescence streak signal at different xenon pressures for a phase-matched mixture with Ar (Ar:Xe Ratio = 11.3) and Kr (Kr:Xe Ratio = 4.6).

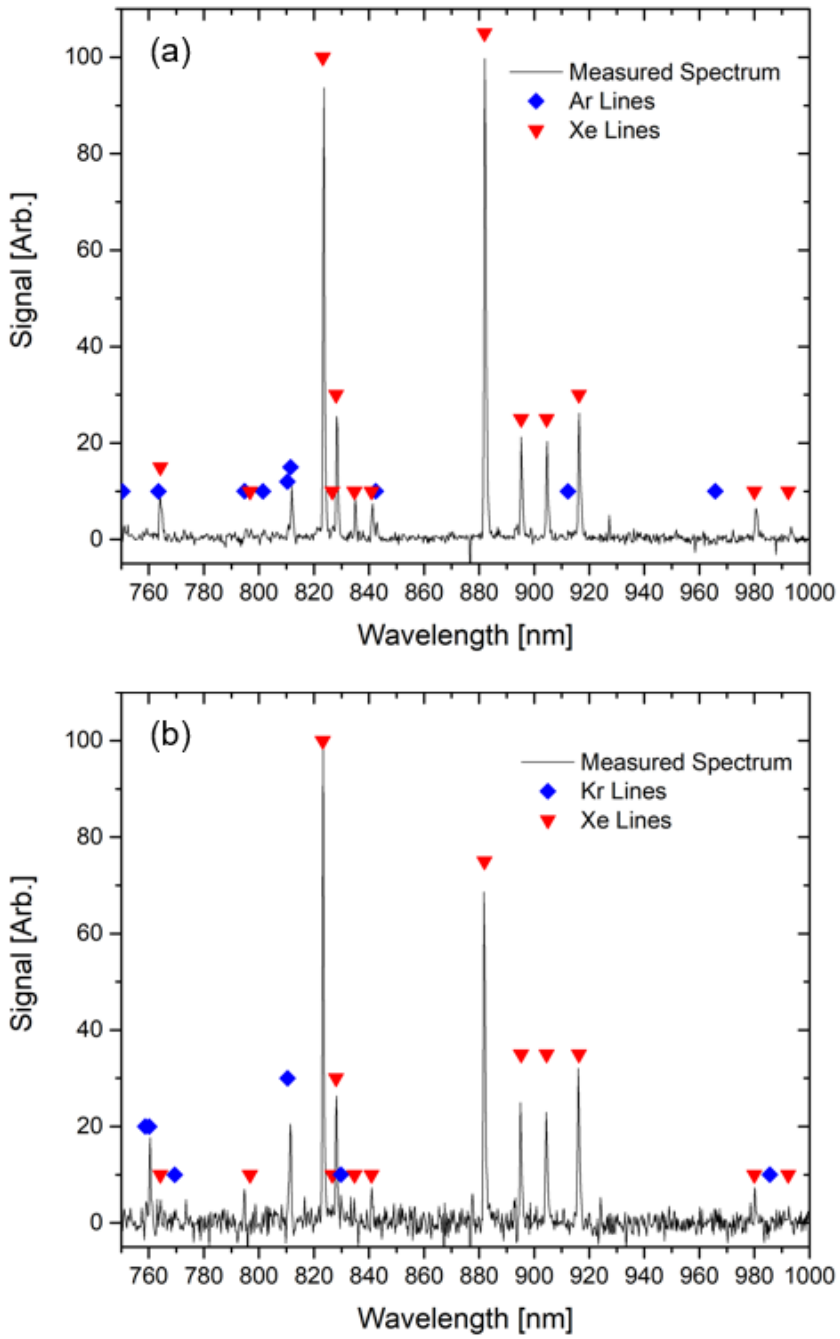

Figure 5.7: Spectra of the fluorescence streak created in a phase-matched (a) Xe:Ar mixture (Ar:Xe Ratio = 11.3) and (b) Xe:Kr mixture (Kr:Xe Ratio = 4.6). Lines corresponding to Ar I, Kr I, and Xe I are assigned according to criteria described in the text.

photon (10.5eV) is below the ionization potential of xenon (12.1 eV). However, the combined energy of one 118 nm photon and one 355 nm photon (14 eV) is enough to ionize xenon, while being below the ionization potential of argon (15.8 eV). The ionization potential of krypton (14 eV) is low enough to possibly be ionized in this system, however strong ionization of kryton is not evident. Two-photon ionization of xenon, where one of the photons is 118 nm and the other is a 355 nm photon, is likely the mechanism producing xenon ions. The intensity of the 355 nm light is much larger than that of the third harmonic, so we can assume the absorption of the 118 nm light is the rate limiting step. We model this process as two-photon, two-color ionization model where the absorption of the 118 nm photon is far from resonance and is affected by the pressure in the gas cell due to pressure broadening. This pressure broadened absorption is the proposed mechanism for loss of 118 nm light in the detection region for high cell pressures. In Xenon the two lines closest to resonance with the 118 nm light are the Xe $(^2P_{3/2})$5d $\left[\frac{3}{2}\right]$ line at 119.2 nm and the Xe $(^2P_{3/2})$7s line at 117 nm. We also must consider the Kr $(^2P_{1/2})$5d $\left[\frac{1}{2}\right]$ resonance line at 116.5 nm, which can lead to additional absorption in the case of phase matching with Kr. Argon does not have any transitions near enough to 118 nm to cause significant loss.

5.5 Absorption Cross Section

We consider far off-resonance absorption in the presences of pressure broadening. The atomic absorption cross section for light at frequency ω due to an absorption line at ω_0 is given by

$$\sigma(\omega) = \frac{fe^2}{m\epsilon_0 c\gamma} \frac{(\gamma/2)^2}{(\omega-\omega_0)^2 + (\gamma/2)^2}, \tag{5.9}$$

where f is the oscillator strength, e is the electron charge, m is the mass of the electron, ϵ_0 is the permittivity of free space, c is the speed of light, and γ is the linewidth. Far from resonance, $(\omega-\omega_0)^2 >> (\gamma/2)^2$, and Eqn. (5.9) can be approximated as

$$\sigma(\omega) = \frac{fe^2}{4m\epsilon_0 c} \frac{\gamma}{(\omega-\omega_0)^2}, \tag{5.10}$$

noting that the cross section is proportional to the linewidth. For gasses at high pressures, collisions

between atoms contribute to the Lorentzian linewidth of an absorption in a process known as pressure broadening. Neutral atoms undergoing collisions induce a dipole that perturbs the energy levels and broadens the linewidth of transitions. Collisions between atoms of the same species experience resonant collisions that enhance this broadening. Same-species broadening is typically $\sim$ 1 GHz$\times 2\pi$ per Torr of gas vs. $\sim$ 10 MHz$\times 2\pi$ per Torr of gas for collisions between different species.[97, 98] In our two-species gas, although the phase matching gas is present in much higher quantities than xenon, resonant Xe-Xe collisional broadening will dominate the pressure broadening. The pressure broadened linewidth is given by

$$\gamma = \gamma_n + \gamma_c, \tag{5.11}$$

where γ_n is the natural linewidth and γ_c is the collisional linewidth, which is proportional to the density, $\gamma_c = \beta\mathcal{N}$, where β is the collisional broadening coefficient and $\mathcal{N}$ is the density of the gas. For the lines considered in this paper $\gamma_n \sim 100$ MHz$\times 2\pi$, while $\gamma_c \sim 1$ GHz$\times 2\pi$ per Torr of gas.[99] So, for pressures used in this experiment $\gamma_n << \gamma_c$, and γ_n can be ignored such that $\gamma \cong \gamma_c$. This allows us to write our pressure broadened cross section as

$$\begin{aligned} \sigma(\omega) &= \frac{fe^2}{4m\epsilon_0 c}\frac{\beta\mathcal{N}}{(\omega-\omega_0)^2}, \\ &= \alpha\mathcal{N}, \end{aligned} \tag{5.12}$$

where α is defined as our pressure broadening constant.

5.6 Simulation Results

In order to compare our pressure broadened absorption model to the experimental data, we simulate the simultaneous tripling and absorption processes in our gas system. The electric field of an electromagnetic wave with frequency, ω, and wavenumber, k, propagating along the z-axis is given by

$$E(z,t) = Ae^{i(kz-\omega t)} + c.c., \tag{5.13}$$

where A is the electric field amplitude. The intensity of the electric field is related to the electric field amplitude by $I = 2n\epsilon_0 c|A|^2$. The change in the intensity of the 118 nm beam as it propagates through a medium can be simulated by calculating the change in the electric field amplitude. The differential equation describing the propagation of the 118 nm beam is given by

$$\frac{d|A_{118}|}{dz} = \frac{1}{2}\chi^{(3)}\mathcal{N}_{Xe}k_{118}|A_{355}|^3 - \frac{1}{2}\sigma\mathcal{N}_{Xe}|A_{118}|, \tag{5.14}$$

where $\chi^{(3)}$ is the third order susceptibility, $\mathcal{N}_{Xe}$ is the density of xenon, k_{118} is the wavenumber of the 118 nm light, A_{355} is the field amplitude of the 355 nm beam, σ is the absorption cross section, and A_{118} is the field amplitude of the 118 nm beam. The first term describes the third harmonic generation of 118 nm light assuming perfect phase matching and the second term describes the loss of 118 nm light due to absorption. Using Eqn (5.12), this becomes

$$\frac{d|A_{118}|}{dz} = \frac{1}{2}\chi^{(3)}\mathcal{N}_{Xe}k_{118}|A_{355}|^3 - \frac{1}{2}\alpha\mathcal{N}_{Xe}^2|A_{118}|. \tag{5.15}$$

The 355 nm power is kept constant, assuming the third harmonic generation leads to negligible loss. To account for the fact that the 355 nm beam is focusing through the gas cell, the electric field amplitude along the z axis is scaled by the radius of the beam

$$|A_{355}(z)| = |A_{355}(0)|\frac{\omega_0}{\omega(z)}, \tag{5.16}$$

where ω_0 is the beam waist, $\omega(z) = \omega_0\sqrt{1 + (\lambda z/\pi\omega_0^2)^2}$ is the beam radius as a function of z, and $A_{355}(0)$ is the field amplitude at the focus calculated from experimental parameters.

Although the 118 nm beam also has a transverse spread that changes through the focus, the 118 nm amplitude is not scaled by the beam radius. This assumes that the effects of the transverse spread are negligible on relative measurements across our parameter space. The majority of the third harmonic generation takes place within the Rayleigh range, where the beam radius varies from ω_0 to $\sqrt{2}\omega_0$. We assume this variation is negligible and the 118 nm light is created with roughly the same beam radius. Linear absorption does not affect the width of a Gaussian beam, thus the

transverse expansion of the beam is the same for all parameters, and ignoring the expansion does not effect relative measurements.

The differential equation is numerically integrated over the 40 cm length of the gas cell, with the focus at the center. The 118 nm field amplitude at the end is used to calculate a beam flux, since our experimental results are a measure of the flux of the 118 nm photons. Additionally, we assume that the amount of light from the fluorescence streak is proportional to the loss of 118 nm light in a region around the focus of the 355 nm beam that approximates our fluorescence collection region.

Using our simulations, we want to model the experiment shown in Fig (5.6), then compare the simulated and experimental results to extract a value for α. The two free parameters in this simulation are the pressure-broadening constant, α, and an overall vertical scaling of the magnitude of the signal. For a single value of α, the simulation is run for a range of xenon pressures to produce a curve of 118 nm flux vs pressure similar to Fig (5.6). The simulated curves are fit to the experimental data by calculating a sum of squared residuals between the experimental and simulated results for a given value of α and vertical scaling factor.

The fitted simulation results for the Xe/Ar case are shown in Fig 5.8. The model accurately reproduces the shape of the experimental 118 nm flux. A value of $\alpha_{Xe} = 0.84(1) \times 10^{-37} cm^5$ is extracted from the fit, where the error bar represents only the statistical uncertainty in the fit. We can compare this value of α_{Xe} to one calculated using an oscillator strength $f = 0.379$ from Chan *et al.* [100] and a collisional broadening coefficient $\beta = 5.6 GHz/Torr$ extracted from the experimental data in Ferrel *et al.* [99]. The two lines in xenon nearest to the 118 nm light are the Xe $(^2P_{3/2})$5d $\left[\frac{3}{2}\right]$ line at 119.2 nm and the Xe $(^2P_{3/2})$7s line at 117 nm. The contribution due to the 117 nm line is negligible since the oscillator strength is a factor of 4 smaller and the collisional line width is a factor of 5 smaller than the 119.2 nm line. The expected value of α_{Xe} is calculated to be $1.18 \times 10^{-37} cm^5$, in reasonable agreement with our experimentally determined fit value considering the simple model used.

In the case of phase matching with krypton, the Kr $(^2P_{1/2})$5d $\left[\frac{1}{2}\right]$ resonance line at 116.5 nm

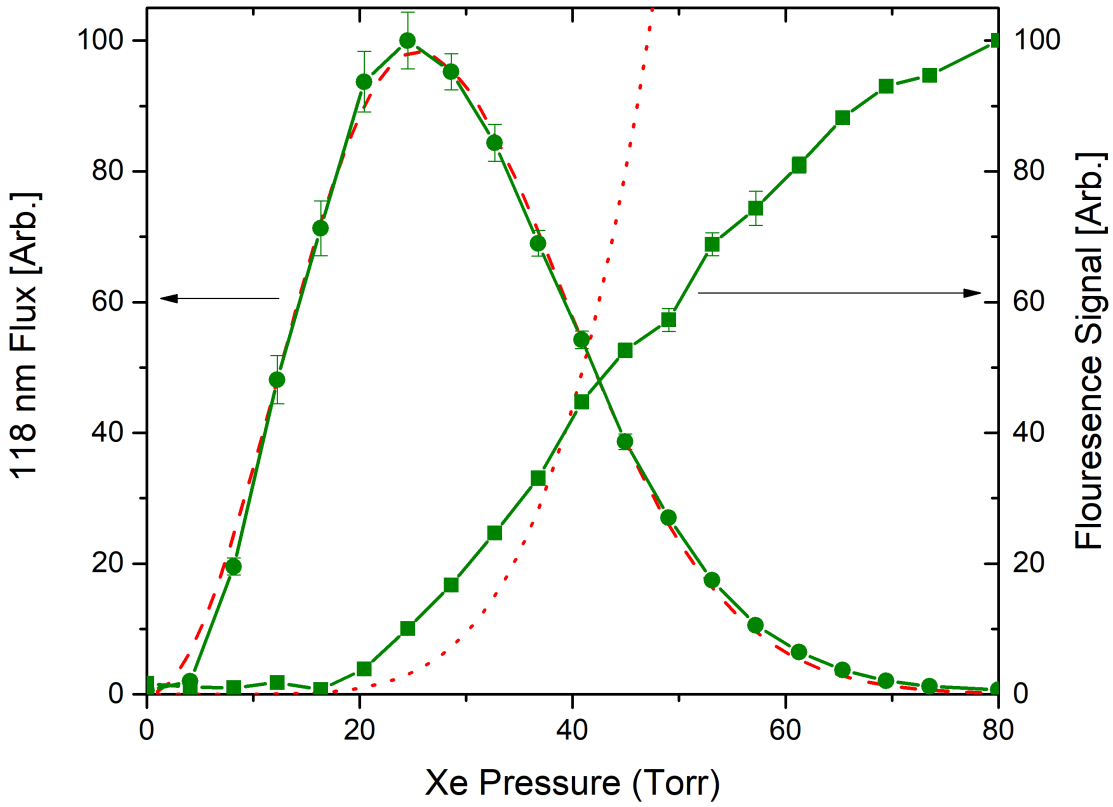

Figure 5.8: Comparison of simulated and experimental results for Xe/Ar. Experimental 118 nm flux and fluorescence signal are plotted as green circles and squares respectively. Simulated 118 nm flux and fluorescence signal are plotted as red dashes and dots respectively. The simulated fluorescence curve is independently scaled by eye.

also leads to absorption of 118 nm light. This can be accounted for with an additional loss term of

$$\left(\frac{d|A_{118}|}{dz}\right)_{Kr} = -\frac{1}{2}\alpha_{Kr}\mathcal{N}_{Kr}^2|A_{118}|, \tag{5.17}$$

where α_{Kr} is the pressure-broadening coefficient due to krypton and $\mathcal{N}_{Kr}$ is the density of krypton. Since the density of xenon and krypton are related by the phase matching ratio, Eqn. (5.15) can be rewritten as

$$\frac{d|A_{118}|}{dz} = \frac{1}{2}\chi^{(3)}\mathcal{N}_{Xe}k_{118}|A_{355}|^3 - \frac{1}{2}\alpha_{Xe/Kr}\mathcal{N}_{Xe}^2|A_{118}|. \tag{5.18}$$

where $\alpha_{Xe/Kr} = \alpha_{Xe} + \alpha_{Kr}R^2$. The results of this model are fit to the experimental Kr results in Fig 5.9, with the model reproducing the shape of the experimental curve. From the fit, a value of $\alpha_{Kr} = 4.6(2)\times10^{-39}cm^5$, can be compared to an expected value of $\alpha_{Kr} = 7.1\times10^{-39}cm^5$ calculated using an oscillator strength $f = 0.193$ from Chan *et al.* [100] and a collisional broadening coefficient $\beta = 3.0GHz/Torr$ extracted from the experimental data in Ferrel *et al.* [99].

For both Xe/Ar and Xe/Kr, the fluorescence results from the model do not match the experimental results well. However, there is some qualitative agreement. The fluorescence appears to turn on near the pressure where the 118 nm flux starts to turn over. The experimental fluorescence appears to increase linearly while the simulated results appear to increase non-linearly. This may be attributed to uncertainties in the fluorescence measurement. The fluorescence streak is several cm long, and extends beyond the window through which we have optical access to collect fluorescence. We collect only a small portion of the fluorescence streak around the focus.

5.7 Discussion and Conclusions

Third harmonic generation of 118 nm light in a Xe/Ar gas cell is a widely used table top source of VUV radiation. The yield of 118 nm light has been observed to diverge from simple theoretical predictions. The observation of ionized xenon at the focus of the 355 nm beam in the presence of 118 nm light suggests two photon ionization, led by absorption of 118 nm light, is the

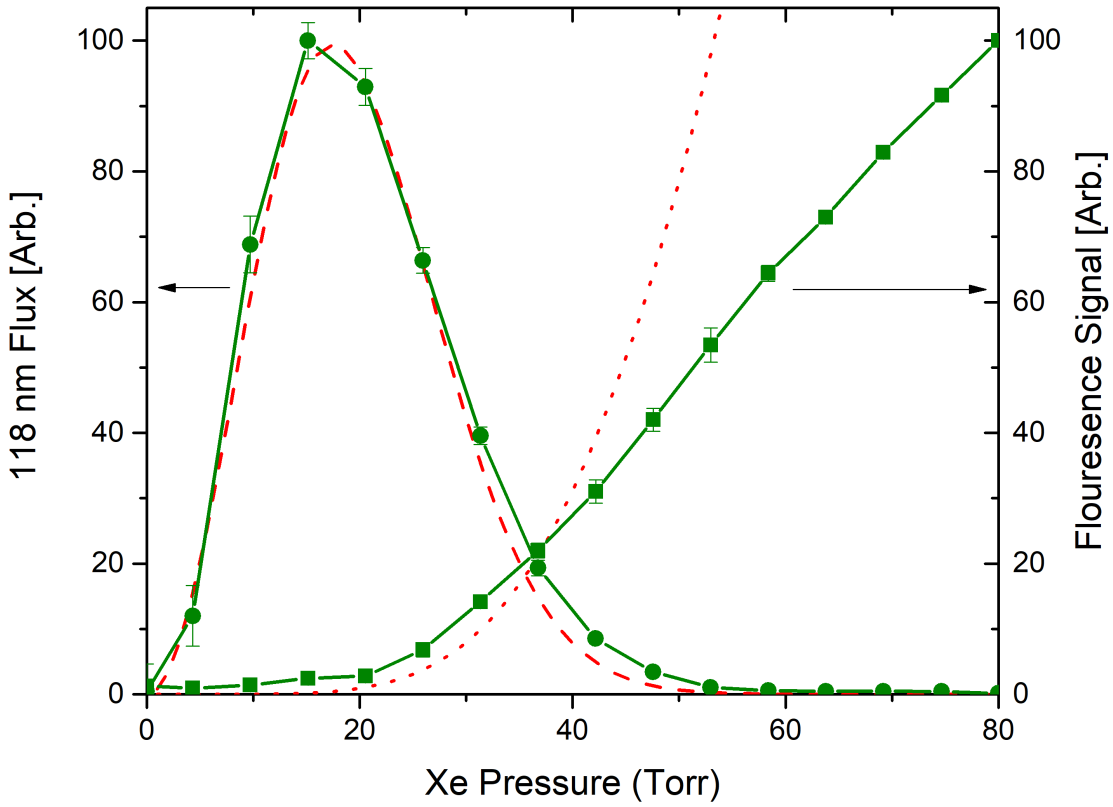

Figure 5.9: Comparison of simulated and experimental results for Xe/Kr. Experimental 118 nm flux and fluorescence signal are plotted as green circles and squares respectively. Simulated 118 nm flux and fluorescence signal are plotted as red dashes and dots respectively. The simulated fluorescence curve is independently scaled by eye.

mechanism limiting the amount of 118 nm light that exits the gas cell. To confirm this mechanism, we developed a model based on pressure-broadened absorption that can be modeled using a simple 1-D simulation. The simulated results are fit to experimental data to extract a pressure-broadening constant, which agrees with values calculated from theory.

A 118 nm light source could be optimized by considering design options that limit the amount of absorption. Minimizing the amount of xenon the 118 nm light must pass through will increase the yield. This can be accomplished by shortening the gas cell and tightening the focus, but the damage threshold of optical components must be considered. Another option might be using a jet of gas rather than a gas cell. While third harmonic generation has been studied in a pulsed supersonic jet of pure xenon, [101, 102] jets of phase matched mixtures have not yet been studied.

Chapter 6

Electrostatic Trapping of OH

In this chapter, we present a reproduction of our paper "Measurements of trap dynamics of cold OH molecules using resonance-enhanced multiphoton ionization" by Gray et al. published in PRA in 2017 [60] The abstract and acknowledgements have been removed, and the bibliographical references and formatting have been changed to match the format of this thesis.

6.1 Introduction

Confining cold molecules in electric, magnetic, or optical traps allows for precision studies of molecules and their interactions due to long interrogation times. Neutral molecule trap lifetimes can range from seconds to minutes [103, 104, 105], depending on the residual background gas pressure and blackbody optical pumping rates [106]. These long interaction times are required to study molecular interactions in cold systems, as the density of trapped samples is typically very low ($10^3 - 10^8$ cm^{-3}) [104, 103, 107, 108]. The long lifetimes increase the probability that interactions can take place before the molecules are ejected from the trap by collisions with background gas or by photon scattering [106]. There have been many recent experiments that have explored various electrostatic [109, 110, 111, 112] and magnetic [113, 114, 115] trapping geometries, and others that demonstrated additional in-trap cooling [116, 117, 118, 119, 120, 121]. Importantly, several experiments have taken advantage of trapped molecules to study the properties of the molecules themselves, including vibrational relaxation of OH [122] and NH [123]. Additonally, studies of molecular interactions have benifited from trapped samples including cold atom-molecule collisions

[25, 124, 125], molecule-molecule collisions [126], and collisionally assisted evaporative cooling [127]. (Here, we restrict our discussions to cold molecules not created by assembly of ultracold atoms.)

One of the most challenging aspects of these experiments is detecting the trapped molecules. The two main methods are laser induced florescence (LIF), where emitted photons are detected using a photo-multipler tube, and resonant ionization, where the resulting ions are detected using a microchannel plate (MCP) detector. Resonant ionization typically has a higher efficiency, as ions can be detected with nearly unit efficiency, while photon collection in LIF is limited by the solid angle of the detection optics, which is only a few percent at best. LIF detection not only produces a lower signal, but can also have a larger noise contribution, as the molecules are trapped close to reflective surfaces, which increases the scattered light impinging on the detector. For ion detection, the ions are usually sent through a time-of-flight mass spectrometer (TOFMS), nearly eliminating the contribution to the noise from other molecular species. Finally, because of the low signal-to-noise (S/N) ratio, experiments that use LIF must illuminate the entire cloud of molecules to increase the number of photons emitted by the molecules. These measurements produce information about only the total trapped number or average density and not about the spatial distribution of the moleules in the trap. Resonance enhanced multiphoton ionization (REMPI), on the other hand, has a high enough S/N ratio that the ionization laser can be focused to illuminate a small portion of the trapped sample. Then, by making measurements of the molecular density at different laser positions, we can profile the density distribution in the trap. The density distribution in the trap can be used to determine the energy distribution or temperature, which are important parameters to measure for many cold molecule experiments. The importance of measuring the density distribution, and not just the number in the trap, was shown in the study of collisions between electrostatically trapped ammonia molecules and magnetically trapped rubidium atoms [25]. Since the density, and thus the collision rate, varies spatially in the trap, extracting collision cross-sections requires a detailed understanding of the molecular distribution. Therefore, studies of trapped molecules benefit greatly from an efficient and spatially selective resonant ionization scheme.

Convenient REMPI schemes have been used to measure the density distribution and under-

stand collisional dynamics with trapped ammonia [25]. However, until recently, the OH radical, which is a fundamental molecule in atmospheric [11], interstellar medium [14, 15], and combustion chemistry [12, 13], did not have an efficient REMPI scheme identified and all trapped studies used LIF [104, 126, 127, 122, 128, 129]. In 2011, the Lester group demonstrated a new UV + VUV REMPI scheme to state-selectively ionize ground-state OH radicals using 118 nm light as the VUV photon [130, 131, 59]. They used the REMPI scheme to examine the OH products from unimolecular dissociation of Criegee intermediates [9, 10]. Here, we present the first measurements of trapped OH molecules using this ionization detection scheme. This method allows us to measure not only the relative number of molecules in the trap, but also the temporal evolution of the spatial density distribution. We use this new capability to measure trap loading dynamics to optimize the loading process and determine the energy distribution in the tap. Proper trap loading and characterization of the energy distribution are important for future atom-molecule collision experiments.

6.2 REMPI of OH

The 1+1' REMPI scheme used to detect trapped OH molecules uses two photons; the first photon causes a bound-to-bound transition around 281 nm and the second photon (118 nm) excites the molecule to an autoionizing Rydberg state whose lifetime is on the order of a picosecond [59]. The relevant energy structure of OH is shown in Fig. 6.1. The trapped molecules are in the ground rotational ($J = 3/2$) and vibrational ($\nu = 0$) state of the $X^2\Pi_{3/2}$ electronic state. The first photon (UV) is tuned to the $A^2\Sigma^+, \nu = 1 \leftarrow X^2\Pi_{3/2}, \nu = 0$ transition. There are several possible rotatonal states to tranfer the molecule into with the UV photon. The stongest A $\leftarrow$ X transision is Q_1 (1.5) shown in Fig. 6.1. Beames et. al observed that in a supersonically expanded jet of OH, the highest ionization signal was achieved when the UV photon was resonant with the $Q_{21}(1.5)$ transition [131]. However, this transition originates from the lower Λ-doublet level and only the upper Λ-doublet level is trappable with the static electric fields used in our experiments. The strongest transition that originates from upper Λ-doublet level is the $R_{21}(1.5)$ transition, which is used in the work presented here. The second step in the process transfers the molecule to an autoionizing Rydberg

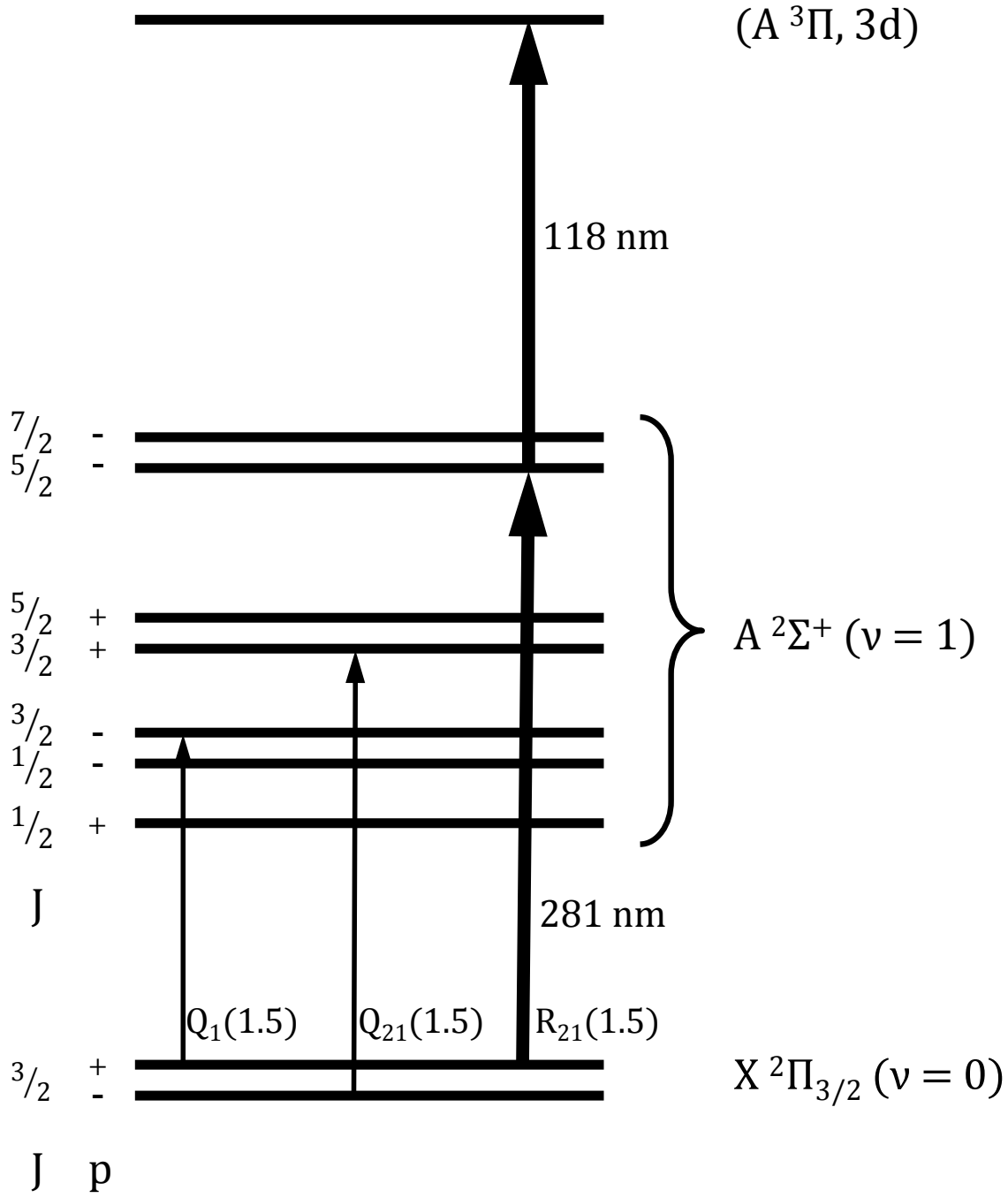

Figure 6.1: Energy level diagram of OH showing the relevant levels for the 1 + 1' REMPI detection scheme. The lowest two levels are the Λ-doublet states of $X^2\Pi_{3/2}$. The first photon is resonant with the $A^2\Sigma^+, \nu = 1 \leftarrow X^2\Pi_{3/2}, \nu = 0$ transition and is denoted by $R_{21}(1.5)$. The second photon transfers the molecule into the $A^3\Pi, 3d$ Rydberg state, from which it autoionizes. J is the total angular momentum, and p is the parity. Vertical spacing between energy levels is not to scale.

state using a 118 nm photon.

6.3 Experimental Setup

The experimental setup is shown in Fig. 6.2. OH radicals are produced at the exit of a piezoelectric transducer (PZT) valve by electric discharge of 1% water seeded in krypton. The molecules are cooled both internally and translationally in the supersonic expansion, producing a beam of OH radicals moving with a mean velocity of 415 m/s and mostly in their rovibronic ground state. The molecular beam is slowed to 34 m/s by a pulsed Stark decelerator, which uses time varying inhomogeneous electric fields to decelerate polar molecules [132]. An electrostatic trap located at the end of the decelerator is used to reduce the mean velocity of the molecules to nearly zero by switching the potentials on the four trap electrodes on and off at different times during the loading process, (Fig. 6.3). The final potentials on the trap electrodes form a 3D trap for OH with a trap depth of 700 μK in the z direction and 250 μK in the x and y directions (Fig. 6.2).

Molecules in the trap are detected using the 1+1' REMPI scheme. The two detection laser beams enter the center of the trap perpendicular to the molecular beam axis through a 3 mm gap between the two central trap electrodes. A frequency-doubled pulsed dye laser, which produces light at 281 nm, excites the OH molecules on the $R_{21}(1.5)$ transition as shown in Fig. 6.1. The 281 nm beam has a beam waist of 2 mm in the y direction and is focused by a 50 mm focal length cylindrical lens to have a beam waist of around 0.5 mm in the z direction at the trap center. The pulse energy of this laser is 4.7 mJ per pulse, which is enough to saturate the transition.

To create the 118 nm light, the third harmonic of a pulsed Nd:YAG laser at 355 nm is frequency tripled in a gas cell containing xenon and argon [133, 134, 135]. The 355 nm light is focused with a 500 mm focal length lens into the gas cell containing 24 torr of xenon mixed with argon at an Ar:Xe ratio of 10.3:1. The xenon provides the non-linear medium, while the argon is used to satisfy the phase-matching condition. We estimate that we create 1 nJ/pulse of 118 nm light. A 250 mm focal length MgF_2 lens, which serves as the vacuum window and separates the gas cell from the ultrahigh vacuum trapping chamber, focuses the 118 nm light to a diameter

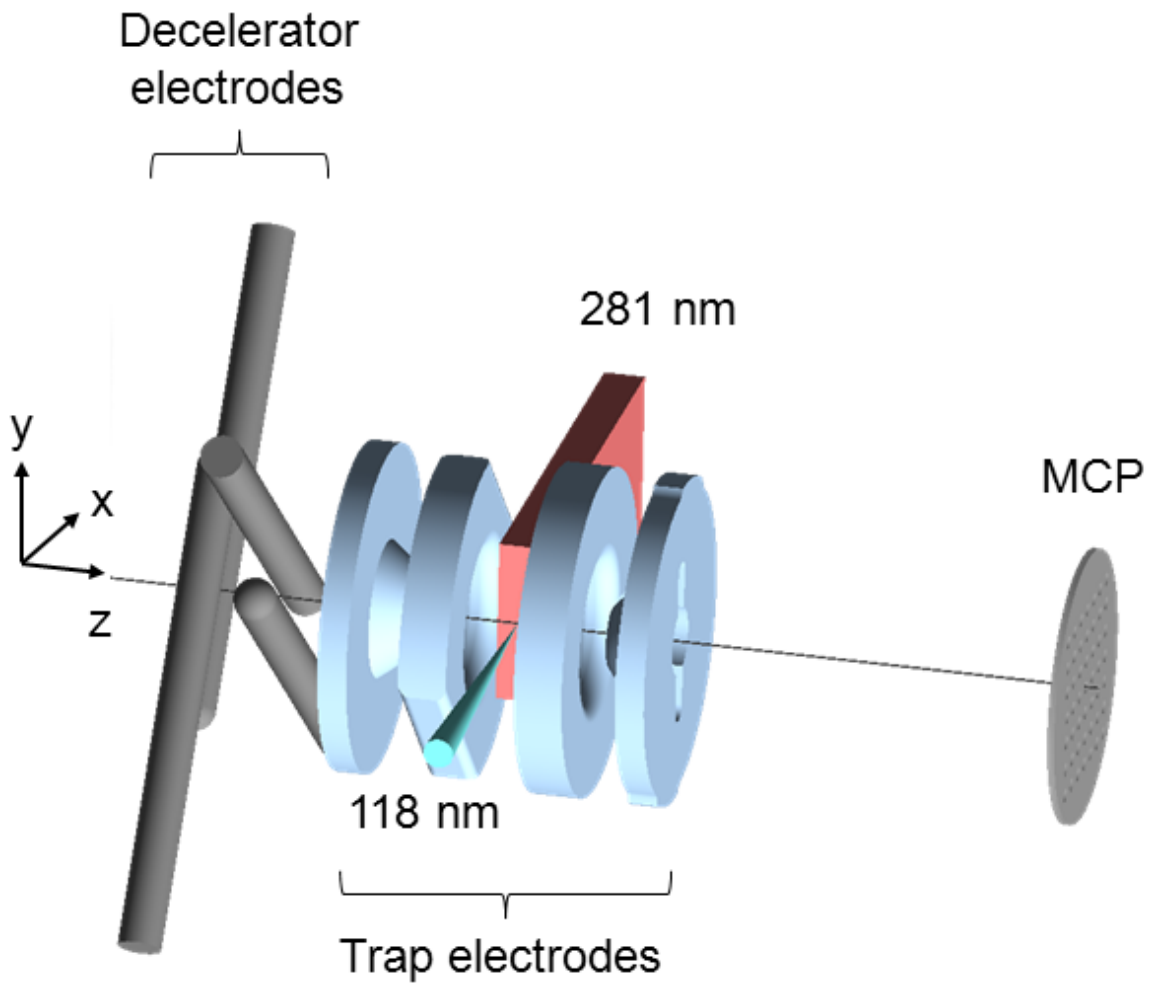

Figure 6.2: Experimental setup showing the last two rod pairs of the Stark decelerator, four trap electrodes, detection lasers, and MCP detector. The red rectangular prism represents the 281 nm laser beam, while the blue cone represents the 118 nm light. The molecular beam propagates along the z-axis. (Not to scale)

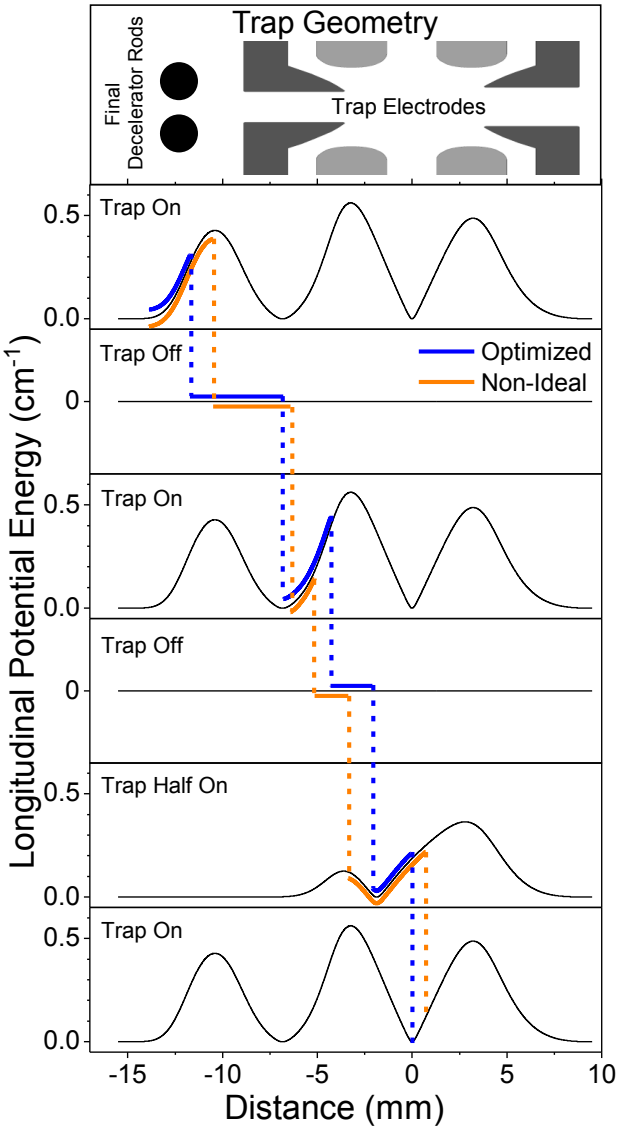

Figure 6.3: Diagram of trap loading process for both an optimized and a non-ideal sequence. The location of the final decelerator electrode and the four trapping electrodes are shown at the top. The longitudinal potential energy curves seen by the OH molecules are shown in the panels for three different configurations of voltage applied. The "Trap on" configuration has the following voltages applied in order from left to right (decelerator, left trap endcap, left trap ring, right trap ring, right trap endcap) = (0, -10, +10, +10, -10) kV. "Trap Half on" has the following voltage configuration (0, 0, +10, 0, -10) kV, and "Trap off" has all electrodes grounded. The blue (top) curve represents the potentials seen by the central molecule in the optimized sequence and the orange (bottom) curve represents the non-ideal sequence. The switches between configurations are shown by vertical lines.

estimated to be 30 μm at the center of the trap. The chromatic dispersion of the MgF_2 lens is used to collimate the residual 355 nm light, the majority of which is blocked by an alumina aperture before the trap. The position of the focus of the 118 nm laser can be scanned both vertically and horizontally using a computer-controlled closed-loop picomotor (New Focus Model 8310).

The central molecular column density and density distribution along the y-axis is measured during the trap loading process, after the trap has been loaded, and after the trap has been turned off to allow the cloud of molecules to expand. During ionization, the potentials on the four trap electrodes are rapidly switched off during the laser pulses, and then changed to (3, 3, 2, 0) kV to create a uniform electric field and accelerate the ions through a TOFMS to an MCP detector. The signal from the MCP corresponding to mass/charge = 17 is recorded via a multichannel scaler (Stanford Research Systems SR430). For all experimental data presented below, each point represents 1000 individual laser shots (100 seconds of integration) with error bars representing the statistical uncertainty in the measurement.

6.4 Molecular Dynamics Simulations

To help interpret the experimental results, three-dimensional molecular dynamics simulations are performed in two stages. The first stage simulates the trajectory of the molecules from the nozzle of the PZT valve to the end of the Stark decelerator. The molecules experience time-varying forces due to the interaction of the molecules' electric dipole moment and the time-varying electric field created by the high-voltage electrodes. More information on this simulation can be found in Refs. [25, 61]. Molecules are then propagated through the trapping region using a second simulation using the phase-space distribution of the molecules from the decelerator simulation as the input. The vector force fields for each configuration of the potentials on the electrodes are generated via a commercial finite element solver, COMSOL, and linearly interpolated to the location of each molecule at every time step. A second-order, symplectic, velocity-Verlet integrator is used to propagate the molecules forward in time. A integration time-step of 2 μs is used to minimize computation time without sacrificing required accuracy. To mimic experimental measurement

conditions, every 50μs, we create a 2D histogram of the number of molecules in the y-z plane, where each bin of the histogram is 50 μm wide in the y- and z-dimensions and is 6 mm long in the x-dimension. This simulated measurement scheme allows us to record data with high spatial and temporal resolution to compare with experimental data. All trapping simulations were run with an initial number of 3.5×10^6 molecules.

6.5 Results and Discussion

6.5.1 Trap loading dynamics

Efficiently loading cold molecules from a decelerator into a trap is critical to be able to perform subsequent experiments, as the number density exiting a decelerator is already low. We use information about the time evolution of the central molecule column density and the in-trap density distribution to optimize loading into a quadrupole electrostatic trap. Previously, only the total number was used in this optimization procedure, which could cause situations where the central column density of the sample was not at a maximum, leading to poor initial conditions for collision studies.

Figure 6.4 shows the column density, which was produced by integrating through the x-dimension, at the center of the trap during the loading process for two sample loading procedures (See Fig. 6.3). The optimized scheme (Fig. 6.4(a)) was created by varying trapping stage times to maximize the column density at the center of the trap at long times in the trap (15 ms). The non-ideal scheme (Fig. 6.4(b)) was made by using a similar optimization procedure, but timings were varied to maximize the column density about 1 mm away from the trap center in the longitudinal direction. This produced an example of a scheme that traps a large number of molecules, but does not produce a high density in the trap center. The non-ideal trapping scheme also induces both longitudinal and transverse oscillations as the trap turns on with the center-of-mass of the molecular cloud displaced from the center of the trap (See Supplemental Material [136] for phase-space movies of both trapping schemes). Typical LIF measurements have used an excitation laser

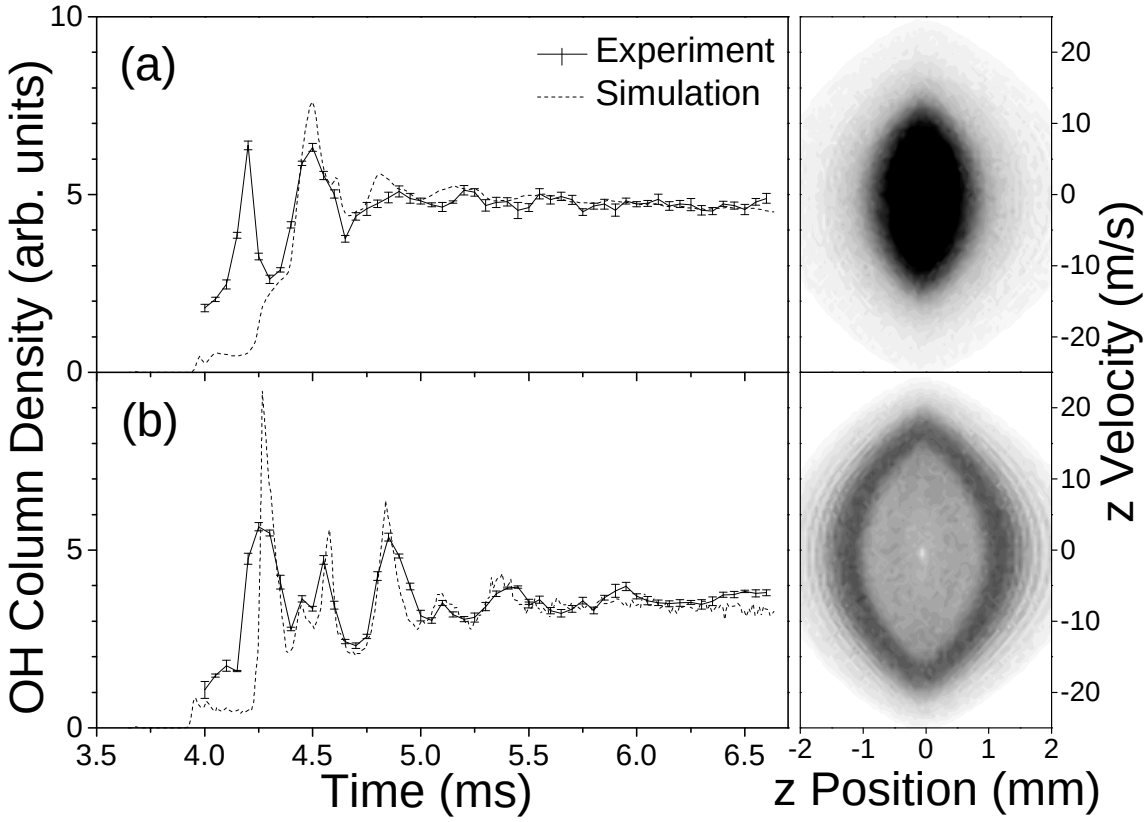

Figure 6.4: Measured central column density during the trap loading process with corresponding molecular dynamics simulations. The measured central density is shown with error bars connected by lines to guide the eye and the simulations results are shown with dashed lines. (a) Results from the optimized loading scheme. The final trap configuration is turned on at 4.34 ms. (b) Results from the non-ideal loading scheme. The final trap configuration is turned on at 4.30 ms. The plots at the right correspond to the simulated longitudinal phase-space distribution after 15 ms of trapping.

with a beam waist on the order of millimeters. So, the two schemes would produce similar LIF signals as they have similar numbers of molecules in the same volume even though the local density within the trap is different.

The results of molecular dynamics simulations are also shown for these loading schemes, and show good agreement of the time evolution of the central column density. Small mismatches between the results of the simulations and the experimental measurements are likely due to the small inaccuracies in the initial molecular distribution used for the trapping simulations. The simulated final phase-space distribution in the trap for the two loading schemes is shown at the right of Fig. 6.4. For the optimized loading scheme, the most dense portion of the phase-space distribution resides at low energies, whereas the molecules are at higher energies in the non-ideal loading scheme. The non-ideal loading scheme produces a distribution that would be unsuitable for collision experiments due to its lower number of molecules in the center of the trap and its higher most probable velocity.

In addition to measuring the peak density as a function of time for the loading, we can also measure the dynamics of the density distribution along the y-axis as shown in Fig. 6.5. Here, the widths are determined by measuring the ions created as the 118 nm laser is scanned along the y-axis of the trap. Since the trapping potentials are not well approximated by either a harmonic or linear potential, an analytic model for the distribution can not be derived from our trapping potentials, so a Pearson IV function was chosen to describe the distribution [137]. The widths of the experimental and simulated distributions were found by fitting to a Pearson IV function and calculating the full width at half maximum (FWHM) from the fit parameters (Fig. 6.6). For the optimized loading scheme, there are few oscillations in the transverse cloud width or the peak density. However, even after a ms in the non-ideal case, there are observable oscillations in both the cloud width and peak density, indicating the cloud was loaded with excess energy.

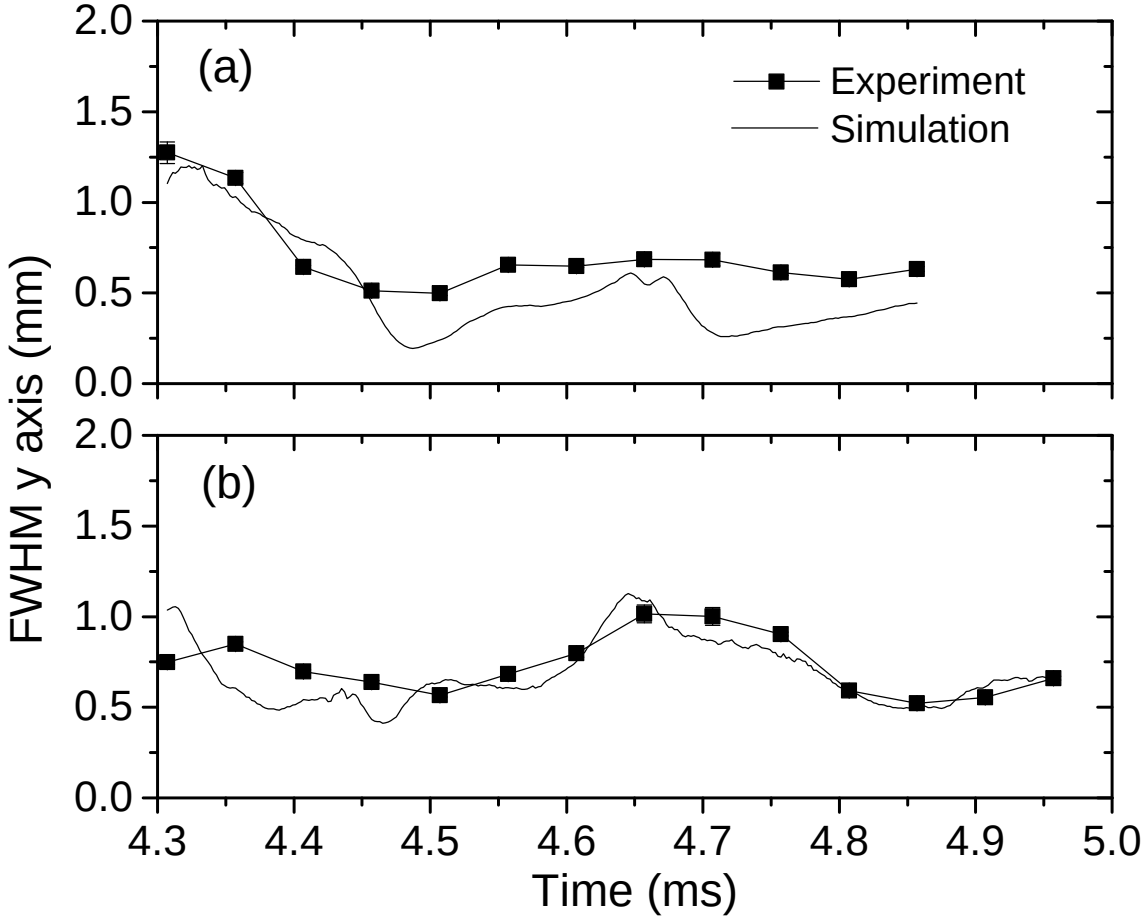

Figure 6.5: Width of the trapped OH cloud as a function of time for the (a) optimized loading and (b) non-ideal loading scheme. The squares represent the experimental measurements, while the solid lines represent simulation results. For both cases, the simulations reproduce the modulation in the width of the cloud after it is trapped. The optimized loading scheme results in fewer oscillations in the cloud width. The statistical uncertainty is on the order of the point size or smaller.

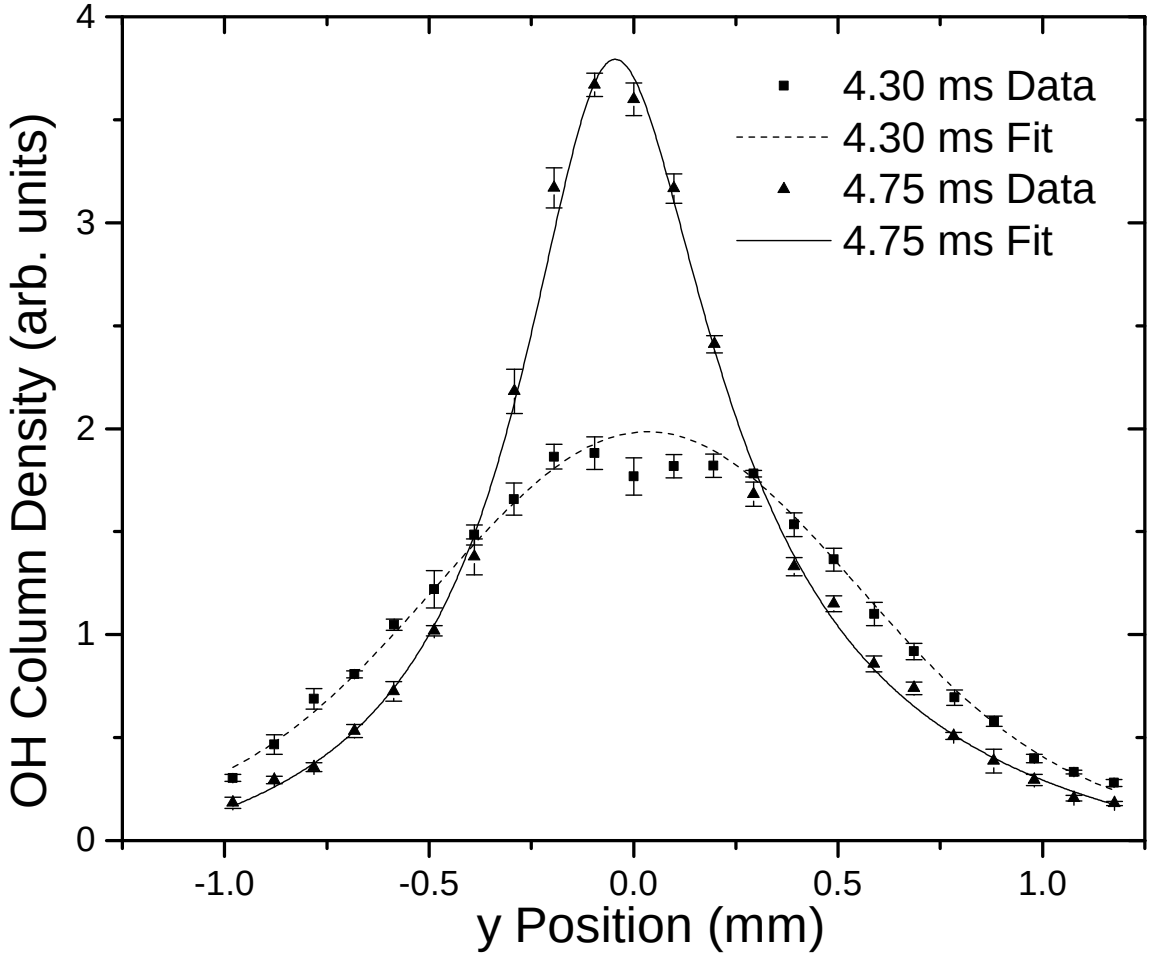

Figure 6.6: Measured density profiles of the OH molecules in the trap using the non-ideal loading sequence. These data were recorded directly after the trap was loaded (4.30 ms) and at 450 μs later (4.75 ms). The lines are Pearson IV distribution fits to the experimental data. The widths of the experimental density profiles are determined by extracting the FWHM of a Pearson IV distribution fit.

6.5.2 Ballistic Expansion of OH cloud

With the ability to measure the density profile, the energy distribution can be determined experimentally from the expansion of the molecules after the trapping potentials have been turned off. Although this method of determining the temperature is standard practice in cold atom experiments, it is not often used in cold molecule experiments. Previous experiments have measured the ballistic expansion of Rydberg molecules from a moving trap; however, their method is unique to molecules that can be easily field ionized [138, 139]. Using REMPI to ionize the molecules provides a more general method to measure energy distributions in cold molecule experiments.

a Figure 6.7 shows the change in the width of the cloud after the trap turns off for the optimized loading scheme after 15 ms of trapping. We fit the width of the cloud as a function of time to the following model $\sigma_y(t) = \sqrt{(\sigma_y(t=0))^2 + (V_{rms}t)^2}$, where $\sigma_y(t=0)$ and V_{rms} (root-mean-square velocity) are fitting parameters, and t is the time after the trap is turned off. Fitting $\sigma_y(t)$ to the experimental and simulated results gives transverse V_{rms} of 5.5 $\pm$ 0.2 m/s and 6.2 $\pm$ 0.2 m/s respectively. This model assumes the cloud is in thermal equilibrium and is contained in a harmonic trapping potential. Although neither of these assumptions are satisfied by our system, we use this model to determine a reasonable value for the V_{rms}. Additionally, one can calculate the rms velocity using the initial size in the trap and the linear potential energy gradient, while employing the virial theorem. Using this, the rms velocity for the experimental measurements (5.92 $\pm$ 0.07 m/s) and results of simulations (5.13 $\pm$ 0.02 m/s). These measured velocities correspond to a temperature of 50 mK. All the uncertainties stated are statistical. Because the system does not satisfy the conditions of thermal equilibrium or harmonic trapping, the systematic uncertainties likely dominate over the statistical ones. However, all measurements are self-consistent, leading to reasonable confidence in the results.

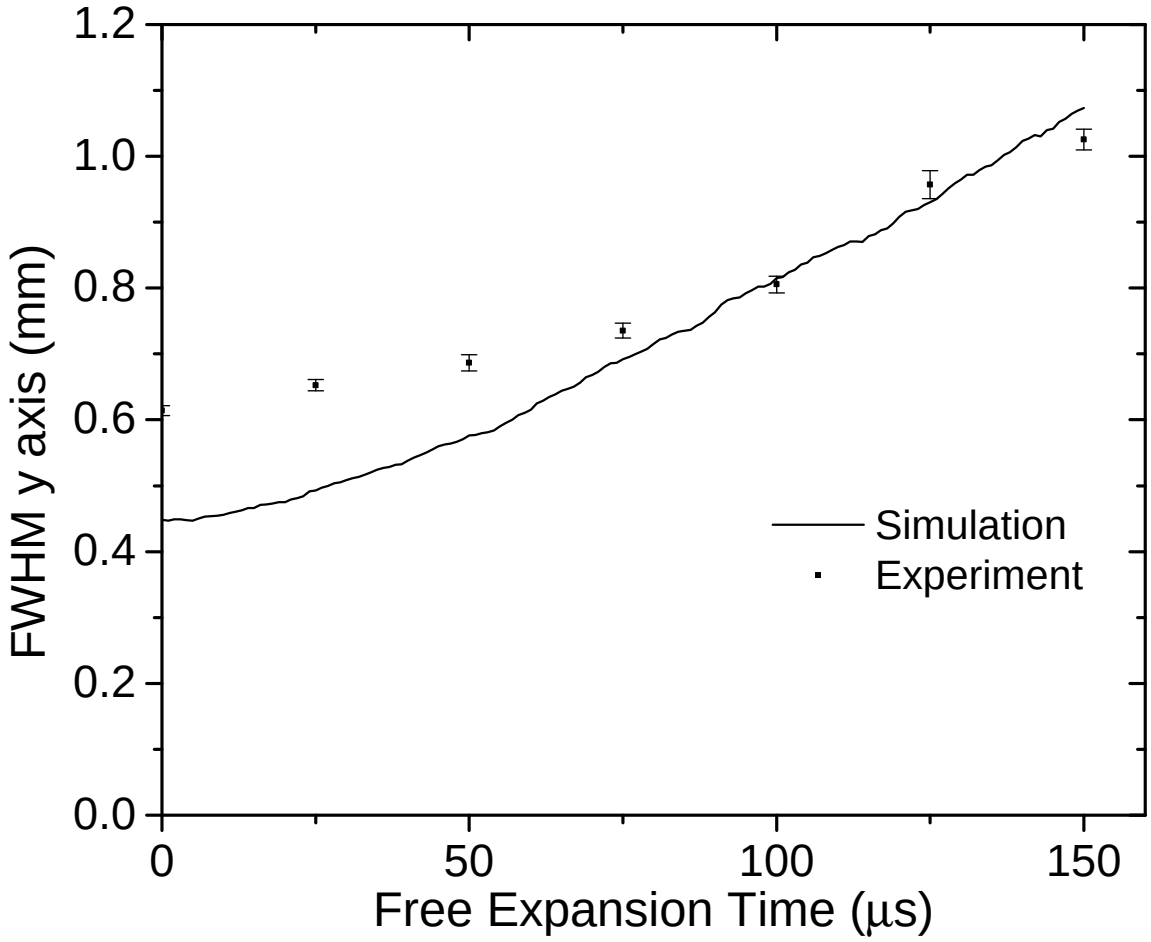

Figure 6.7: Width of the cloud as it expands after the trap is turned off. The molecules were trapped using the optimized loading scheme and held for 15 ms before release in both the experiment and simulation. The initial size of the cloud in the trap differs between the experiment and simulations. This is likely due to the lack of knowledge of the initial distribution of molecules leaving the decelerator.

6.6 Conclusion

Cold, trapped samples of OH molecules could be a useful starting point to explore molecular interactions and cold chemistry. Being able to characterize the trapped samples beyond just total trapped number will be important for these studies. Using a recently developed 1 + 1' REMPI scheme, we have been able to measure the non-uniform density distribution in a trapped sample of OH. This detailed information has allowed us to optimize the loading of OH into an electrostatic trap. Additionally, the new measurement technique provides information about the trapped molecules' energy distribution from the in-trap cloud size and from the rate of expansion after the trapping fields have been turned off. Previously, these dynamics of trapped OH molecules have been inferred from simulations, but never before observed in experiments.

Future work utilizing this detection method includes studying collisions between OH and ultracold Rb atoms. Measuring the density distribution of trapped OH molecules will allow for experimental determination of elastic and inelastic scattering cross-sections in the cold molecule-ultracold atom system. These measured cross-sections will help to improve theoretical models of atom-molecule collisions in the 100 mK temperature regime.

Chapter 7

Measuring Cold Collisions Between OH and Rb

7.1 Introduction

One of the most fundamental rules of thermodynamics is that heat flows from hot to cold. In order to cool something, you must bring it in contact with with something that is colder. In order to further cool cold molecules with temperatures on the order of tens of millikelvin, we need to bring the molecules in contact with something even colder. Since large density samples of ultracold atoms can be easily made in the laboratory, ultracold atoms are often used as the thermal reservoir in which the heat of another species can be dumped. The process of using one cold gas sample to cool another species is known as sympathetic cooling. Sympathetic cooling has been accomplished by using ions to cool ions[31], ultra cold atoms to cool atoms[32], and ultra cold atoms to cool ions[33]. The current frontier in sympathetic cooling is the prospect of using ultra cold atoms to further cool cold molecules, moving these molecular species from the millikelvin to microkelvin regime.

Sympathetic cooling of trapped molecules requires a pair of collisions partners with an elastic cross section that is much larger than the inelastic cross section. Elastic collisions will lead to a transfer of kinetic energy from the hotter species to the cooler species, which drives the cooling. Inelastic collisions, however, are collisions that cause a change in the internal quantum state of one of the species. The large anisotropy of atom-molecule collisions can lead to a large inelastic collision cross section, which presents a unique problem for sympathetic cooling of molecules. [140]

In order to use static fields to trap a molecule, the molecule must be in a weak-field-seeking

state. However, since energy splittings in a field come from energy levels repelling each other, a weak-field-seeking state cannot be the absolute ground state of the molecule. For a trapped molecule, there will always be an energy level below the trapped state for the molecule to fall into due to inelastic collisions. Thus, inelastic collisions will lead to the molecule changing state into an untrapped state and being lost from the system. Since it can take 10-100's elastic collisions to cool the molecules but only a single inelastic collision to knock it out of the trap, the elastic scattering cross section must be much larger than the inelastic to have efficient cooling.

7.2 Theory

The large anisotropy of atom-molecule interactions leads to large inelastic scattering cross sections since angular momentum quantum numbers are no longer conserved.[140] The combination of the $^2\Pi$ OH molecule and the ^2S Rb atom ground states leads to the $^1A'$, ^1A", $^3A'$, ^3A" potential energy surfaces.[141] There is also an ionic state with the same $^1A'$ symmetry as one of the covalent states, which leads to an avoided crossing that could have a large effect on the scattering dynamics. Figure 7.1 shows a couple of these potential energy surfaces, demonstrating the large anisotropy of the interaction.

Lara *et al.* [141] generated and used the above potential energy surfaces to calculate the inelastic and elastic cross sections of the Rb-OH interaction. They use a basis set that considers the hyperfine state of the Rb atom,

$$|Rb\rangle = |f_a m_{f_a}\rangle \tag{7.1}$$

where f is the total spin angular momentum $f = s + i$, with i being the nuclear spin angular momentum. The subscript (a) is used to denote the quantum numbers of the atomic species, vs a subscript of (d) being used when describing the diatom species, the diatomic OH molecule. The basis for the OH molecule is

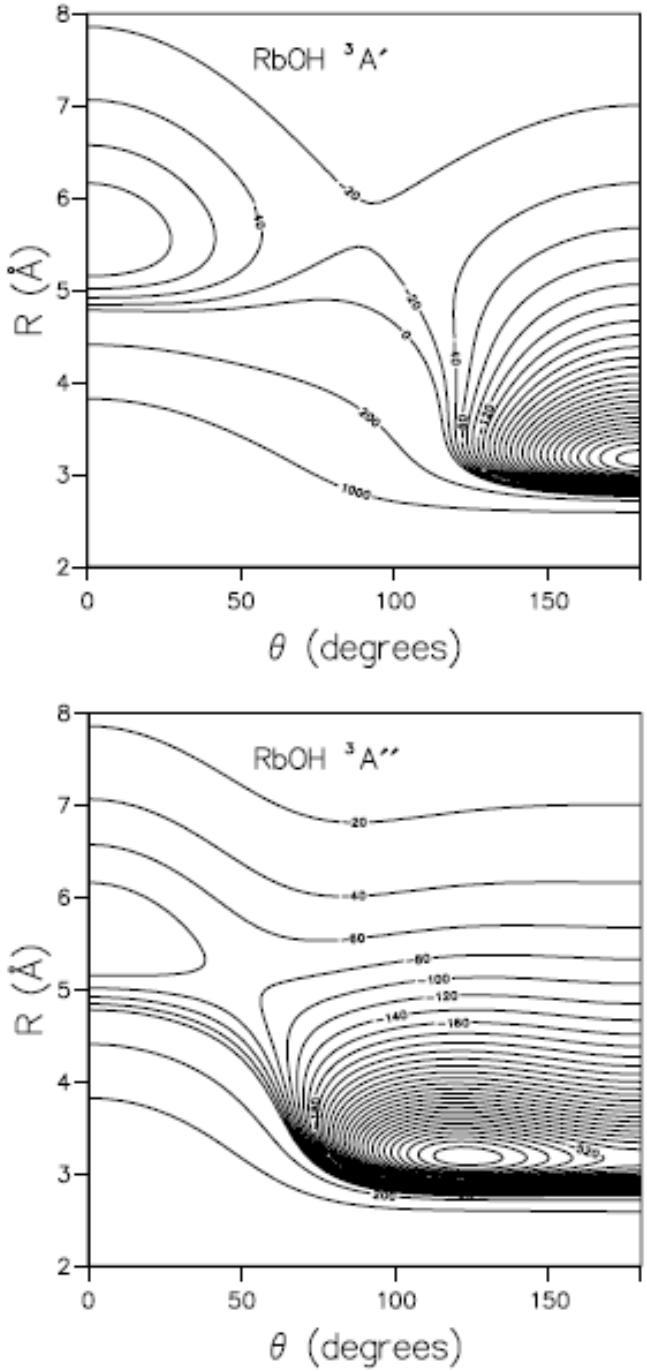

Figure 7.1: Potential Energy Surfaces of the OH-Rb interaction. From [140].

$$|OH\rangle = \left|s_d \bar{\lambda} \bar{\omega} \epsilon f_d m_{f_d}\right\rangle \tag{7.2}$$

where $f = j + i$, and linear combinations of the spin-orbit states are used to produce states of good parity

$$\left|\bar{\lambda} \bar{\omega} \epsilon\right\rangle = \frac{1}{\sqrt{2}}(|\lambda \omega\rangle + \epsilon \,|-\lambda - \omega\rangle). \tag{7.3}$$

With the inclusion of the partial wave quantum numbers $|LM_L\rangle$ to account for the relative orientation of the collision pair in the lab frame, the total basis is given by

$$\left|s_d \bar{\lambda} \bar{\omega} \epsilon f_d m_{f_d}\right\rangle |f_a m_{f_a}\rangle \, |LM_L\rangle \,. \tag{7.4}$$

The incident channels that are considered are shown in Figure 7.2, with channel C1 being the most relevant to our experiment. C1 includes both Rb and OH in their fully stretched states, $|OH\rangle = |\epsilon = f, f_d = 2, m_{f_d} = +2\rangle$ and $|Rb\rangle = |f_a = 2, m_{f_a} = +2\rangle$. In our experiment, Rb is trapped in the $|2, +2\rangle$ state. The hyperfine states of OH that are decelerated and trapped are all of those that are fully stretched by electric fields, or with $\Omega m_j = -9/4$. So the states of OH that are present in the trap are $|OH\rangle = |\epsilon = f, f_d = 2, m_{f_d} = \pm 2, \pm 1\rangle$. [142]

The elastic and inelastic cross sections for channel C1 can be found on the top of Figure 7.3. The cross sections are generally in agreement with two different semiclassical models that describe the behaviour for a higher and lower energy regime. In the lower energy regime, below $10^{-4}K$, the behaviour of the cross sections follows the prediction of the Wigner threshold law. [140] The Wigner threshold law states that as the energy of a collision goes to zero, the cross sections related to an elastic or isoenergetic process will approach a constant value. For an exoergic process, the cross section will vary as $1/\sqrt{E}$. For our system, the OH and the Rb being in the fully stretched states leads to inelastic collisions being an exoergic process. The constants that elastic cross sections approach and the constant of proportionality for exoergic processes are strongly dependent on the potential energy surfaces. The cross sections that Lara *et al.* derive from their potential energy

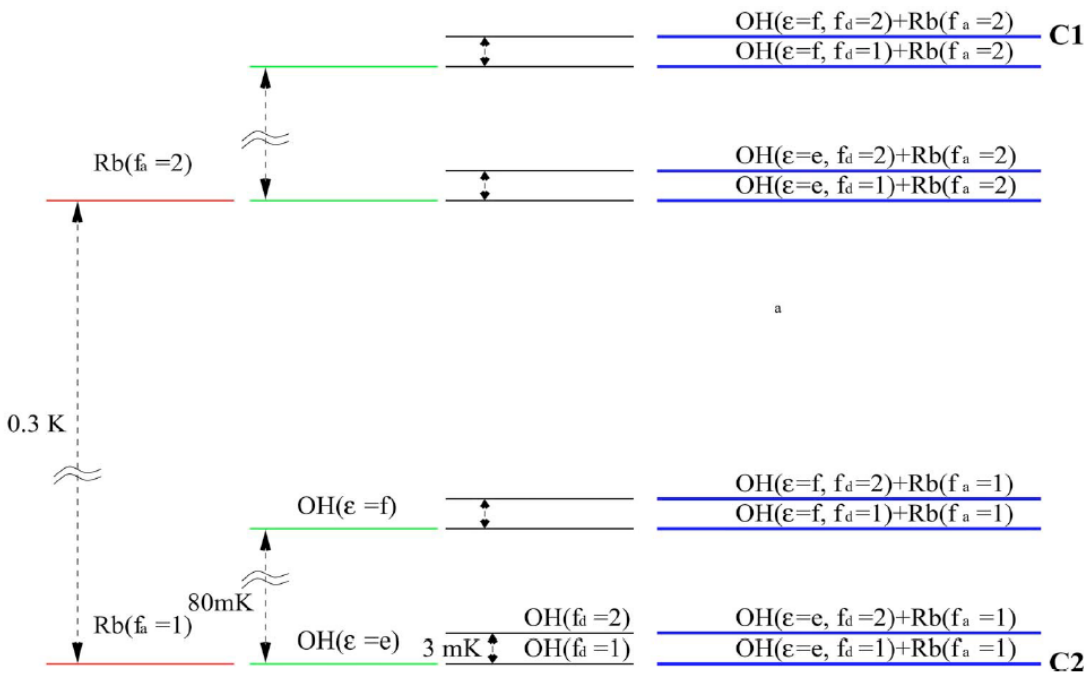

Figure 7.2: Quantum States in the OH-Rb interaction. The states relevant to the experiment are represented by Channel C1. From [140].

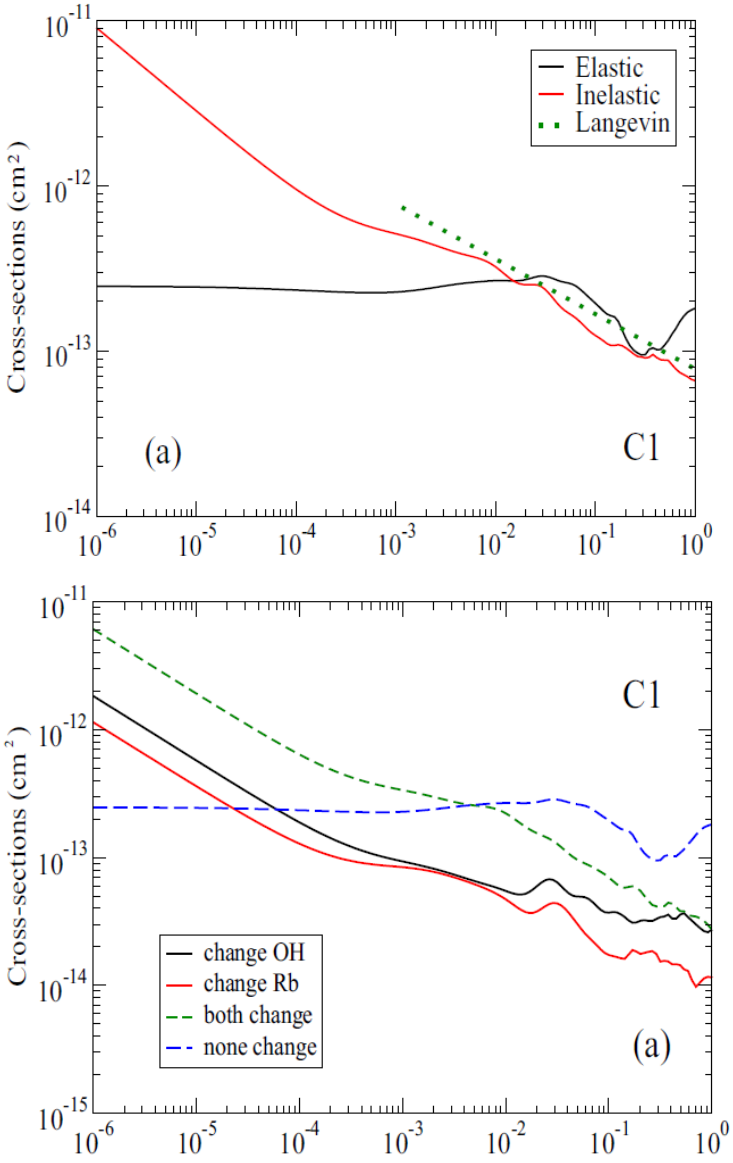

Figure 7.3: Theoretical Cross Sections. From [140]

surfaces paint a grim picture for the prospect of sympathetic cooling. The inelastic cross section is already a factor of 2 above the elastic cross section at 1mK, and they quickly diverge to the point that inelastic scattering is already an order of magnitude more likely at 10 μK.

For higher energies where many partial waves can contribute, above $10^{-2}K$, the inelastic cross section is predicted by the Langevin capture model. [143] In this model, the centrifugal barrier defined by the long range potential

$$V(R) = \frac{-C_6}{R^6} + \frac{L(L+1)}{2\mu R^2} \tag{7.5}$$

gives a maximum partial wave L(E) for a given energy E that will exceed the centrifugal barrier. The Langevin model assumes that any collision that overcomes this centrifugal barrier leads to an inelastic collision with unit probability. When the atom and molecule get near enough to each other, the internal state of both is scrambled and can change to any energetically allowable state. This produces a Langevin cross section

$$\sigma_{Langevin} = 3\pi \left(\frac{C_6}{4E}\right)^{1/3}. \tag{7.6}$$

where $C_6 = 325 E_h a_0^6$ is the isotropic vanderwalls coefficient of the PES.[141] For our trapped OH with a temperature of 50mK, we are within the regime where the Langevin model seems to be valid, and the expected cross sections is $\sigma_{Langevin} \approx 2 * 10^{-13} cm^2$ or $2000 \mathring{A}^2$. Efficient cooling to any point below the starting temperature of the OH does not seem feasible. While the elastic cross section does appear to be larger than the inelastic cross section in the tens of millikelvin region, the elastic and inelastic cross sections are on the same order of magnitude and fast loss from the trap would likely obscure any observable effect of cooling.

There are some areas where the theory used to calculate these cross sections deviates from the conditions used in this experiment. The calculations described above are field free and do not account for the effects an electric field would have. The collision partners in this experiment could experience fields on the order of tens of kV/cm due to the electrostatic trap used to confine the molecules. Electric fields have been shown to strongly affect the inelastic cross sections of cold

atom-molecule collisions. The effect is attributed to a competition between the field, which tends to quantize the molecule at long distances along a lab fixed axis, and the potential anisotropy, which tends to quantize the molecule at short distances along the intermolecular axis. At some intermediate distance during a collision, the two effects balance which leads to an indeterminate quantization axis. This would tend to increase the inelastic cross section and decrease the elastic cross section.

Another difference between the conditions of this experiment and the theoretical calculations is the hyperfine levels included. The calculations above use OH in the state $|OH\rangle = |\epsilon = f, f_d = 2, m_{f_d} = +2\rangle$ as the incident channel, and consider any change of m_{f_d} state to induce a loss from the trap. The states of OH that will be decelerated and trapped in our experiment are the states $|OH\rangle = |\epsilon = f, f_d = 2, m_{f_d} = \pm 2, \pm 1\rangle$. [142] The $m_{f_d} = -2$ and ± 1 states would need to be considered as incident channels to produce a more detailed picture of the theoretical expectations of this experiment. These cross sections would be further complicated by the presence of fields. While states with the same $|m_f|$ are degenerate in electric fields, the magnetic fields would break this degeneracy. [142]

Furthermore, collisions that change the state of the OH molecule from one trapped state to another trapped state would not lead to trap loss and could appear in the experiment as elastic scattering rather than inelastic scattering. However, this effect may be negligible based on the theory presented by [141]. The states of OH that are trapped have the same product $m_j\Omega = -9/4$ and the quantum numbers can be broken down as follows

- $m_f = +2 \longrightarrow \Omega = -3/2, m_j = +3/2, m_i = +1/2$
- $m_f = +1 \longrightarrow \Omega = -3/2, m_j = +3/2, m_i = -1/2$
- $m_f = -1 \longrightarrow \Omega = +3/2, m_j = -3/2, m_i = +1/2$
- $m_f = -2 \longrightarrow \Omega = +3/2, m_j = -3/2, m_i = -1/2$

The nuclear spin projection m_i are untouched by potential energy couplings and will not be changed

in a collision,[141] which rules out many of the possible transitions between two trapped states. The transitions where m_i is conserved involve a very large change of $\Delta m_j = \pm 3$, which would further lessen this effect. The cross sections calculated by Lara *et al.* are seen to decrease the more that m_f is changed, with the cross section of a $\Delta m_j = -3$ transition being an order of magnitude less than for $\Delta m_j = 0$. So this possible effect would likely not significantly increase the experimentally measured cross section nor significantly decrease the inelastic cross section.

7.3 Experimental Expectations

Due to the complex dynamics of the co-trapped environment, extracting cross sections from experimental measurements cannot be accomplished with analytical models, but instead requires comparison to simulated results. However, we can construct an approximate analytical model to estimate what we expect to see from our experiment. To determine if the cross sections calculated by Lara *et al.* are experimentally feasible to measure, we can estimate the rate of collisions and what effect that will have on our measured signal. Since the theoretical predictions indicate efficient cooling is unlikely, we start by considering loss from the trap due to inelastic collisions assuming elastic collisions have a negligible effect. We assume that the colder rubidium atoms are approximately stationary and the contribution to the collision energy is negligible. We approximate all of the molecules to have a constant velocity equal to the average velocity of the cloud. The density of Rb atoms that the OH molecules move through is approximated as the measured peak density. The inelastic collision rate per OH molecule is given by

$$\Gamma_i = \sigma_i v_{OH} \rho_{Rb}. \tag{7.7}$$

where v_{OH} is the average velocity of the OH molecules, which we measured in Chapter 6 to be $5m/s$, and ρ_{Rb} is the peak density of Rb, which we measure to be $10^{10} atoms/cm^3$. This evaluates to each molecule experiencing an inelastic collision at a rate of approximately 1Hz, which corresponds to a 1/e lifetime

$$\tau_i = \frac{1}{\Gamma_i} \approx 1s \tag{7.8}$$

induced by inelastic collisions causing loss from the trap. In this measurement of the OH molecule lifetime, inelastic collisions with Rb are not the only process causing loss from the trap. There are also collisions with background gas and blackbody radiation pumping [144], which lead to a background lifetime, which we measure to be $2.49 \pm 0.15s$. Lifetimes add in parallel and the measured lifetime will be given by the expression

$$\frac{1}{\tau_m} = \frac{1}{\tau_i} + \frac{1}{\tau_0} \tag{7.9}$$

where τ_m is the lifetime measured in the presence of rubidium and τ_0 is the lifetime measured in the absence of rubidium.

We can use Equation 7.9 to estimate the experimental sensitivity to the inelastic collision cross section. Figure 7.4 plots the estimated lifetimes that would be expected to be measured for different inelastic collision lifetimes with $\tau_0 = 2.49s$. In order to distinguish a statistically significant difference between the measured lifetime and the background lifetime, the measured lifetime would need to differ by $2\sigma_{\bar{\tau_0}}$ from τ_0, where $\sigma_{\bar{\tau_0}} = 0.15s$ is the standard error of the mean of τ_0. The shaded red area in Figure 7.4 represents this area that excluded by the sensitivity of our experiments The plot of Equation 7.9 crosses this level at $\tau_i \approx 18s$, which corresponds to an inelastic cross section of $\sigma_i \approx 111\text{Å}^2$. So, the experiment should be sensitive enough to measure inelastic cross sections on the order of $10^{-14}cm^{-2}$ and set an upper limit on the cross section if a significant effect were not seen. On the lower end of τ_i and higher end of σ_i, we are only limited by how small of a lifetime we can measure. This will be determined experimentally by the uncertainty in the interaction time, which is limited by eddy currents induced in the stainless steel vacuum chamber when the magnetic coils turn off. These eddy currents persist for $\sim 1 - 10ms$. To measure a lifetime, we need several time points, so we could measure an inelastic lifetime down to ∼10ms and set an lower limit on the inelastic cross section on the order of $10^{-10}cm^{-2}$.

Estimating the effect of elastic collisions on the signal that we see will be a bit more complicated. Elastic collisions will tend to shrink the width of the OH cloud, which also increases the

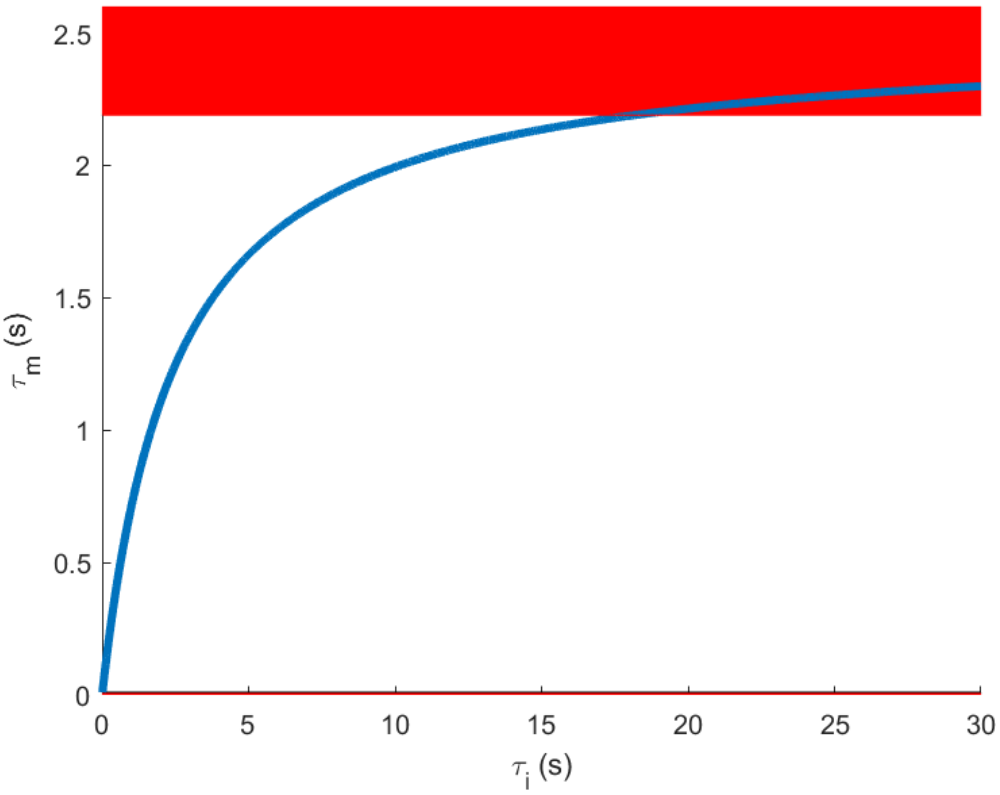

Figure 7.4: Measured lifetime vs collision induced lifetime. As the inelastic cross section decreases (increasing τ_i) the measured lifetime τ_m approaches the background lifetime τ_0. The shaded red area represents the values of τ_m excluded by our estimated sensitivity.

density in the center of the trap. The distribution of the molecules in our trap seems to fit best to a Pearson IV distribution, since the trapping potentials are not well approximated by a linear or harmonic potential and the molecules are not in thermal equilibrium.[60] However, to simplify the math for our estimations, we will model the density as a 3D gaussian. The density of the OH molecules in the trap is then given by

$$n(x,y,z,t) = \frac{N(t)}{(2\pi)^{3/2}\sigma_x(t)\sigma_y(t)\sigma_z(t)} \exp\left\{-\frac{1}{2}\left(\frac{x^2}{\sigma_x^2(t)} + \frac{y^2}{\sigma_y^2(t)} + \frac{z^2}{\sigma_z^2(t)}\right)\right\} \tag{7.10}$$

where N(t) is the total number as a function of time, and σ_x, σ_y, and σ_z are the gaussian widths of the cloud in the x, y, and z directions. The total number over time is simply an exponential decay with a lifetime of τ_m from Equation 7.9

$$N(t) = N_0 e^{-t/\tau_m}. \tag{7.11}$$

In our quadrapole electric field trap with cylindrical symmetry, the widths in all three directions can be related to a single width by

$$\sigma_x = \sigma_y = \frac{1}{2}\sigma_z = \sigma_0. \tag{7.12}$$

and Equation 7.10 becomes

$$n(x,y,z,t) = \frac{2N_0 e^{-t/\tau_m}}{(2\pi)^{3/2}\sigma_0^3(t)} \exp\left\{-\frac{1}{2}\left(\frac{x^2+y^2+4z^2}{\sigma_0^2(t)}\right)\right\} \tag{7.13}$$

When detecting the OH molecules, the ionization laser integrates through the y-axis to give a column density. Assuming that the transverse extent of the laser is much smaller than the cloud, the column density is given by

$$n_c(x,z,t) = \frac{2N_0 e^{-t/\tau_m}}{(2\pi)\sigma_0^2(t)} \exp\left\{-\frac{1}{2}\left(\frac{x^2+4z^2}{\sigma_0^2(t)}\right)\right\} \tag{7.14}$$

By measuring this column density as a function of x by scanning the ionization laser with the pico-motor, we can get a measure of the width of the cloud by fitting to a gaussian. By measuring the change in the width over time we can get an estimate of the elastic cross section.

To estimate the effect of the elastic cross section on the width of the cloud, we need to relate the width of the cloud to the elastic collision rate. From the Virial theorem, we say that the average potential energy is half of the thermal energy. The potentials are approximately linear, so we can relate the average potential energy to the average position to get the width as a function of temperature.

$$\frac{1}{2}k_B T = \langle E_{pot} \rangle = d\nabla E \langle x \rangle \tag{7.15}$$

$$\sigma(T) = \langle x \rangle = \frac{k_B T}{2d\nabla E} \tag{7.16}$$

where d is the dipole moment of OH and ∇E is the gradient of the electric field.

The temperature loss due to the average kinetic energy lost by the molecules per elastic collision with the atoms is given by [145]

$$\Delta T_m = \frac{-(T_m - T_a)}{\kappa} \tag{7.17}$$

where T_m is the temperature of the molecules, T_a is the temperature of the atoms, and κ is the ratio of the sum of the masses to the reduced mass

$$\kappa = \frac{(m_{OH} + m_{Rb})^2}{2m_{OH}m_{Rb}} \tag{7.18}$$

For the OH-Rb system, $\kappa = 3.66$. When the temperature of the molecules is much larger than the atoms, $1/\kappa = 0.27$ is the fraction of the temperature lost from the molecules undergoing one elastic collision on average. Since the width of the cloud is proportional to the temperature, the width will decrease by the same fraction as the temperature. The temperature as a function of the average number of collisions is given by

$$T_m(N) = T_a + (T_0 - T_a)e^{-N/\kappa} \tag{7.19}$$

Equation 7.19 is plotted in Figure 7.5 for a Rb temperature of $T_a = 500\mu K$ and OH temperature $T_0 = 50mK$. It takes 2.5 collisions to drop the temperature by a factor of 2 and 8.5 collisions to drop the temeprature by an order of magnitude. In our experiment, we do not expect the molecule cloud to survive long enough to see many elastic collisions. In the region where the average number of collisions is low, $T_a << T_0$ and Equation 7.19 can be approximated by

$$T_m(N) = T_0 e^{-N/\kappa} \tag{7.20}$$

The temperature could be expressed as a function of time by noting that the number of collisions is the amount of time elapsed multiplied by the elastic collision rate

$$T_m(t) = T_0 e^{-\Gamma_e t/\kappa} = T_0 e^{-\sigma_e v_{OH} \rho_{Rb} t/\kappa} \tag{7.21}$$

This model predicts the temperature and width of the cloud decay exponentially over time with a lifetime of

$$\frac{1}{\tau_\sigma} = \sigma_e v_{OH} \rho_{Rb}/\kappa \tag{7.22}$$

This model neglects the effect of the cooling on the velocity of the OH molecules, which will also be a function of the temperature

$$\frac{1}{2}k_B T = \langle E_{kin} \rangle = \frac{1}{2} m v_{OH}^2 \tag{7.23}$$

$$v_{OH}(T) = \sqrt{\frac{k_B T}{m}} \tag{7.24}$$

As the cloud cools the average velocity decreases, and the elastic collision rate will slow. Since the inelastic collision rate depends in the same way on the velocity of the OH molecules, the inelastic collision rate will also be slowed by elastic collisions. The velocity scales as the square root of the temperature, so the velocity will drop at a slower rate than the temperature, limiting the effect the cooling has on the collision rates.

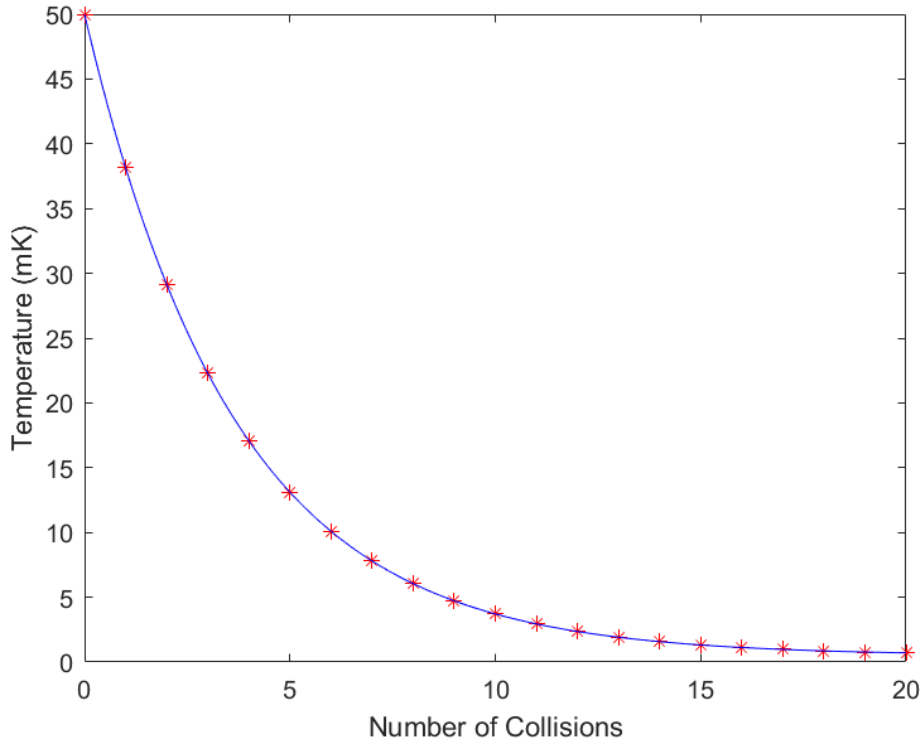

Figure 7.5: OH molecule cloud temperature vs average number of elastic collisions per molecule for an initial OH temperature of 50 mK and initial Rb temperature of 500μK. The red stars represent the values for integer number of collisions to help guide the eye.

The main measurement in our experiment is the column density at the center of the trap, which in our model is given by Equation 7.14 when taking x and z to be 0

$$n_c(t) = \frac{2N_0 e^{-t/\tau_m}}{(2\pi)\sigma_0^2(t)} \tag{7.25}$$

Substituting in our expression for the width we can see that the column density as a function of time is proportional to the product of three different exponentials

$$n_c(t) \propto e^{-t/\tau_0} e^{-t/\tau_i} e^{2t/\tau_\sigma} \tag{7.26}$$

an exponential decay due to the background lifetime, an exponential decay due to inelastic collisions, and an exponential growth due to the shrinking of the width. The measured lifetime of the column density will be a combination of these exponential factors

$$\frac{1}{\tau_m} = \frac{1}{\tau_0} + \frac{1}{\tau_i} - \frac{2}{\tau_\sigma} = \frac{1}{\tau_0} + \frac{1}{\tau_{col}} \tag{7.27}$$

where τ_{col} is the modified lifetime induced by collisions, which can be expressed in terms of the elastic and inelastic collision cross sections

$$\frac{1}{\tau_{col}} = \Gamma_i - \frac{2}{\kappa}\Gamma_e = v_{OH}\rho_{Rb}(\sigma_i - \frac{2}{\kappa}\sigma_e) \tag{7.28}$$

This expression implies that the elastic collisions can have a large effect on the measured lifetime of the column density if the elastic cross section is on the order of the inelastic cross section. Equation 7.28 equals 0 when the elastic cross section is greater than the inelastic cross section by a factor of $\kappa/2 = 1.88$, which is not unlikely based on the field free theoretical predictions around 50mK.

7.4 Collision Measurement

The apparatus used to measure cross sections is illustrated in Figure 7.6. Rubidium atoms are trapped and cooled in a magneto-optical trap (MOT). Once the MOT is loaded to the desired level, the atoms are optically pumped and the anti-Helmholtz coils that produce the quadrapole

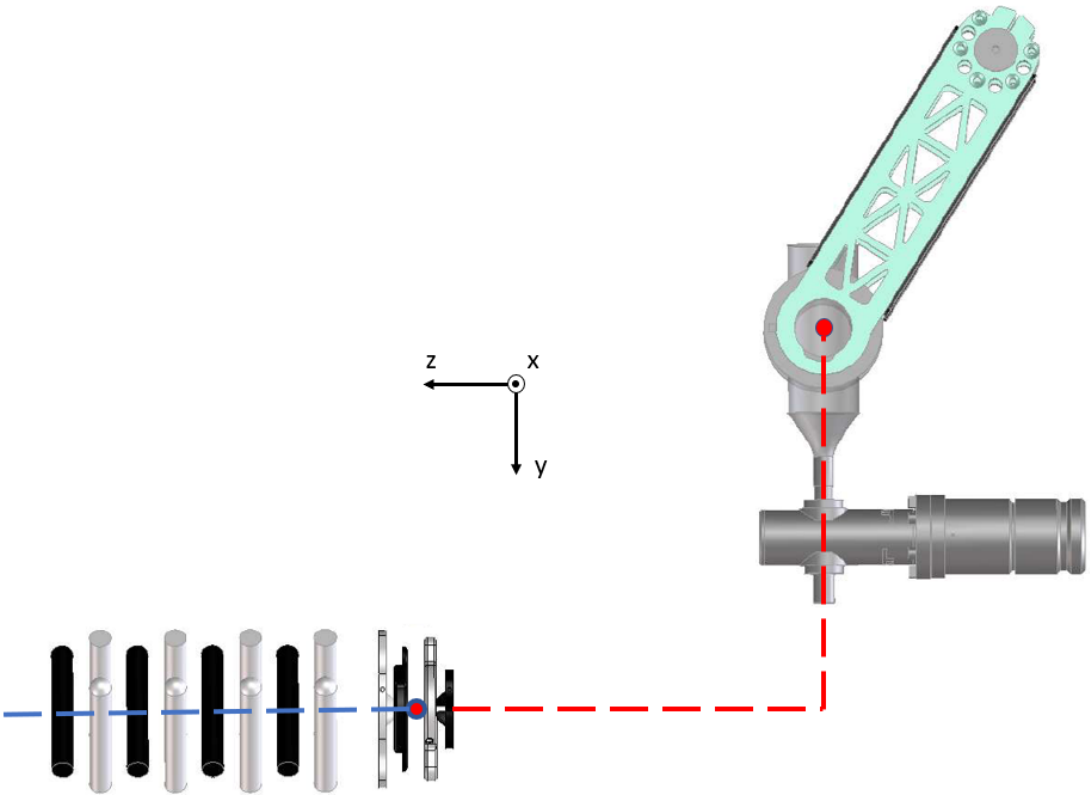

Figure 7.6: OHRbIT Apparatus. The Rb atoms are trapped in a separate glass chamber, separated by a gate valve. The coils are mounted on movable track that transports the coils outside of vacuum while holding the atoms inside the vacuum chamber. The path of the atoms inside of vacuum is an L shape, represented by the dashed red line. The atoms are loaded through an aperture in the back of the electrostatic trap.

magnetic trapping field are ramped to 500A. This traps a total of $N \sim 10^9$ atoms with a peak density of $n \sim 10^{10} atoms/cm^3$ at a temperature of $T \sim 500\mu K$. The magnetic coils sit outside the vacuum chamber on a series of two movable tracks. The first track moves the atoms along the atom trapping chamber through an all-metal gate valve and into the science chamber to align with the electrostatic molecule trap in y direction. The second track moves the atoms through the back of the molecule trap to align with the center of the trap. After the atoms are in place, the molecules are fired from the valve, decelerated, and trapped as described in Chapter 6. The molecules are detected via REMPI as described in Chapter 4.

The ionization signal of the OH is plotted in Figure 7.7 as a function of interaction time with and without atoms. The signal with atoms present decreases much quicker than without atoms. This is clear evidence that we are observing inelastic collisions between OH and Rb. When fitted to a simple exponential decay, the lifetime without atoms is $\tau_0 = 2.49(15)s$ and the lifetime with atoms is $\tau_m = 0.94(7)s$. The lifetime of the column density due to collision is then $\tau_{col} = 1.51(18)s$, or $1/\tau_{col} = 0.66(9)Hz$.

From this collision induced lifetime, we can estimate the elastic and inelastic cross sections. Equation 7.28 can be rearranged to give

$$\sigma_i = \frac{\frac{1}{\tau_{col}}}{v_{OH}\rho_{Rb}} + \frac{2}{\kappa}\sigma_e \tag{7.29}$$

which is a relation between the cross sections that depends on the measured collision induced lifetime. The values of σ_i and σ_e will lie along a line with slope $2/\kappa$. The values in Equation 7.29 that vary with experimental conditions and results only change the intercept of the line. Equation 7.29 is plotted as the black line in Figure 7.8. The horizontal dashed red line represents the inelastic cross section predicted by the Langevin model. The vertical dashed red line represents the elastic cross section predicted by Lara *et al.* at 50mK.

The use of the average velocity for v_{OH} and the peak density for ρ_{Rb} are both overestimates of the conditions the OH molecules most of the time in the trap. A particle in a trap spends most of its time at a slower velocity near the edges of the trap. To produce a likely underestimate

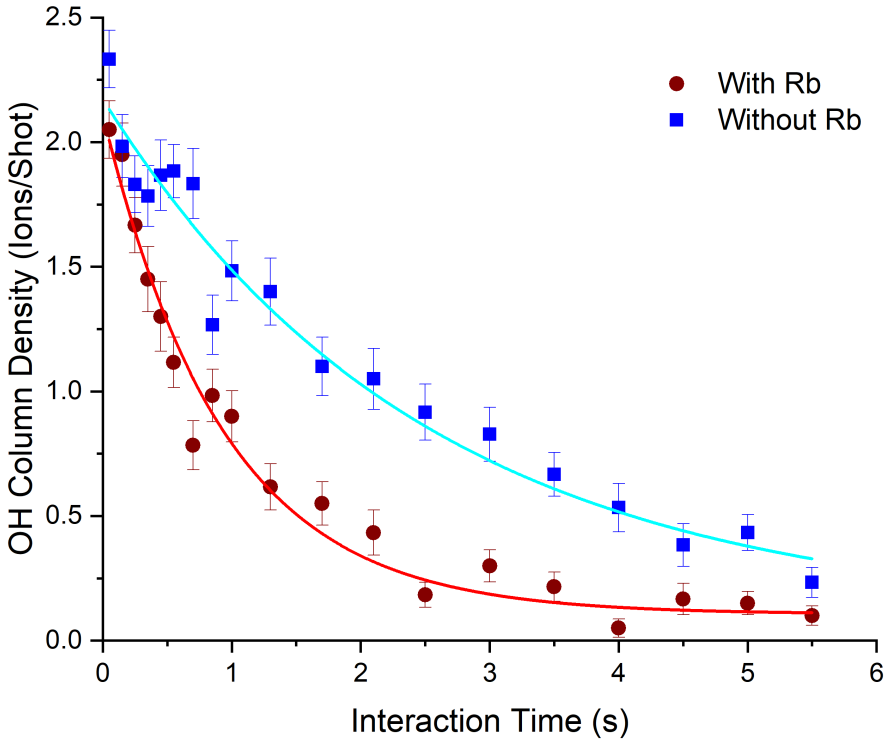

Figure 7.7: OH Signal vs Interaction Time. The blue points are without Rb atoms present and the red data is with Rb atoms present. Fit to an exponential decay, the lifetime without Rb atoms is $\tau_0 = 2.49(15)s$ and the lifetime with atoms present is $\tau_m = 0.94(7)s$.

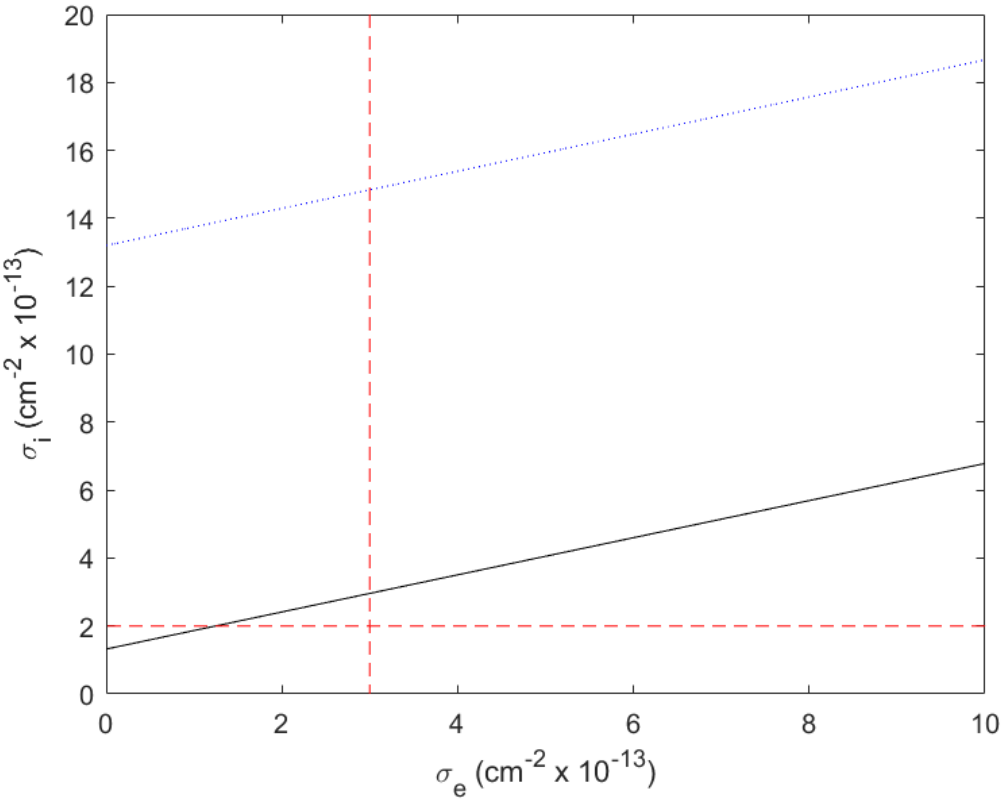

Figure 7.8: Relation between Inelastic and Elastic Cross Sections. The Inelastic and elastic cross sections lie on a line, with the intercept being determined by the measured OH decay curve. The solid black and dotted blue lines represent under and overestimates of the intercept described in the text. The horizontal and vertical dashed red lines represent the theoretical predictions of the inelastic and elastic cross sections respectively.

of these parameters, we take the product $v_{OH}\rho_{Rb}$ to be an order of magnitude lower than our initial estimate. This shifts the intercept to produce the dotted blue line in Figure 7.8. The true cross sections likely lie in the region between the solid black and dotted blue lines. To constrain the inelastic cross section, we could use the change in the width of the OH cloud to estimate the elastic cross section. Preliminary data (Figure 7.9 shows no significant change in the width over an interaction time of 1s, so the elastic cross section is on the lower side of this graph and the inelastic cross section is likely on the order of $10^{-13}cm^{-2}$. The theoretical predictions in Lara *et al.* are claimed to be within a factor of two, and the estimates based on our experimental data seem to agree with those prediction. In order to extract values and quantitative uncertainties for the cross sections from our data, we will need to use Monte Carlo simulations of the co-trap environment. This process is described below in the Future Work section of this chapter.

7.5 Data Taking Procedure

In order to isolate the effects of the atoms on the molecules, a procedure was designed to ensure the only change between shots with atoms and without atoms was the presence of the atoms. For the shots without atoms, the only difference in procedure is that the laser that repumps atoms in the MOT is shuttered, preventing atoms from being trapped. The atom trapping apparatus still goes through the procedure of waiting the ∼15 seconds it takes the MOT to load, ramping up the magnetic fields, and moving the magnetic coils to overlap with the molecule trap. The components of the molecule trapping apparatus that may pick up noise still sees all of the possible noise sources from the atom trapping apparatus, such as vibrations caused by the movement of the track and electrical pick up noise from the large changing magnetic fields from the trapping coils.

The time points were chosen to have a variable interval meant to capture the fast decay expected for the signal with atoms and the slow decay expected for signal without atoms. From preliminary data, we determined an interval of 100ms at short times would be appropriate to measure the fast decay. The lifetime without atoms is $\sim 2.5s$, and time points were chosen to be far enough out in time to fit the lifetime appropriately. The data is interleaved, alternating between

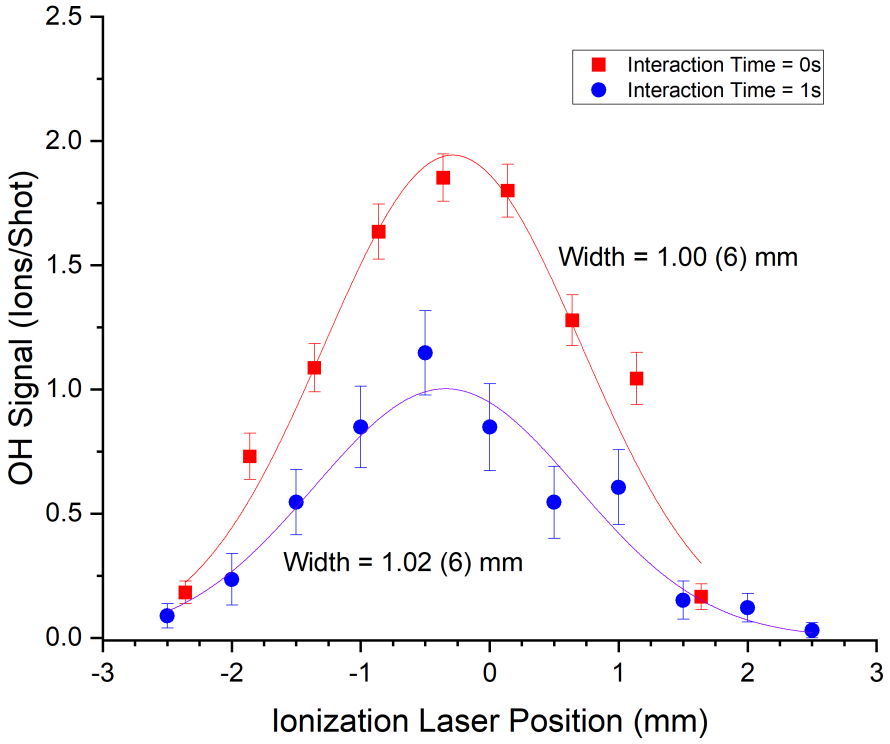

Figure 7.9: Preliminary scans of the OH cloud density profile at interaction times of 0s and 1s. The red squares are the initial distribution at interaction time of 0s. The blue circles are the distribution after interacting with Rb atoms in co-trap for 1s. The similarly colored lines are a Gaussian fit to the data. The Gaussian width for 1s, $\sigma(1s) = 1.02(6)mm$, does not differ significantly from the width at 0s, $\sigma(0s) = 1.00(6)mm$

a shot with atoms and a shot without atoms. A pair of shots with and without atoms takes $\sim 50s$. We take 60 shots for each time point, for a total integration time of ~ 16 hours.

Due to the long integration time, the procedure was designed in order to minimize the possible effect of systematic error sources that may change over time, such as laser powers and wavelengths. A vector of the time points is created in random order with no repeats. A pair of interleaved shots is taken at each time point before creating a new randomized vector to repeat each time point. In this way, the number of shots taken for each time point is the same on the time scale that experimental drifts may happen. Each single shot of the experiment is recorded with a time stamp. Some experimental conditions, such as the status of the laser locks, are also recorded with a time stamp which allows data to be rejected if there are known problems that might affect the quality of the data. A histogram of the single shots at each time point can be compared to a Poisson distribution to check if the data appears to follow counting statistics. The data can also be checked for an abundance of 0 count shots, which may indicate an intermittent problem destroying the signal.

Data taking is interrupted at regular intervals, corresponding to a set amount of shots at each time point. During these interludes, some benchmark signals are measured in order to check that the experiment is operating in a consistent manner. This is important to ensure that all of the data is directly comparable across the long integration time. First, the molecule signal at zero interaction time is checked to ensure there has not been a change in the initial number of molecules in the trap or the REMPI detection efficiency. The most common problem that may affect the measured molecule signal is drifts in the wavelength of the dye laser that produces the 281nm light. The Xe:Ar gas mixture for producing the 118nm light can also require refreshing. Next, the number of atoms is checked for interaction times of 0s and 1s. The atom number is determined by transporting the atoms to overlap with the electrostatic trap for a set amount of time before transporting the atoms back to the glass cell where the atoms are measured using absorption imaging. The atom number is measured at 0s interaction time to check the initial number of atoms that are trapped. Deviation from previously measured atom numbers are most likely due to wavelength and alignment drift of

the optical pumping laser. The atom number is then measured at 1s interaction time as a check on the alignment of the magnetic trap to the electrostatic trap. If the atom number at 1s deviates from what was previously measured, the likely cause is an error in the positioning of the track along the z-axis. While this track mostly operates within the expected encoder error on the order of $10\mu m$, we have occasionally observed the track to spontaneously generate an error of 1mm and require realignment.

7.6 Co-Trap Alignment and Characterization

In order to measure collisions effectively, and accurately simulate the measurements made by the apparatus, we need an accurate co-alignment of our electrostatic trap, magnetic trap, and ionization laser. The electrostatic trap is stationary, so we need to move the magnetic trap and 118 nm beam to overlap with the center of the electrostatic trap. Figure 7.6 shows the geometry of the combined trap apparatus. The electrostatic trap creates a quadropole electric field with approximately cylindrical symmetry. The strong axis of the electrostatic trap is aligned to the z-direction, while the radial direction of the trap is in the x-y plane. The anti-Helmholtz coils of the magnetic trap are not aligned along the same axis as the electrostatic trap. The magnetic quadropole field has its strong axis aligned to the x-direction and the radial symmetry is in the y-z plane.

In the co-trap environment, the Rb atoms and OH molecules both will experience Zeeman and Stark shifts due to the magnetic and electric fields present. The OH molecule trapped in the fully stretched Stark state includes m_f levels that are both weak and strong field seeking. However, the Zeeman shifts the molecules will see are small enough relative to the Stark shifts to be negligible, and do not affect the trap depth or the dynamics of the molecules in the trap. The Rb atoms, however, are polarizable and experience a Stark shift that significantly affects the dynamics of the atoms in the co-trap. The Hamiltonian describing the dc Stark effect on Rb is

$$H_S = -\frac{1}{2}\alpha_0 E_z^2 - \frac{1}{2}\alpha_2 E_z^2 \frac{3J_z^2 - J(J+1)}{2(2J-1)} \tag{7.30}$$

where α_0 and α_2 are the scalar and tensor polarizabiliteis of Rb.[146] When J=1/2 the second term vanishes. For the $S_{1/2}$ state of Rb 87, the scalar polarizability is $\alpha_0 = h * 0.0794 Hz/(V/cm)^2$. This Stark potential decreases with increasing electric field magnitude and is quadratic. Near the center of the co-trap the linear Zeeman potential dominates and the Rb atoms remain trapped. However, there is a point around 1-2 mm from the trap center where the Stark shift overcomes the Zeeman potential, leading to holes in the trap that cause loss from of Rb atoms form the co-trap. The number of Rb atoms follows a double exponential decay of in the presence of the electric fields. The initial fast decay is due to the loss of atoms by the reduction of the trap depth. While this loss does limit the number of atoms available for collisions, the effect can be exploited to help align the centers of the traps. If the centers of the traps are offset in some direction, the co-trap potential will be asymmetric with one side being weaker than a properly aligned trap. Misalignment leads to a faster trap loss, and the lifetime of the atoms is maximized when the co-trap is well aligned.

One might think that alignment along the z-axis could be achieved by scanning the ionizaiton laser over the trapped molecular cloud and assigning the center to the point where OH^+ ion signal is maximized. However, attempting this alignment would introduce a few problems. First, the counterpropogating 281 nm laser beam, which provides the first photon in the REMPI detection scheme, is focused through the trap with an estimated beam waist of $500 \mu m$. Thus, the 281 nm beam would need to be realigned by hand for each new alignment of the 118 nm beam in order to deconvolve the beam width from the measurement of the cloud. This realignment would be tedious to repeatedly perform. It could also potentially introduce systematic errors with constantly having to re-optimize the detection efficiency at each new position. Second, the time of flight of the OH^+ ions would change with ionization laser position. To reduce the effect of noise peaks, only peaks that have an arrival time within a small time window are assigned as OH^+ and counted as part of the ion signal. This time window would need to be identified and shifted for each new laser alignment. With a single laser ionization scheme, these potential detection problems would be alleviated.

Instead, we first align the atoms along the z-axis to the electric field then align the ionization

laser to the atoms. To align the atoms along the z-axis we exploit the fact that the lifetime of the atoms is reduced when the electrostatic trap and magnetic trap are not aligned. The fast loss of atoms from the co-trap in the first 100's of us is the main cause of reduction in atom number. The alignment procedure involves (1) moving the atoms into the electrostatic trap (2) pulsing the electric fields on for 1s (3) moving the atoms back to take an absorption image (4) fitting the absorption image to determine the remaining amount of atoms. The surviving atom number is plotted in Figure 7.10 This procedure is repeated while varying the final positions of the magnetic trap. Loss of atoms due to the electric fields is minimized when the center of the magnetic trap aligns with the center of the electric fields. Since the z-axis is the strong axis of the electrostatic trap and one of the weak axis of the magnetic trap, the z-axis is the most sensitive to this alignment with a FWHM of 200um. This suggests our determination of the center of the trap can be on the order of 10's of um from a Gaussian fit, when our 118nm laser beam waist is 50um. We should be able to align the center of the atom distribution to the center of the electric trap well enough to use the atoms as a tool to align the ionization laser. Using the picomotor to scan the ionization laser while measuring the Rb^+ ion signal, we find the center of the distribution by fitting to a Gaussian. The Rb Ionization signal is plotted in Figure 7.11

Alignment of the 118 nm laser in the x-direction (lab vertical) is easily achieved using a picomotor scan of the molecules in the trap, shown in Figure 7.12 This scan is fit to a Gaussian whose center is at the trap center, which is determined with an error of 10s of um. The laser is then set to this center and its position acts as a reference for aligning the atoms to the vertical center of the trap. While monitoring the Rb^+ ion signal, we vary the difference between currents applied to the magnetic trapping coils, shown in Figure 7.13. This has the effect of scanning the atoms across the laser beam, and the center of a Gaussian fit of the Rb^+ ion signal corresponds to the alignment of the magnetic trap to the electric trap.

Alignment of the atoms in the y-direction is limited to measuring atom loss due to E-fields at various alignments. The y-axis is a weak axis for both traps, and the atom loss is not as sensitive to misalignment as the axes. We move the atoms into the electrostatic trap and hold for 8 seconds

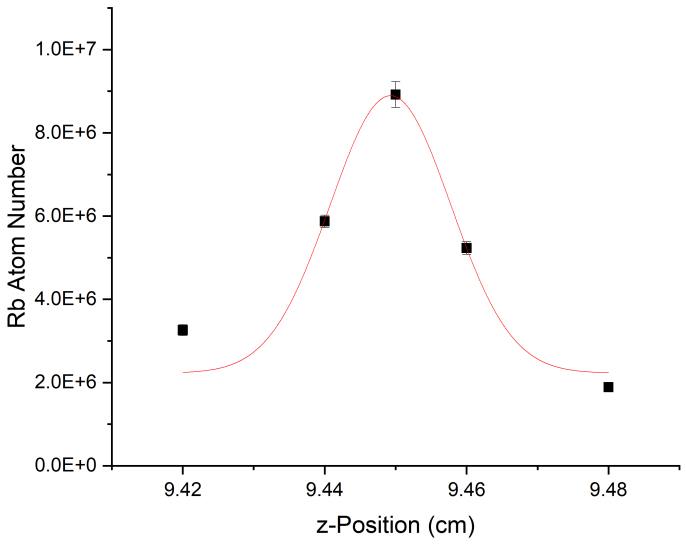

Figure 7.10: Alignment of the Rb atoms along the z-axis. The Rb atoms are brought to the electrostatic trap and the trapping fields are turned on. After 1s the electrostatic trap is turned off and the Rb atoms are transported back to the glass cell where the survival number is determined by absorption imaging.

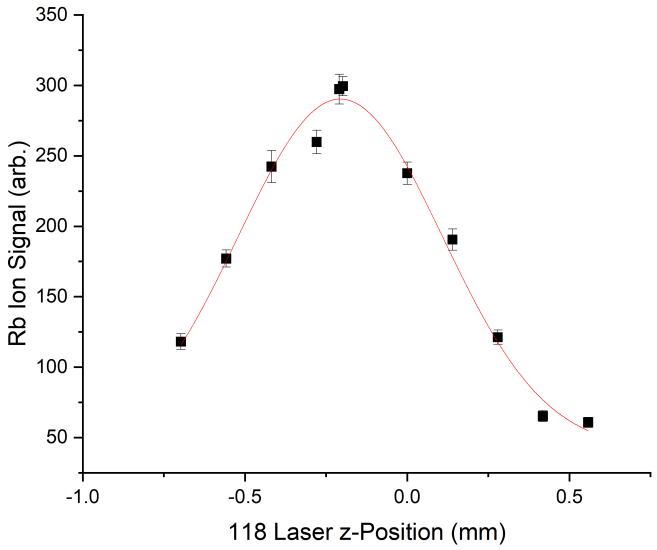

Figure 7.11: Alignment of the 118nm laser along the z-axis. After alignment of the Rb atoms to the electrostatic trapping fields along the z-axis, the 118nm laser position is scanned along the z-axis to find the center of the Rb atom cloud.

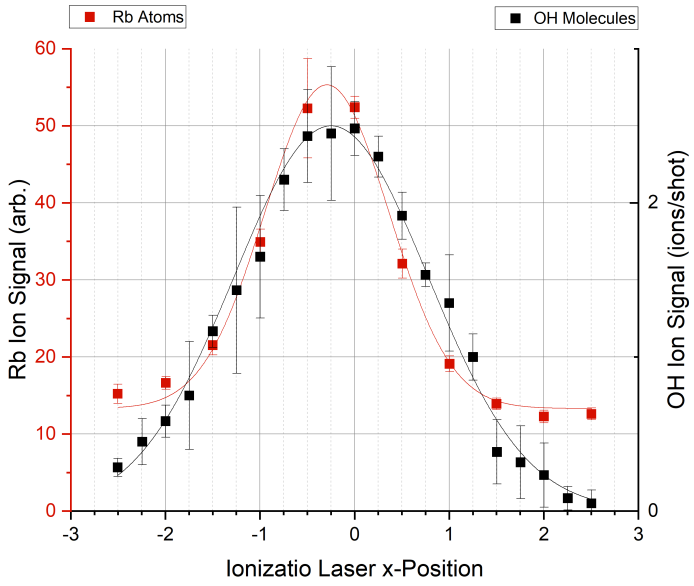

Figure 7.12: Overlap between Rb atoms and OH molecules along the x-axis. A Gaussian fit to the OH molecules is used to determine the correct alignment of the ionization laser along the x-axis.

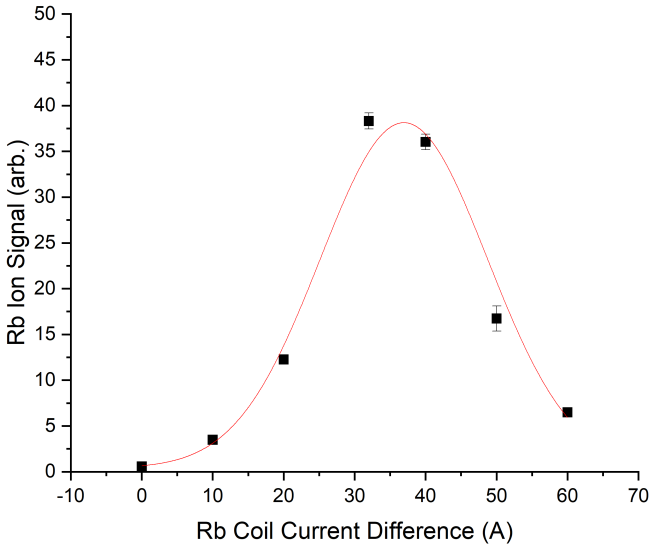

Figure 7.13: Alignment of the Rb atoms along the x-axis. With the ionization laser kept at the center of the electrostatic trap, the Rb atoms are displaced along the x-axis by changing the difference between the trapping coil currents.

to enhance the sensitivity. The signal is shown in Figure 7.14 This signal still has a FWHM on the order of mm, but a Gaussian fit gives us the center with an error of 10s of um.

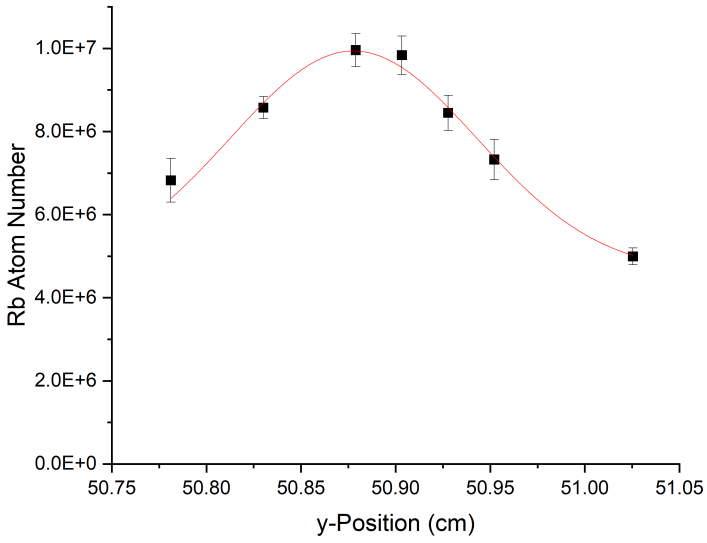

Figure 7.14: Alignment of the Rb atoms along the y-axis. The Rb atoms are brought to the electrostatic trap and the trapping fields are turned on. After 8s the electrostatic trap is turned off and the Rb atoms are transported back to the glass cell where the survival number is determined by absorption imaging.

Chapter 8

Conclusion

8.1 Summary

In this thesis, we have demonstrated a measurement of collisions between cold OH molecules and ultracold Rb atoms in a co-trapped environment. Rb atoms are trapped in a quadrapole magnetic field at a temperature of $T \sim 500\mu K$. The atoms are transported through the vacuum chamber to overlap with an electrostatic quadrapole trap that is used to trap OH molecules. The OH molecules are slowed using a Stark Decelerator and trapped in the electric quadrapole trap with a temperature of $\sim 50mK$. Collisions are inferred from changes in the distribution of the OH molecules in the presence of Rb atoms. Initial estimates of the cross sections from this data can place the inelastic cross section on the order of $O(10^{-13})cm^2$. This is in good agreement with the full theoretical calculations by Lara et al. and the Langevin model. [141] This supports the idea that the internal state of the OH molecule is "scrambled" anytime the molecule is near an Rb atom. Preliminary measurements show no change in the OH energy distribution over a 1 second interaction time, indicating the elastic cross section is much lower than the inelastic. In order to more precisely extract values for the cross sections from our measurements, the experimental data needs to be compared to simulated data. This process is described in the Future Work section below.

A new 1+1' REMPI scheme was developed for detecting decelerated and trapped OH molecule. The advantages of this REMPI detection were discussed, which give it a much higher signal-to-noise ratio than the typical LIF detection. This high signal-to-noise ratio allows the ionization

laser to be focused to a much smaller detection volume, which gives the ability to measure the density distribution of OH molecules in the trap by scanning the ionization laser across the cloud. The usefulness of measuring the density distribution of the OH molecules was demonstrated by measuring the temperature of the trapped OH, as well as examining the dynamics of trapping.

The 1+1' REMPI scheme requires light at 118nm, which is in the vacuum ultraviolet region of the electromagnetic spectrum. We described the theory and experimental implementation of producing 118nm light by frequency tripling 355nm light in a phasematched mixture of Xe and Ar. The power of 118nm light that can be produced was shown to be limited by pressure broadened absorption of 118nm light by Xe.

8.2 Future work

In order to extract the elastic and inelastic cross sections from the experimental data, we need to simulate all of the complex dynamics of the molecules, atoms, and collisions that are occurring simultaneously. This can be achieved using trajectory simulations that propagate the atoms and molecules on the trapping potentials and incorporate conditions that change the populations due to collisions. This will be done in a multi-stage process that uses a purely atomic simulation to generate an analytical model of the Rb density that can be used to generate a probabilistic model of atom-molecule collisions based solely on the molecular motion. The atomic simulation is separated from the molecular simulation for a few reasons. First, the number of Rb atoms present in the co-trap outnumbers the number of molecules by four orders of magnitude. The number of simulated OH particles would be severely limited by the memory and speed requirements of simulating a proportional number of Rb atoms. Second, particle collision models are inherently slow due to the need to search for pairs of particles that are close enough to trigger a collision event. This is further compounded by the need to include Rb-Rb collisions that are important to the dynamics of the trapped Rb atoms. Third, the velocity of the Rb atoms contributes negligibly to the probability or energy of collision. Finally, the effect of OH-Rb collisions on the Rb distribution are negligible due to the significantly larger number of Rb atoms present. An average atom-molecule collision rate

for the OH molecules of 1Hz would mean an average atom-molecule collision rate of 10^{-4} Hz for the Rb atoms. Therefore, the Rb trajectories can be simulated independent of the OH molecules, and the Rb density can be treated as a mean field that the OH propagates through.

The Rb trap simulations will be modeled by generating an initial distribution of particles expected from the purely magnetic trap, then propagating those particles along potentials based on the Stark and Zeeman shifts in the co-trap. The potentials are calculated from electric and magnetic fields generated by COMSOL, a commercially available finite element modeling software. The initial distribution is generated from random initial velocities and positions weighted by a Boltzmann distribution. The distribution of the Rb as a function of time is given by

$$n(x,y,z,t) = \frac{N_{Rb}(t)}{(2\pi)^{3/2}\sigma_x(t)\sigma_y(t)\sigma_z(t)} \exp\left\{-\frac{1}{2}\left(\frac{x^2}{\sigma_x^2(t)} + \frac{y^2}{\sigma_y^2(t)} + \frac{z^2}{\sigma_z^2(t)}\right)\right\} \tag{8.1}$$

where N_{Rb} is the total number of Rb atoms, and $\sigma_x(t)$, $\sigma_y(t)$, and $\sigma_z(t)$ are the Gaussian widths of the cloud in the x, y, and z directions. The number is determined from absorption imaging of the cloud after transporting back to the MOT cell. The number is fit to a double exponential decay with the form

$$N_{Rb}(t) = (N_0 - N_1)e^{-t\frac{\tau_1+\tau_2}{\tau_1\tau_2}} + N_1 e^{-t/\tau_2} \tag{8.2}$$

The widths can be modeled to evolve in time as a double exponential with the form

$$\sigma_i(t) = \lambda_1 e^{-t/\beta_1} + \lambda_2 e^{-t/\beta_2} + \lambda_0 \tag{8.3}$$

The width can be measured in the x dimension by scanning the ionization laser across the cloud using the picomotor. However, the other dimensions cannot be measured easily in our experiment. The measurements in the x dimension are used to fit the simulations, which give the fit parameters in other two dimensions. Once these fit parameters are generated, the density of Rb can be calculated at any position and time in the trap.

The collisions simulations will propagate OH trajectories along the trapping potentials. The initial phase space distribution of OH molecules comes from Monte Carlo simulation of molecules propagating through the decelerator and trap. As the particles are propagated in the trap, the

instantaneous molecular velocity and Rb density are determined for each particle during each time step. The probability of either type of collision collision happening during a given time step is

$$P_i = \Gamma_i \cdot \delta t = \rho_{Rb} v_{OH} \sigma_i \delta t \tag{8.4}$$

$$P_e = \Gamma_e \cdot \delta t = \rho_{Rb} v_{OH} \sigma_e \delta t \tag{8.5}$$

The time step needs to be chosen such that the probabilities are much less than 1. For each molecule, a random number is generated between 0 and 1 for each time step. If the number is less than P_i, an inelastic collision event has occurred and the molecule is removed from the simulation. If the number is between P_i and $P_i + P_e$, an elastic collision event has occurred, and the kinetic energy of the molecule is reduced according to Equation 7.17 with a random recoil angle. If the number is greater than $P_i + P_e$, no collision has occurred and the molecule is unchanged.

To extract the cross sections from the experimental measurements, the simulation will be repeated with many different pairs of values for σ_i and σ_e. Each simulation produces a simulated decay curve which can be compared to the experimental decay curve to determine a quality of fit via a reduced-chi-squared fit. From the landscape of fitness values, the likely range of cross sections can be determined within a confidence interval.

Bibliography

[1] Eric R. Hudson, H. J. Lewandowski, Brian C. Sawyer, and Jun Ye. Cold molecule spectroscopy for constraining the evolution of the fine structure constant. Phys. Rev. Lett., 96:143004, Apr 2006.

[2] Jonathan J Hudson, Dhiren M Kara, IJ Smallman, Ben E Sauer, Michael R Tarbutt, and Ed A Hinds. Improved measurement of the shape of the electron. Nature, 473(7348):493–496, 2011.

[3] Vitaly Andreev and NR Hutzler. Improved limit on the electric dipole moment of the electron. Nature, 562(7727):355–360, 2018.

[4] William B. Cairncross, Daniel N. Gresh, Matt Grau, Kevin C. Cossel, Tanya S. Roussy, Yiqi Ni, Yan Zhou, Jun Ye, and Eric A. Cornell. Precision measurement of the electron's electric dipole moment using trapped molecular ions. Phys. Rev. Lett., 119:153001, Oct 2017.

[5] R. Mitra, V. S. Prasannaa, R. F. Garcia Ruiz, T. K. Sato, M. Abe, Y. Sakemi, B. P. Das, and B. K. Sahoo. Towards *cp*-violation studies on superheavy molecules: Theoretical and experimental perspectives. Phys. Rev. A, 104:062801, Dec 2021.

[6] John L Bohn, Ana Maria Rey, and Jun Ye. Cold molecules: Progress in quantum engineering of chemistry and quantum matter. Science, 357(6355):1002–1010, 2017.

[7] Jutta Toscano, HJ Lewandowski, and Brianna R Heazlewood. Cold and controlled chemical reaction dynamics. Physical Chemistry Chemical Physics, 22(17):9180–9194, 2020.

[8] Valentine Wakelam, J-C Loison, E Herbst, B Pavone, A Bergeat, K Béroff, M Chabot, A Faure, Daniele Galli, Wolf D Geppert, et al. The 2014 kida network for interstellar chemistry. The Astrophysical Journal Supplement Series, 217(2):20, 2015.

[9] Joseph M. Beames, Fang Liu, Lu Lu, and Marsha I. Lester. Uv spectroscopic characterization of an alkyl substituted criegee intermediate ch3choo. J. Chem. Phys., 138(24):244307, 2013.

[10] Nathanael M. Kidwell, Hongwei Li, Xiaohong Wang, Joel M. Bowman, and Marsha I. Lester. Unimolecular dissociation dynamics of vibrationally activated ch3choo criegee intermediates to oh radical products. Nat. Chem., 8:509–514, 2015.

[11] Daniel Stone, Lisa K. Whalley, and Dwayne E. Heard. Tropospheric oh and ho2 radicals: field measurements and model comparisons. Chem. Soc. Rev., 41:6348–6404, 2012.

[12] Gregory P Smith, Jorge Luque, Chung Park, Jay B Jeffries, and David R Crosley. Low pressure flame determinations of rate constants for oh(a) and ch(a) chemiluminescence. Combust. Flame, 131(1–2):59 – 69, 2002.

[13] Namrata Vora, Jia Eng Siow, and Normand M Laurendeau. Chemical scavenging activity of gaseous suppressants by using laser-induced fluorescence measurements of hydroxyl. Combust. Flame, 126(1–2):1393 – 1401, 2001.

[14] J. Guibert, M. Elitzur, and Nguyen-Q-Rieu. Oh excitation in interstellar clouds. Astron. Astrophys., 66(3):395–405, 1978.

[15] F. Yusef-Zadeh, M. Wardle, and D. A. Roberts. Thermal oh (1667/1665 mhz) absorption and nonthermal oh (1720 mhz) emission toward the w28 supernova remnant. Astrophys. J., 583(1):267, 2003.

[16] Alon B Henson, Sasha Gersten, Yuval Shagam, Julia Narevicius, and Edvardas Narevicius. Observation of resonances in penning ionization reactions at sub-kelvin temperatures in merged beams. Science, 338(6104):234–238, 2012.

[17] Sjoerd N Vogels, Jolijn Onvlee, Simon Chefdeville, Ad van der Avoird, Gerrit C Groenenboom, and Sebastiaan YT van de Meerakker. Imaging resonances in low-energy no-he inelastic collisions. Science, 350(6262):787–790, 2015.

[18] Simon Chefdeville, Yulia Kalugina, Sebastiaan YT van de Meerakker, Christian Naulin, François Lique, and Michel Costes. Observation of partial wave resonances in low-energy o2–h2 inelastic collisions. Science, 341(6150):1094–1096, 2013.

[19] Ayelet Klein, Yuval Shagam, Wojciech Skomorowski, Piotr S Żuchowski, Mariusz Pawlak, Liesbeth Janssen, Nimrod Moiseyev, Sebastiaan YT van de Meerakker, Ad van der Avoird, Christiane P Koch, et al. Directly probing anisotropy in atom–molecule collisions through quantum scattering resonances. Nature Physics, 13(1):35–38, 2017.

[20] Junwen Zou, Sean D. S. Gordon, and Andreas Osterwalder. Sub-kelvin stereodynamics of the $\mathrm{Ne}(^3P_2) + \mathrm{n}_2$ reaction. Phys. Rev. Lett., 123:133401, Sep 2019.

[21] Aernout P. P. van der Poel, Peter C. Zieger, Sebastiaan Y. T. van de Meerakker, Jérôme Loreau, Ad van der Avoird, and Hendrick L. Bethlem. Cold collisions in a molecular synchrotron. Phys. Rev. Lett., 120:033402, Jan 2018.

[22] Ludwig Scharfenberg, Sebastiaan YT van de Meerakker, and Gerard Meijer. Crossed beam scattering experiments with optimized energy resolution. Physical Chemistry Chemical Physics, 13(18):8448–8456, 2011.

[23] Nitzan Akerman, Michael Karpov, Yair Segev, Natan Bibelnik, Julia Narevicius, and Edvardas Narevicius. Trapping of molecular oxygen together with lithium atoms. Phys. Rev. Lett., 119:073204, Aug 2017.

[24] Matthew T. Hummon, Timur V. Tscherbul, Jacek Kłos, Hsin-I Lu, Edem Tsikata, Wesley C. Campbell, Alexander Dalgarno, and John M. Doyle. Cold **N**+NH collisions in a magnetic trap. Phys. Rev. Lett., 106:053201, Feb 2011.

[25] L. P. Parazzoli, N. J. Fitch, P. S. Żuchowski, J. M. Hutson, and H. J. Lewandowski. Large effects of electric fields on atom-molecule collisions at millikelvin temperatures. Phys. Rev. Lett., 106:193201, 2011.

[26] N. J. Fitch, L. P. Parazzoli, and H. J. Lewandowski. Collisions between ultracold atoms and cold molecules in a dual electrostatic-magnetic trap. Phys. Rev. A, 101:032703, Mar 2020.

[27] S Jurgilas, A Chakraborty, CJH Rich, L Caldwell, HJ Williams, NJ Fitch, BE Sauer, Matthew D Frye, Jeremy M Hutson, and MR Tarbutt. Collisions between ultracold molecules and atoms in a magnetic trap. Physical Review Letters, 126(15):153401, 2021.

[28] Valentina Zhelyazkova, Anne Cournol, Thomas E Wall, Aki Matsushima, Jonathan J Hudson, EA Hinds, MR Tarbutt, and BE Sauer. Laser cooling and slowing of caf molecules. Physical Review A, 89(5):053416, 2014.

[29] Alejandra L Collopy, Shiqian Ding, Yewei Wu, Ian A Finneran, Loïc Anderegg, Benjamin L Augenbraun, John M Doyle, and Jun Ye. 3d magneto-optical trap of yttrium monoxide. Physical review letters, 121(21):213201, 2018.

[30] JF Barry, DJ McCarron, EB Norrgard, MH Steinecker, and D DeMille. Magneto-optical trapping of a diatomic molecule. Nature, 512(7514):286–289, 2014.

[31] DJ Larson, James C Bergquist, John J Bollinger, Wayne M Itano, and David J Wineland. Sympathetic cooling of trapped ions: A laser-cooled two-species nonneutral ion plasma. Physical review letters, 57(1):70, 1986.

[32] M. Mudrich, S. Kraft, K. Singer, R. Grimm, A. Mosk, and M. Weidemüller. Sympathetic cooling with two atomic species in an optical trap. Phys. Rev. Lett., 88:253001, Jun 2002.

[33] Eric R Hudson. Sympathetic cooling of molecular ions with ultracold atoms. EPJ Techniques and Instrumentation, 3:1–21, 2016.

[34] K.-K. Ni, S. Ospelkaus, M. H. G. de Miranda, A. Pe'er, B. Neyenhuis, J. J. Zirbel, S. Kotochigova, P. S. Julienne, D. S. Jin, and J. Ye. A high phase-space-density gas of polar molecules. Science, 322(5899):231–235, 2008.

[35] Thorsten Köhler, Krzysztof Góral, and Paul S. Julienne. Production of cold molecules via magnetically tunable feshbach resonances. Rev. Mod. Phys., 78:1311–1361, Dec 2006.

[36] Tetsu Takekoshi, Markus Debatin, Raffael Rameshan, Francesca Ferlaino, Rudolf Grimm, Hanns-Christoph Nägerl, C Ruth Le Sueur, Jeremy M Hutson, Paul S Julienne, Svetlana Kotochigova, et al. Towards the production of ultracold ground-state rbcs molecules: Feshbach resonances, weakly bound states, and the coupled-channel model. Physical Review A, 85(3):032506, 2012.

[37] Johann G Danzl, Manfred J Mark, Elmar Haller, Mattias Gustavsson, Russell Hart, Jesus Aldegunde, Jeremy M Hutson, and Hanns-Christoph Nägerl. An ultracold high-density sample of rovibronic ground-state molecules in an optical lattice. Nature Physics, 6(4):265–270, 2010.

[38] Mingyang Guo, Bing Zhu, Bo Lu, Xin Ye, Fudong Wang, Romain Vexiau, Nadia Bouloufa-Maafa, Goulven Quéméner, Olivier Dulieu, and Dajun Wang. Creation of an ultracold gas of ground-state dipolar na 23 rb 87 molecules. Physical review letters, 116(20):205303, 2016.

[39] Jee Woo Park, Sebastian A Will, and Martin W Zwierlein. Ultracold dipolar gas of fermionic na 23 k 40 molecules in their absolute ground state. Physical review letters, 114(20):205302, 2015.

[40] MHG De Miranda, A Chotia, Brian Neyenhuis, D Wang, G Quéméner, Silke Ospelkaus, JL Bohn, Jun Ye, and DS Jin. Controlling the quantum stereodynamics of ultracold bimolecular reactions. Nature Physics, 7(6):502–507, 2011.

[41] Luigi De Marco, Giacomo Valtolina, Kyle Matsuda, William G Tobias, Jacob P Covey, and Jun Ye. A degenerate fermi gas of polar molecules. Science, 363(6429):853–856, 2019.

[42] Giacomo Valtolina, Kyle Matsuda, William G Tobias, Jun-Ru Li, Luigi De Marco, and Jun Ye. Dipolar evaporation of reactive molecules to below the fermi temperature. Nature, 588(7837):239–243, 2020.

[43] Jun-Ru Li, William G Tobias, Kyle Matsuda, Calder Miller, Giacomo Valtolina, Luigi De Marco, Reuben RW Wang, Lucas Lassablière, Goulven Quéméner, John L Bohn, et al. Tuning of dipolar interactions and evaporative cooling in a three-dimensional molecular quantum gas. Nature Physics, 17(10):1144–1148, 2021.

[44] A.J.C. Varandas and A.I. Voronin. Calculation of the asymptotic interaction and modelling of the potential energy curves of oh and oh+. Chemical Physics, 194(1):91–100, 1995.

[45] Gerhard Herzberg. The spectra and structures of simple free radicals: an introduction to molecular spectroscopy. Courier Corporation, 1988.

[46] John M. Brown and Alan Carrington. Rotational Spectroscopy of Diatomic Molecules. Cambridge Molecular Science. Cambridge University Press, 2003.

[47] Brian Sawyer. Cold polar molecules for novel collision experiments at low energies. PhD thesis, University of Colorado, 2010.

[48] Giacinto Scoles, D.R Miller, W. Gentry, H Pauly, Davide Bassi, U.Hefter, K. Bergman, Mario Zen, J. Reuss, C.J.N. Meijdenberg, D. Abuerbach, M. Kappes, Samuel Leutwyler, Ugo Valbusa, U. Buck, Y.T. Lee, Paul Dagdigian, Steven Stolte, R. Düren, and Salvatore Iannotta. Atomic and Molecular Beam Methods: Vol. 1. 01 1998.

[49] Travis Briles. Production, Deceleration, and Detection of OH Radicals. PhD thesis, University of Colorado, 2015.

[50] D Proch and T Trickl. A high-intensity multi-purpose piezoelectric pulsed molecular beam source. Review of Scientific Instruments, 60(4):713–716, 1989.

[51] Sebastiaan YT van de Meerakker, Nicolas Vanhaecke, Hendrick L Bethlem, and Gerard Meijer. Transverse stability in a stark decelerator. Physical Review A, 73(2):023401, 2006.

[52] Eric R Hudson, JR Bochinski, HJ Lewandowski, Brian C Sawyer, and Jun Ye. Efficient stark deceleration of cold polar molecules. The European Physical Journal D-Atomic, Molecular, Optical and Plasma Physics, 31(2):351–358, 2004.

[53] Dongdong Zhang, Gerard Meijer, and Nicolas Vanhaecke. Advanced switching schemes in a stark decelerator. Physical Review A, 93(2):023408, 2016.

[54] LP Parazzoli, N Fitch, DS Lobser, and HJ Lewandowski. High-energy-resolution molecular beams for cold collision studies. New Journal of Physics, 11(5):055031, 2009.

[55] Ludwig Scharfenberg, Henrik Haak, Gerard Meijer, and Sebastiaan YT van de Meerakker. Operation of a stark decelerator with optimum acceptance. Physical Review A, 79(2):023410, 2009.

[56] Andreas Osterwalder, Samuel A Meek, Georg Hammer, Henrik Haak, and Gerard Meijer. Deceleration of neutral molecules in macroscopic traveling traps. Physical Review A, 81(5):051401, 2010.

[57] Yomay Shyur, Jason A Bossert, and HJ Lewandowski. Pulsed operation of a ring stark decelerator. Journal of Physics B: Atomic, Molecular and Optical Physics, 51(16):165101, 2018.

[58] Dave Reens. University of Colorado-Boulder, 2019.

[59] Amy M. Green, Fang Liu, and Marsha I. Lester. Uv + v uv double-resonance studies of autoionizing rydberg states of the hydroxyl radical. J. Chem. Phys., 144(18), 2016.

[60] John M. Gray, Jason A. Bossert, Yomay Shyur, and H. J. Lewandowski. Measurements of trap dynamics of cold oh molecules using resonance-enhanced multiphoton ionization. Phys. Rev. A, 96:023416, Aug 2017.

[61] N. Fitch, L. Parazzoli, and Heather Lewandowski. Collisions between ultracold atoms and cold molecules in a dual electrostatic-magnetic trap. Physical Review A, 101:032703, 2020-03 2020.

[62] John M Gray, Jason Bossert, Yomay Shyur, Ben Saarel, Travis C Briles, and HJ Lewandowski. Characterization of a vacuum ultraviolet light source at 118 nm. The Journal of Chemical Physics, 154(2):024201, 2021.

[63] James AR Samson. Techniques of vacuum ultraviolet spectroscopy. John Wiley and Sons, 1967.

[64] James A Samson, David L Ederer, Thomas Lucatorto, and Marc De Graef. Vacuum ultraviolet spectroscopy I, volume 1. Academic press, 1998.

[65] James A Samson, David L Ederer, Thomas Lucatorto, and Marc De Graef. Vacuum ultraviolet spectroscopy II, volume 2. Academic press, 1998.

[66] Cheuk-Yiu Ng. Vacuum ultraviolet spectroscopy and chemistry by photoionization and photoelectron methods. Annual review of physical chemistry, 53(1):101–140, 2002.

[67] Daniel R Albert and H Floyd Davis. Studies of bimolecular reaction dynamics using pulsed high-intensity vacuum-ultraviolet lasers for photoionization detection. Physical Chemistry Chemical Physics, 15(35):14566–14580, 2013.

[68] Arman Cingöz, Dylan C Yost, Thomas K Allison, Axel Ruehl, Martin E Fermann, Ingmar Hartl, and Jun Ye. Direct frequency comb spectroscopy in the extreme ultraviolet. Nature, 482(7383):68–71, 2012.

[69] Nelson De Oliveira, Mourad Roudjane, Denis Joyeux, Daniel Phalippou, Jean-Claude Rodier, and Laurent Nahon. High-resolution broad-bandwidth fourier-transform absorption spectroscopy in the vuv range down to 40 nm. Nature Photonics, 5(3):149–153, 2011.

[70] S Hannemann, EJ Salumbides, S Witte, R Th Zinkstok, E-J Van Duijn, KSE Eikema, and W Ubachs. Frequency metrology on the E F Σ g+ 1? X Σ g+ 1 (0, 0) transition in H_2, HD, and D_2. Physical Review A, 74(6):062514, 2006.

[71] Wade G Rellergert, D DeMille, RR Greco, MP Hehlen, JR Torgerson, and Eric R Hudson. Constraining the Evolution of the Fundamental Constants with a Solid-State Optical Frequency Reference Based on the Th 229 Nucleus. Physical review letters, 104(20):200802, 2010.

[72] EE Eyler, DE Chieda, Matthew C Stowe, Michael J Thorpe, TR Schibli, and Jun Ye. Prospects for precision measurements of atomic helium using direct frequency comb spectroscopy. The European Physical Journal D-Atomic, Molecular, Optical and Plasma Physics, 48(1):43–55, 2008.

[73] Joan B Pallix, Udo Schuhle, Christopher H Becker, and David L Huestis. Advantages of single-photon ionization over multiphoton ionization for mass-spectrometric surface analysis of bulk organic polymers. Analytical Chemistry, 61(8):805–811, 1989.

[74] RJJM Steenvoorden, PG Kistemaker, AE De Vries, L Michalak, and NMM Nibbering. Laser single photon ionization mass spectrometry of linear, branched and cyclic hexanes. International journal of mass spectrometry and ion processes, 107(3):475–489, 1991.

[75] Dirk Basting and Gerd Marowsky. Excimer laser technology. Springer Science & Business Media, 2005.

[76] Robert W Boyd. Nonlinear optics. Academic press, 2003.

[77] Yuen-Ron Shen. Principles of nonlinear optics. Wiley-Interscience, New York, NY, USA, 1984.

[78] Geoffrey New. Introduction to Nonlinear Optics. Cambridge University Press, 2011.

[79] David E. Couch, Daniel D. Hickstein, David G. Winters, Sterling J. Backus, Matthew S. Kirchner, Scott R. Domingue, Jessica J. Ramirez, Charles G. Durfee, Margaret M. Murnane, and Henry C. Kapteyn. Ultrafast 1mhz vacuum-ultraviolet source via highly cascaded harmonic generation in negative-curvature hollow-core fibers. Optica, 7(7):832–837, Jul 2020.

[80] Kunihiro Suto, Yoshihiro Sato, Claire L. Reed, Vladimir Skorokhodov, Yutaka Matsumi, and Masahiro Kawasaki. Ion fragment imaging of the ion-pair photodissociation of ch3cl, ch3br, c2h5cl, and c2h5br at 118 nm. The Journal of Physical Chemistry A, 101(7):1222–1226, 1997.

[81] Toshiaki Munakata and Takahiro Kasuya. Ion pair production from ch3cl and ch3br with 118 nm laser light. Chemical Physics Letters, 154(6):604 – 609, 1989.

[82] Jie Yang, Xue-Bin Wang, Xiao-Peng Xing, and Lai-Sheng Wang. Photoelectron spectroscopy of anions at 118.2nm: Observation of high electron binding energies in superhalogens mcl4 (m=sc, y, la). The Journal of Chemical Physics, 128(20):201102, 2008.

[83] Jian Li, Veronica M Bierbaum, and Stephen R Leone. Laser ionization time-of-flight mass spectrometer detection of methyl radical produced by ion–molecule reactions in a flowing-afterglow apparatus. Chemical Physics Letters, 313(1):76 – 84, 1999.

[84] William M. Jackson and Dadong Xu. Photodissociation of the acetone cation at 355 nm using the velocity imaging technique. The Journal of Chemical Physics, 113(9):3651–3657, 2000.

[85] Y. J. Shi, S. Consta, A. K. Das, B. Mallik, D. Lacey, and R. H. Lipson. A 118 nm vacuum ultraviolet laser/time-of-flight mass spectroscopic study of methanol and ethanol clusters in the vapor phase. The Journal of Chemical Physics, 116(16):6990–6999, 2002.

[86] D. N. Shin, Y. Matsuda, and E. R. Bernstein. On the iron oxide neutral cluster distribution in the gas phase. ii. detection through 118 nm single photon ionization. The Journal of Chemical Physics, 120(9):4157–4164, 2004.

[87] Joseph M. Beames, Fang Liu, Marsha I. Lester, and Craig Murray. Communication: A new spectroscopic window on hydroxyl radicals using uv + vuv resonant ionization. The Journal of Chemical Physics, 134(24):241102, 2011.

[88] Joseph M. Beames, Fang Liu, and Marsha I. Lester. 1+1 resonant multiphoton ionisation of oh radicals via the a2+ state: insights from direct comparison with a-x laser-induced fluorescence detection. Molecular Physics, 112(7):897–903, 2014.

[89] M. P. McCann, C. H. Chen, and M. G. Payne. Two-photon (vacuum ultraviolet + visible) spectroscopy of argon, krypton, xenon, and molecular hydrogen. The Journal of Chemical Physics, 89(9):5429–5441, 1988.

[90] JF Ward and GHC New. Optical third harmonic generation in gases by a focused laser beam. Physical Review, 185(1):57, 1969.

[91] R Miles and S Harris. Optical third-harmonic generation in alkali metal vapors. Quantum Electronics, IEEE Journal of, 9(4):470–484, 1973.

[92] Gary C Bjorklund. Effects of focusing on third-order nonlinear processes in isotropic media. Quantum Electronics, IEEE Journal of, 11(6):287–296, 1975.

[93] Nicholas P. Lockyer and John C. Vickerman. Single photon ionisation mass spectrometry using laser-generated vacuum ultraviolet photons. Laser Chem, 17:139–159, 1997.

[94] DA Kleinman. Nonlinear dielectric polarization in optical media. Physical Review, 126(6):1977, 1962.

[95] Rita Mahon, T McIlrath, V Myerscough, and David W Koopman. Third-harmonic generation in argon, krypton, and xenon: bandwidth limitations in the vicinity of Lyman-α. Quantum Electronics, IEEE Journal of, 15(6):444–451, 1979.

[96] A. Kramida, Yu. Ralchenko, J. Reader, and and NIST ASD Team. NIST Atomic Spectra Database (ver. 5.3), [Online]. Available: `http://physics.nist.gov/asd` [2016, January 29]. National Institute of Standards and Technology, Gaithersburg, MD., 2015.

[97] G. A. Hebner and G. N. Hays. Measured pressure broadening and shift rates of the 1.73 m (5d[3/2]1–6p[5/2]2) transition of xenon. Applied Physics Letters, 59(5):537–539, 1991.

[98] Greg A. Pitz, Douglas E. Wertepny, and Glen P. Perram. Pressure broadening and shift of the cesium D_1 transition by the noble gases and n_2, h_2, hd, d_2, ch_4, c_2h_6, cf_4, and ^{3}He. Phys. Rev. A, 80:062718, Dec 2009.

[99] Wanda R. Ferrell, M. G. Payne, and W. R. Garrett. Resonance broadening and shifting of spectral lines in xenon and krypton. Phys. Rev. A, 36:81–89, Jul 1987.

[100] W. F. Chan, G. Cooper, X. Guo, G. R. Burton, and C. E. Brion. Absolute optical oscillator strengths for the electronic excitation of atoms at high resolution. iii. the photoabsorption of argon, krypton, and xenon. Phys. Rev. A, 46:149–171, Jul 1992.

[101] AH Kung. Third-harmonic generation in a pulsed supersonic jet of xenon. Optics letters, 8(1):24–26, 1983.

[102] A L'huillier, LA Lompre, M Ferray, XF Li, G Mainfray, and C Manus. Third-harmonic generation in xenon in a pulsed jet and a gas cell. EPL (Europhysics Letters), 5(7):601, 1988.

[103] B. G. U. Englert, M. Mielenz, C. Sommer, J. Bayerl, M. Motsch, P. W. H. Pinkse, G. Rempe, and M. Zeppenfeld. Storage and adiabatic cooling of polar molecules in a microstructured trap. Phys. Rev. Lett., 107:263003, 2011.

[104] Sebastiaan Y. T. van de Meerakker, Paul H. M. Smeets, Nicolas Vanhaecke, Rienk T. Jongma, and Gerard Meijer. Deceleration and electrostatic trapping of oh radicals. Phys. Rev. Lett., 94:023004, 2005.

[105] E Tsikata, W C Campbell, M T Hummon, H-I Lu, and J M Doyle. Magnetic trapping of nh molecules with 20s lifetimes. New J. Phys., 12(6):065028, 2010.

[106] Steven Hoekstra, Joop J. Gilijamse, Boris Sartakov, Nicolas Vanhaecke, Ludwig Scharfenberg, Sebastiaan Y. T. van de Meerakker, and Gerard Meijer. Optical pumping of trapped neutral molecules by blackbody radiation. Phys. Rev. Lett., 98:133001, 2007.

[107] Hendrick. L. Bethlem, Giel Berden, Floris M H Crompvoets, Rienk T. Jongma, André J a van Roij, and Gerard Meijer. Electrostatic trapping of ammonia molecules. Nature, 406(August):491–4, 2000.

[108] Hendrick L. Bethlem, Floris M. H. Crompvoets, Rienk T. Jongma, Sebastiaan Y. T. van de Meerakker, and Gerard Meijer. Deceleration and trapping of ammonia using time-varying electric fields. Phys. Rev. A, 65:053416, 2002.

[109] Jacqueline van Veldhoven, Hendrick L. Bethlem, Melanie Schnell, and Gerard Meijer. Versatile electrostatic trap. Phys. Rev. A, 73:063408, 2006.

[110] J. J. Gilijamse, S. Hoekstra, N. Vanhaecke, S.Y.T. van de Meerakker, and G. Meijer. Loading stark-decelerated molecules into electrostatic quadrupole traps. Eur. Phys. J. D, 57(1):33–41, 2010.

[111] Congsen Meng, Aernout P. P. van der Poel, Cunfeng Cheng, and Hendrick L. Bethlem. Femtosecond laser detection of stark-decelerated and trapped methylfluoride molecules. Phys. Rev. A, 92:023404, 2015.

[112] T. Rieger, T. Junglen, S. A. Rangwala, P. W. H. Pinkse, and G. Rempe. Continuous loading of an electrostatic trap for polar molecules. Phys. Rev. Lett., 95:173002, Oct 2005.

[113] Hsin-I Lu, Ivan Kozyryev, Boerge Hemmerling, Julia Piskorski, and John M. Doyle. Magnetic trapping of molecules via optical loading and magnetic slowing. Phys. Rev. Lett., 112:113006, 2014.

[114] Yang Liu, Manish Vashishta, Pavle Djuricanin, Sida Zhou, Wei Zhong, Tony Mittertreiner, David Carty, and Takamasa Momose. Magnetic trapping of cold methyl radicals. Phys. Rev. Lett., 118:093201, 2017.

[115] J. S. Eardley, N. Warner, L. Z. Deng, D. Carty, and E. Wrede. Magnetic trapping of sh radicals. Phys. Chem. Chem. Phys., 19:8423–8427, 2017.

[116] Marina Quintero-Pérez, Paul Jansen, Thomas E. Wall, Joost E. van den Berg, Steven Hoekstra, and Hendrick L. Bethlem. Static trapping of polar molecules in a traveling wave decelerator. Phys. Rev. Lett., 110:133003, Mar 2013.

[117] Paul Jansen, Marina Quintero-Pérez, Thomas E. Wall, Joost E. van den Berg, Steven Hoekstra, and Hendrick L. Bethlem. Deceleration and trapping of ammonia molecules in a traveling-wave decelerator. Phys. Rev. A, 88:043424, Oct 2013.

[118] Marina Quintero-Pérez, Thomas E. Wall, Steven Hoekstra, and Hendrick L. Bethlem. Preparation of an ultra-cold sample of ammonia molecules for precision measurements. J. Mol. Spectrosc., 300:112 – 115, 2014.

[119] Martin Zeppenfeld, Barbara G. U. Englert, Rosa Glockner, Alexander Prehn, Manuel Mielenz, Christian Sommer, Laurens D. van Buuren, Michael Motsch, and Gerhard Rempe. Sisyphus cooling of electrically trapped polyatomic molecules. Nature, 491:570–573, Nov 2012.

[120] Rosa Glöckner, Alexander Prehn, Gerhard Rempe, and Martin Zeppenfeld. Rotational state detection of electrically trapped polyatomic molecules. New J. Phys., 17(5):055022, 2015.

[121] Alexander Prehn, Martin Ibrügger, Rosa Glöckner, Gerhard Rempe, and Martin Zeppenfeld. Optoelectrical cooling of polar molecules to submillikelvin temperatures. Phys. Rev. Lett., 116:063005, Feb 2016.

[122] Sebastiaan Y. T. van de Meerakker, Nicolas Vanhaecke, Mark P. J. van der Loo, Gerrit C. Groenenboom, and Gerard Meijer. Direct measurement of the radiative lifetime of vibrationally excited oh radicals. Phys. Rev. Lett., 95:013003, 2005.

[123] Wesley C. Campbell, Gerrit C. Groenenboom, Hsin-I Lu, Edem Tsikata, and John M. Doyle. Time-domain measurement of spontaneous vibrational decay of magnetically trapped nh. Phys. Rev. Lett., 100:083003, 2008.

[124] Matthew T. Hummon, Timur V. Tscherbul, Jacek Kłos, Hsin-I Lu, Edem Tsikata, Wesley C. Campbell, Alexander Dalgarno, and John M. Doyle. Cold $\mathbf{N}$+NH collisions in a magnetic trap. Phys. Rev. Lett., 106:053201, 2011.

[125] Wesley C. Campbell, Edem Tsikata, Hsin-I Lu, Laurens D. van Buuren, and John M. Doyle. Magnetic trapping and zeeman relaxation of nh ($x\ ^3\Sigma^-$). Phys. Rev. Lett., 98:213001, 2007.

[126] Brian C. Sawyer, Benjamin K. Stuhl, Mark Yeo, Timur V. Tscherbul, Matthew T. Hummon, Yong Xia, Jacek Klos, David Patterson, John M. Doyle, and Jun Ye. Cold heteromolecular dipolar collisions. Phys. Chem. Chem. Phys., 13:19059–19066, 2011.

[127] Benjamin K.Stuhl, Matthew T. Hummon, Mark Yeo, Goulven Quéméner, John L. Bohn, and Jun Ye. Evaporative cooling of the dipolar hydroxyl radical. Nature, 492:396–400, Jul 2012.

[128] Brian C. Sawyer, Benjamin L. Lev, Eric R. Hudson, Benjamin K. Stuhl, Manuel Lara, John L. Bohn, and Jun Ye. Magnetoelectrostatic trapping of ground state oh molecules. Phys. Rev. Lett., 98:253002, 2007.

[129] Brian C. Sawyer, Benjamin K. Stuhl, Dajun Wang, Mark Yeo, and Jun Ye. Molecular beam collisions with a magnetically trapped target. Phys. Rev. Lett., 101:203203, 2008.

[130] Joseph M. Beames, Fang Liu, Marsha I. Lester, and Craig Murray. Communication: A new spectroscopic window on hydroxyl radicals using uv + vuv resonant ionization. J. Chem. Phys., 134(24), 2011.

[131] Joseph M. Beames, Fang Liu, and Marsha I. Lester. 1+1 resonant multiphoton ionisation of oh radicals via the a2+ state: insights from direct comparison with a-x laser-induced fluorescence detection. Mol. Phys., 112(7):897–903, 2014.

[132] Hendrick L. Bethlem, Giel Berden, and Gerard Meijer. Decelerating neutral dipolar molecules. Phys. Rev. Lett., 83:1558–1561, Aug 1999.

[133] Nicholas P. Lockyer and John C. Vickerman. Single Photon Ionisation Mass Spectrometry Using Laser-Generated Vacuum Ultraviolet Photons. Laser Chem., 17:139–159, 1997.

[134] A.H. Kung, J.F. Young, and S.E. Harris. Generation of 1182-Å radiation in phase-matched mixtures of inert gases. Appl. Phys. Lett, 22(6):301–302, 1973.

[135] Travis C. Briles, John M. Gray, Yomay Shyur, and H. J. Lewandowski. Characterization and optimization of a vuv light source at 118nm. In preparation.

[136] See Supplemental Material at [URL will be inserted by publisher] for phase-space movies of both trapping schemes.

[137] Harold Jeffreys. Theory of Probability. Oxford University Press, Oxford, 3 edition, 1998.

[138] P. Allmendinger, J. Deiglmayr, J. A. Agner, H. Schmutz, and F. Merkt. Surface-electrode decelerator and deflector for rydberg atoms and molecules. Phys. Rev. A, 90:043403, Oct 2014.

[139] Ch. Seiler, S. D. Hogan, and F. Merkt. Trapping cold molecular hydrogen. Phys. Chem. Chem. Phys., 13:19000–19012, 2011.

[140] Manuel Lara, John L. Bohn, Daniel Potter, Pavel Soldán, and Jeremy M. Hutson. Ultracold rb-oh collisions and prospects for sympathetic cooling. Phys. Rev. Lett., 97:183201, Nov 2006.

[141] Manuel Lara, John L. Bohn, Daniel E. Potter, Pavel Soldán, and Jeremy M. Hutson. Cold collisions between oh and rb: The field-free case. Phys. Rev. A, 75:012704, Jan 2007.

[142] Kenji Maeda, Michael L Wall, and Lincoln D Carr. Hyperfine structure of the hydroxyl free radical (oh) in electric and magnetic fields. New Journal of Physics, 17(4):045014, 2015.

[143] Raphael D Levine, Richard B Bernstein, and Yuan T Lee. Molecular reaction dynamics and chemical reactivity. Physics Today, 41(10):90, 1988.

[144] Steven Hoekstra, Joop J. Gilijamse, Boris Sartakov, Nicolas Vanhaecke, Ludwig Scharfenberg, Sebastiaan Y. T. van de Meerakker, and Gerard Meijer. Optical pumping of trapped neutral molecules by blackbody radiation. Phys. Rev. Lett., 98:133001, 2007.

[145] Robert deCarvalho, John M Doyle, Bretislav Friedrich, Thierry Guillet, Jinha Kim, David Patterson, and Jonathan D Weinstein. Buffer-gas loaded magnetic traps for atoms and molecules: A primer. The European Physical Journal D-Atomic, Molecular, Optical and Plasma Physics, 7(3):289–309, 1999.

[146] Christian Krenn, Werner Scherf, Oleg Khait, Maurizio Musso, and Laurentius Windholz. Stark effect investigations of resonance lines of neutral potassium, rubidium, europium and gallium. Zeitschrift für Physik D Atoms, Molecules and Clusters, 41(4):229–233, 1997.